June 2021

Investigation on the Structure and Dynamics of Lithium Ion Solvation Shell by Linear and Non-Linear Infrared Spectroscopy

Xiaobing Chen
Louisiana State University and Agricultural and Mechanical College

INVESTIGATION ON THE STRUCTURE AND DYNAMICS OF LITHIUM ION SOLVATION SHELL BY LINEAR AND NON-LINEAR INFRARED SPECTROSCOPY

A Dissertation

Submitted to the Graduate Faculty of the
Louisiana State University and
Agricultural and Mechanical College
in partial fulfillment of the
requirements for the degree of
Doctor of Philosophy

in

The Department of Chemistry

by
Xiaobing Chen
B.E., Qingdao University of Science and Technology, 2016
August 2021

ACKNOWLEGEMENTS

There is an old saying in China that says, “He who teaches me once is my mentor for life”. I would like to express sincere gratitude to my advisor, Prof. Daniel Kuroda, for his mentorship and continuous support during my graduate school. Prof. Kuroda has been playing a vital role in my PhD career, teaching me to become an ethical scientist and conduct good-quality research. My career goals are made possible under his guidance.

I want to thank all my committee members, Prof. Chen, Prof. Maverick, Prof. Charalampopoulos (deceased) and Prof. Griffin for the advice and valuable feedback on my research. I also want to show special appreciation to Prof. Kuroda, Prof. Maverick and Prof. Chen for being the professional references of my job application.

I am grateful for the help and support provided by all the current and former group members in Kuroda group, especially Kristen, Yaowen, Xiaoliu, Susith and Jeramie, who have accompanied me in the office for the longest time.

I want to extend my gratitude to my family for all the encouragement, understanding and love they have shown. Moreover, I appreciate the companionship of my friends (in both China and US) over the years. Life at LSU has been made more colorful and enjoyable because of you all.

I believe diligence and persistence are more important than anything else during my pursuit of a PhD degree. Lastly, I want to share a saying that I like and always try to stick to, which says, “When there’s a will, there’s a way”.

TABLE OF CONTENTS

ABSTRACT

Lithium ion battery (LIB) is a lightweight, rechargeable and powerful battery that is used widely from mobile phones to laptops to electric cars. It has many exceptional advantages such as high energy density, high output power, relatively low self-discharge, etc. However, it has some disadvantages such as safety issues, capacity loss, and expensive manufacture. LIB is composed of three main components: electrolytes, positive and negative electrodes. Researchers have been working on improving the performance of LIB for the past decade, but only a few have focused on investigating the electrolytes at the molecular level. In addition, the molecular mechanisms behind the macroscopic properties of LIB are yet to be explored. The vibrational stretch of the solvent molecule is selected as the infrared probe in order to investigate the structure and dynamics in LIE at the molecular level via linear and non-linear infrared spectroscopies. Ultrafast laser spectroscopy has emerged as a powerful tool of studying the structure and dynamics at the molecular level because it offers unique advantages of time and frequency resolutions. DFT calculation, classical and ab initio MD simulations are also employed to assist the interpretation of experimental data. Three projects of LIE are detailed in this dissertation. The first project focused on lowering the flammability of the electrolyte by replacing carbonate solvent with urea solvent, where it is found that the molecular interactions in urea-based electrolytes are similar to the carbonate-based electrolytes. The aim of second project was to reveal the molecular mechanism behind the dynamics of solvent molecules around Li ion in acetonitrile-based electrolytes, where it is shown that the angle between Li ion and acetonitrile plays the most important role in the molecular dynamics around Li ion. The last project investigated a less conventional LIE, which is the concentrated electrolyte composed of Li sulfonylimide salt and acetonitrile, where a highly correlated network is proposed to form in the

mixtures. In addition, the molecular origin of the macroscopic properties in a family of concentrated electrolytes is studied through both experimental and theoretical methods.

CHAPTER 1. INTRODUCTION TO LITHIUM ION ELECTROLYTES

Lithium ion batteries (LIB) have dominated the energy storage market for past decade. Due to the exclusive advantages of LIB such as high energy output, high energy density and low self-discharge, they have been employed in a variety of devices ranging from mini storage devices to electric household to electric vehicles.[1] The technology of LIB still has room for improvement in order to reach better battery performance. Some problems of LIB are yet to be solved, such as safety issues, relatively high cost and poor durability.[2-4] A basic rechargeable LIB is composed of an ion-conducting electrolyte, two electrodes, and a separator.[1] The electrolyte, as one key component of LIB, has direct relation with the durability, flammability and conductivity of the battery.[5] Conventional electrolyte is constituted by a mixture of cyclic and linear carbonate solvents with ~1 M lithium salt.[6] While many researchers have focused on optimizing the materials of electrodes or the compositions of electrolytes, only a few studied the electrolytes and the conduction mechanism of electrolytes at the molecular level. In addition, some novel types of electrolytes have been proposed as possible replacement for conventional electrolytes in order to solve the safety issues and enhance the durability of LIB, one of which is the highly concentrated electrolyte, where the Li ion (Li+) concentration is increased to ~4 M.[7-9] Such concentrated solutions of Li salt and organic solvents have less safety issues, relatively high conductivity, and unusually high stability.[10] The origin of the interesting properties of concentrated electrolytes is still unclear. More investigations on the conventional and novel electrolytes at the molecular level are expected in the future to further optimize the performance of LIB.

1.1. Overview of LIB

1.1.1. History

The foundation of LIB was laid during 1970s.[1] The first battery was not rechargeable after the initial discharging, where the negative electrode was lithium and the positive electrode was manganese dioxide. Later in 1985, the first rechargeable battery was introduced to the market by Moli Energy, where the lithium and molybdenum sulfide were used as the negative and positive electrodes, respectively. Onto the next step, the lithium was replaced by a petroleum coke for the anode and the metal sulfide was replaced by a metal oxide for the cathode. Up to this point, a high voltage potential of LIB and the intercalation/de-intercalation of lithium on the surface of electrodes were enabled by the proper electrode materials.[1] Based on this prototype of LIB, Sony developed the first commercial rechargeable LIB and introduced it on the market in 1991.[11] In past decade, LIB have revolutionized our lives and laid the foundation of a wireless, and fossil fuel-free society. In 2019, John B. Goodenough, M. Stanley Whittingham and Akira Yoshino were awarded the Nobel Prize in Chemistry for their great contributions to the development of LIB during 1970s to 1980s.[12]

1.1.2. Components, performance and applications

A basic LIB should be composed of two electrodes, an ion-conducting electrolyte and a separator between the electrodes. In the electrolyte, lithium ions migrate back and forth between the anode and the cathode through the separator during charging and discharging processes, and get intercalated into the active materials on the surface of electrodes. Simultaneously, electrons move between two electrodes via an outer electrical connection, like a cable, as the electricity carriers.[1] The intercalation/de-intercalation of Li ions has significant importance for the performance of rechargeable battery.[13, 14] For example, when excess amount of Li ions

accumulates on the electrode surface, the ions form Li dendrites that can puncture the separator and short-circuit the cell, leading to the battery failure.[15, 16] Compared to other cations, Li ion is very small, allowing for a great number of intercalation compounds. Such property of the Li ion enables the wide electrochemical window from -3 V to more than 2 V vs. standard hydrogen electrode (SHE).[17]

Depending on the materials used to make the battery, LIB have different performance. In general, a LIB can have an energy density ranging from 250 to 693 Wh/L,[18] a specific power density ranging from 300 to 1500 W/kg,[19] and a cycle life between 400 and 1200.[20] In addition, the efficiency of LIB is very high, usually above 90%.[21] The high energy density, the long cycle life, and the light weight have made LIB the undisputed champion among all rechargeable batteries.

LIB were first used in mobile consumer devices, such as mobile phones, followed by the laptops. In 2000, most of the laptops were powered by LIB, where the battery packs usually consist of 3 to 12 cells.[1] Some other applications are electric household appliances and power tools, such as vacuum cleaner, electric drills and electric mower, with a voltage of 3.6 to 36 V, depending on the usage.[22, 23] In recent years, LIB play a more and more significant role in the electric mobility, such as electric bicycles, electric scooters and electric vehicles.[24-26] This type of LIB is specifically designed for a high ampere-hour capacity.

1.1.3. Advantages and disadvantages

LIB is superior to other types of batteries due to its high specific energy, high specific power, high efficiency during charging and discharging as well as low self-discharge rates.[1] As discussed above, the high performance of LIB has opened many additional markets besides original small electronic devices, such as toys, lighting, medical devices, electric vehicles and

many others.[1, 27] However, there are certain disadvantages of present day LIB, which, if remedied with suitable solutions, could open new applications and expand markets even more. For example, one important topic of LIB manufacturing is to increase capacity and energy with lower cost so that the needs of green and sustainable development of electric vehicles can be fulfilled.[22, 27] A second topic of interest is the specific energy improvement of LIB in order to accelerate the development of many energy storage schemes, e.g. the alternative energy storage devices such as pumped hydro, compressed air, flywheels, etc.[22, 28] Another deficiency of LIB is the safety issues. For example, the short-circuiting of the cell due to the formation of Li dendrites during cycling leads to cell rupture, cell failure or even battery explosion.[29, 30] The last deficiency of LIB requires extensive research regarding the formation of electrolyte-solid interface, the flammability of electrolytes and the development of novel or post-lithium-ion batteries.

1.2. Nonaqueous electrolytes

1.2.1. Components

The electrolyte is a key component of a LIB. The development and investigation of electrolytes can advance the technology of power tools, hybrid electric vehicles and stand-by power sources for communication and modern airplanes.[5, 6] A typical lithium ion electrolyte (LIE) is composed of a Li salt in a mixture of cyclic and linear carbonate solvents. Lithium hexafluorophosphate ($LiPF_6$) was reported to be the predominant salt used for most commercial Li-ion batteries due to its high ionic conductivity, high solubility, and relatively strong stability with the Al current collector and with the electrodes.[5, 31, 32] However, $LiPF_6$ undergoes hydrolysis[33, 34] and has a relatively low thermal stability[35, 36]. The hydrolysis of $LiPF_6$ can produce HF gas and cause cell rupture, which is one of the major issues for the usage of this salt.[37, 38] Some other Li salts were also established and have been used previously for LIE, which

include lithium perchlorate ($LiClO_4$), lithium hexafluoroarsenate ($LiAsF_6$), lithium tetrafluoroborate ($LiBF_4$) and lithium bis(trifluoromethanesulfony)imide (LiTFSI).[6, 31, 39] $LiClO_4$ was widely used for electrolyte research due to its comparable electrochemical properties to $LiPF_6$.[5, 40] However, the salt cannot passivate the Al current collector and thus are limited to the usage in research aspects.[32, 41] $LiAsF_6$ was also used frequently for electrolyte research due to the improvement of efficiency of Li metal plating/stripping.[5, 31, 42] However, the potential hazards associated with the As element have prevented its use in commercial batteries.[43] $LiBF_4$ is less susceptible to hydrolysis and more thermally stable as compared to $LiPF_6$.[44, 45] The electrolyte with $LiBF_4$ is also proven to have improved cell cycling performance at extreme temperature when compared with $LiPF_6$ electrolytes.[46, 47] However, the significantly lower conductivity of $LiBF_4$ has made it commercially unfavorable.[46, 48] LiTFSI is a rather interesting salt. The sulfonylimide anion is a fluorinated anion with two low-energy conformations (cis and trans).[49, 50] The strongly electron-withdrawing fluorine atoms and resonance structures arising from the sulfonyl groups result in an extensive charge delocalization across the backbone of the anion.[51, 52] Electrolytes with LiTFSI are shown to have high thermal stability and are not susceptible to hydrolysis.[40, 53] However, LiTFSI electrolytes have relatively low conductivity[54, 55] and are known to corrode the Al current collector at high potential[56, 57], which again limits its usage in commercial batteries.

As for the organic solvent, usually a mixture of cyclic carbonate, such as ethylene carbonate (EC) and propylene carbonate (PC), and linear carbonate, such as dimethyl carbonate (DMC), ethyl methyl carbonate (EMC) and diethyl carbonate (DEC), is utilized in the commercial LIB.[5, 6] The cyclic carbonates have high dielectric constant and high viscosity, while the linear carbonates have low dielectric constant and low viscosity.[58] The mixture of cyclic and

linear carbonates help achieve the optimal performance of batteries due to the synergetic effects of the cyclic and linear solvents. Carbonates are selected as the universal solvent because they can make Li ion solutions with high electrolytic conductivity, high electrochemical stability, relatively high safety, and stable electrode-electrolyte interface.[5, 6] Besides carbonate solvents, some new solvents were introduced in the literature in order to improve the battery performance, e.g. fluorine-containing[6, 59], boron-containing[60, 61], phosphorous-containing[62, 63], and sulfur-containing organic solvents[64, 65]. Some other solvents like acetonitrile and urea were also reported as possible replacement for the carbonate, which can make electrolytes with less safety issues.[66-68]

1.2.2. State-of-the-art research of LIE

In the state-of-the-art research of LIB, most of the investigations focused on the materials or performance of electrodes and battery cells,[69, 70] while only some of them studied the electrolytes at a nanoscopic level.[71, 72] The performance of LIE is usually evaluated by the conductivity, viscosity and electrochemistry window of the Li ion solutions.[73] To better understand the function of LIB, molecular level research on the electrolytes is required, which has direct relation to the formation of electrolyte-solid interface. Typical electrolytes are composed of Li salts (usually ~1 M) dissolved in a mixture of linear and cyclic carbonate solvents.[5] Thus, carbonate solvents have been studied extensively in the literature regarding the electrochemical properties and the molecular interactions in the carbonate/Li+ solutions.[74-76] To be more specific, the interactions between Li ions and organic solvents are of special interest because the microscopic properties of electrolytes are dependent on the solvation shell of Li+. The functional groups of solvent molecules can serve as good probes in spectroscopies such as

Raman and infrared, where the signals of molecules in different environment can be identified in spectra according to stark effect.[66, 77, 78]

It is universally accepted that each Li+ is coordinated by four solvent molecules in solutions with low Li+ concentration, forming a tetrahedral arrangement.[77, 79, 80] (Figure 1.1) In the case of carbonate-based electrolytes, coordination bonds are formed between Li+ and the oxygen of carbonyl groups while the interactions between Li+ and the ester oxygen are minimal.[71, 77] The Li+ first solvation shell is solvated by more solvent molecules in the surrounding that is named as second solvation shell, which can influence the structure and dynamics of the first solvation shell.[66, 81] However, most properties of the solutions are controlled by the first solvation shell so the second solvation shell is usually neglected. For example, it is shown that the conductivity of a dilute electrolyte has direct relation to the diffusion of the Li+ first solvation shell, where faster diffusion indicates higher conductivity.[6, 82]

Besides the free ion solvation shell in the tetrahedral arrangement, other types of ionic species can play a role in the performance of the electrolytes. Some common ionic species are contact ion pairs (CIP), solvent separated ion pairs (SSIP) and aggregates.[81, 83, 84] (Figure 1.1) Each CIP is composed of a Li+, an anion and typically three solvent molecules. For example, it is demonstrated in the cyclic carbonate solutions with $LiPF_6$, CIP are formed between Li+ and PF_6^- ions due to the strong affinity of counterions to the cations.[77, 81] Another example of CIP is for the lithium thiocyanate (LiSCN) solutions, where almost all thiocyanate ions (SCN^-) coordinate Li+ even in the dilute solution of acetonitrile.[85] SSIP is different from the CIP because there is no direct interaction between cation and anion. Instead, the anion solvates the free ion solvation shell and has indirect interaction with the Li+ from a short distance. Due to the indirect interaction between ions, SSIP are usually hard to detect because the signals are convoluted with

or similar to those of free ion solvation shells. A Raman study of carbonate-based electrolytes claims that the SSIP can be resolved in the anion-bond stretching region of Raman spectra.[78] However, most researches have shown that SSIP cannot be discerned from the free ion solvation shells. Lastly, aggregates are easier to distinguish experimentally. Aggregates are composed of more than two ions that interact with multiple solvent molecules. The signature peaks of aggregates are shifted from those of free ion solvation shell and thus easy to detect via spectroscopies.[83, 84] Three types of ionic species discussed above are considered as unfavorable forms of Li+ solvation because they can slow down the diffusion of first solvation shells and consequently lead to a decrease in the conductivity of dilute electrolytes.[6, 86]

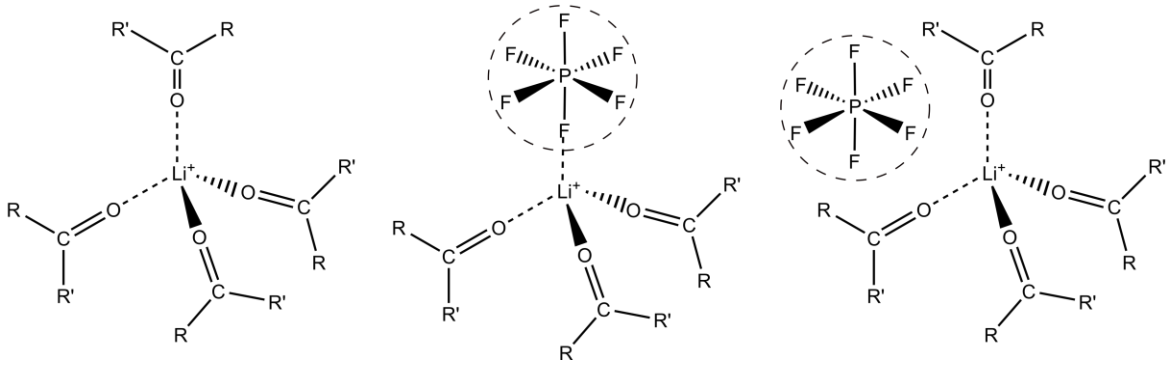

Figure 1.1. Chemical structures of free ion solvation shell (left), contact ion pair (middle), and solvent separated ion pair (right).

Besides the conventional electrolytes with a Li+ concentration of ~1 M, the highly concentrated electrolytes with a ~4 M Li+ concentration are established as novel electrolytes that have high stability and less safety issues compared to the dilute electrolytes.[9, 10, 87] In highly concentrated electrolytes, the molar ratio of Li+:solvent is in the range of 1:3 to 1:1.5. It is shown that concentrated electrolytes have relatively low, but fairly high conductivity compared to dilute electrolytes, considering the very high molar ratio of Li+:solvent.[10, 88, 89] In addition, an unusually high stability is found in the concentrated electrolytes, where the corrosion of

electrodes and the flammability of the electrolyte are very much limited.[10] When the molar ratio of Li+:solvent is around 1:2, each Li+ can only be coordinated by at most two solvent molecules. Thus, the anions have direct interaction with cations in order to fulfill a coordination number of four. Clearly, the ionic species in concentrated electrolytes should be dominated by contact ion pairs rather than free ion solvation shells. It is also found that the anions will be oxidized first instead of solvent molecules and then form a protective layer on the surface of electrode, which again benefits the stability of electrolytes.[90, 91] However, the molecular origin of the favorable properties of concentrated electrolytes is yet unknown. Further investigations regarding the mechanisms of the performance of concentrated electrolytes are required in order to obtain a molecular understanding of such novel systems.

1.2.3. Our interests in Li ion solvation shell

My research on Li ion electrolytes focused on the physical aspects of molecular interactions in the solutions, especially the solvation shell of Li+. As stated previously, four solvent molecules coordinate a Li+ in a tetrahedral arrangement in the first solvation shell. The structure of the Li+ first solvation shell in dilute electrolytes is one of the main topic in this research. Carbonate-based electrolytes have been studied extensively by our group and other research groups.[71, 72, 74, 77, 81, 83] It is shown that in dilute electrolytes, most Li+ form first solvation shells exclusively with solvent molecules, while a small amount can interact with the anions and form CIP, SSIP or aggregates.[77, 81] In addition, the ionic species formed have relation to the structure of the solvent molecules. For example, CIP and SSIP are proven to exist in the electrolytes of cyclic and linear carbonates, respectively.[77, 81] It is also demonstrated that the degree of dissociation of the Li salt plays an important role in the formation of first solvation shells.[67, 92, 93] For instance, LiTFSI and LiSCN are shown to form free ion solvation shell and

CIP, respectively, in the dilute solutions of acetonitrile.[85] The speciation of ionic species is meaningful for understanding the ion transport and solvent-ion interactions in the electrolytes, and thus has been studied via linear and non-linear infrared spectroscopies with the assistance of computational tools.[81, 83]

The dynamics of the Li+ first solvation shell in dilute electrolytes is another topic of our interest. The molecular motions of the solvation shells have significant meaning for studying the local interactions between Li+ and solvent molecules, as well as among the nearby coordinated solvent molecules in the same solvation shell. Because the molecular motions in solutions happen on the femto- to pico-second time scale, ultrafast laser pulses and time-resolved spectroscopy are required for such investigation. Our group employs two-dimensional infrared spectroscopy (2DIR) as the key technique in order to probe the ultrafast dynamical processes in LIE.[66, 74, 77] Ab initio molecular dynamics simulation (AIMDS) is occasionally used to interpret the experimental data as well.[81] Rick's and Rempe's groups demonstrated that polarizable or quantum-based force fields or quantum models are required to accurately model the properties of Li+ solutions. Thus, compared to classical MD simulation, AIMDS should be more appropriate for the investigation of dynamics and structure in LIE.[94, 95] In the literature, it is shown by both experiments and simulations that the local motions within the Li+ first solvation shell is on the order of a few to tens of picosecond[66, 77, 81], while the diffusion of the solvation shell is relatively slower but still within the time scale of picosecond to nanosecond[96, 97]. The molecular motions and dynamics around Li+ are related to the distances and angles between coordinated solvent and Li+, or the angles between two coordinated solvent molecules.[74, 85] Interestingly, due to the large magnitude of the transition dipole of carbonyl stretch, the coordinated carbonates in the same solvation shell are vibrationally coupled, which results in highly convoluted IR spectra that are

hard to interpret in terms of individual molecules.[66, 77] In order to investigate the molecular mechanisms of the deformation dynamics in the first solvation shell, AIMDS and DFT calculations were utilized to decipher the coupling among coordinated molecules.[81, 85] It is illustrated that the dynamics of deformation is dominated by the energy transfer among the coupled states of carbonyl groups due to the excitonic nature of the carbonyl stretches.[66, 77] The exchange of coordinated and free solvent molecules was also investigated experimentally and theoretically, where the dynamics of solvent exchange is found to be on the order of tens of picosecond.[77, 81]

Besides dilute electrolytes, highly concentrated electrolytes are also of our interest. As stated in previous section, the molecular interactions in concentrated electrolytes differ very much from those in dilute electrolytes, considering the different composition of Li+ solvation shell.[90, 98] In order to reach such a high concentration, LiTFSI was extensively used for electrolyte preparation due to its high solubility in organic solvents.[88, 99] This high solubility of LiTFSI has relation to the delocalized charge among the backbone of TFSI- and the four oxygen atoms from the sulfonyl groups. In concentrated solutions of LiTFSI, the TFSI- directly interacts with Li+ through its oxygen atoms, where four oxygen atoms can at most coordinate two Li ions. There are two universally adopted configurations of the LiTFSI contact ion pairs.[98, 100] (Figure 1.2) One is named the bidentate form, where two oxygen atoms of the TFSI- coordinate the same Li+, while two solvent molecules join in the same solvation shell to fulfill four coordination bonds around the Li+. The other is named the monodentate form, in which only one oxygen of TFSI- interacts with the Li+, and three solvent molecules participate in the solvation shell to fulfill a coordination number of four. Thus, the dynamics and structure of Li+ first solvation shell in concentrated solutions can be significantly different from those in dilute electrolytes, arising

from strong ion-ion interactions in concentrated solutions. In fact, researchers have found out that the ion-ion interactions dominate the microscopic properties of electrolytes, where the deformation dynamics of first solvation shell is obviously slowed down and a system with high correlation among ions has formed.[10, 98] In addition, the making and breaking of coordination bonds between Li+ and the anion is likely to be the conduction mechanism for concentrated electrolytes, which is also known as ion hopping mechanism, rather than the diffusion of the first solvation shell as discussed for dilute electrolytes.[101, 102] In my research, linear and non-linear spectroscopies together with DFT and AIMDS were used to study the speciation and dynamics of Li+ first solvation shell. Furthermore, the effects of the anion were studied by comparing the results of three different salts in the same family with increasing anion size, which can offer more insights into the ion-ion interactions and the molecular origin of the macroscopic properties in concentrated solutions.

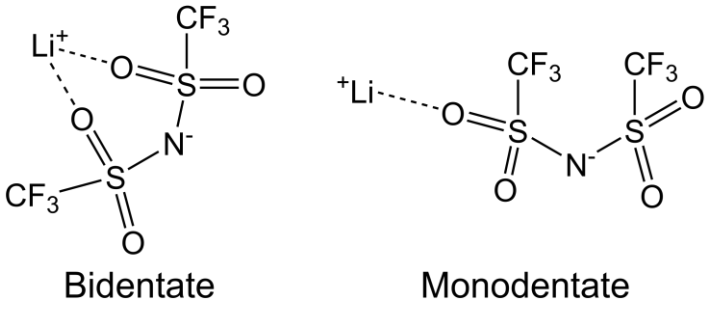

Figure 1.2. Two configurations of LiTFSI coordination. On the left side, two oxygen atoms of TFSI- coordinate the same Li+, which is named as the bidentate form. On the right side, one oxygen atom of TFSI- coordinates the Li+, which is named as the monodentate form.

CHAPTER 2. THEORY OF LINEAR AND NON-LINEAR SPECTROSCOPIES

Infrared spectroscopy is a powerful tool for determining sample composition, studying energetics and investigating molecular structures. While linear infrared spectroscopy has been widely used since the 1950s, non-linear infrared spectroscopic techniques such as two-dimensional infrared spectroscopy (2DIR) have only emerged recently.[103-107] 2DIR is a third-order non-linear spectroscopy technique that can investigate vibrational modes in condensed-phase systems. The advantages of 2DIR, such as high-resolution spectra and time-dependent measurements, enable the investigation of the structure and dynamics of vibrational probes at the molecular level.[108-110] In this chapter, an outline of essential physical phenomena in 2DIR is first provided, where the mathematical formalism of the optics is discussed regarding the interpretation and design of multiple-pulse or 2DIR experiments. The mathematical methodology is then applied to predict the lineshape and cross-peak patterns, depending on the experimental setup selected for the measurement of 2DIR spectra. The 2DIR spectra can assist in gaining structural information such as vibrational coupling and anharmonicities, as well as the dynamical information such as molecular motions and energy transfer, which all happen on a femtosecond (fs) to picosecond (ps) time scale.[111-115] The generation of ultrafast laser pulses and the setup of the 2DIR experiment are also discussed at the end.

2.1. Eigenstates and emitted electric field for individual molecules

Assume one vibrational mode of a molecule is in the gas phase, isolated from other molecules, and if it is oriented along the z-axis, the real-valued electric field of the light that interacts with the molecule can be written as,

$$\vec{E}(t) = \overrightarrow{E'}(t)cos(\vec{k} \cdot \vec{r} - \omega t + \varphi)$$

Eq. 1

where $\overrightarrow{E'}(t)$ is the pulse envelope that is a vectorial property that includes the information of the pulse polarization, $\vec{k}$ is the wavevector that describes the direction of light propagation, ω is the frequency and φ is the phase. When the pulse is polarized along the z-axis or parallel to the vibrational mode, this equation can be simplified to the following,

$$E(t) = E'(t)\, cos(\omega t)$$

Eq. 2

so the electric field is only dependent on the pulse envelope and the frequency. Here the interaction between light and molecule is treated semiclassically such that the time-dependent electric field is considered classically but the vibrational states of the molecule are considered quantum mechanically. The energy of interaction between molecule dipole $\hat{\mu}$ and the external electrostatic field $\hat{E}$ is,

$$\widehat{W}(t) = -\hat{\mu}E(t)$$

Eq. 3

Note that the electric field and the dipole operator are operators. The total Hamiltonian can be written as

$$\widehat{H} = \widehat{H}_0 + \widehat{W}(t)$$

Eq. 4

where $\widehat{H}_0$ is the Hamiltonian for the isolated vibrational mode, and $\widehat{W}$ is the quantum mechanical operator for the interaction between the laser pulse and the molecule. The time-dependent Schrödinger equation is written as

$$\widehat{H}_0|n\rangle = E_n|n\rangle$$

Eq. 5

where $|n\rangle$ is the molecular eigenstates of $\widehat{H}_0$. The wavefunction $|\Phi\rangle$ of the molecule is time-dependent and governed by the Schrödinger equation, which is represented as,

$$i\hbar\frac{\partial}{\partial t}\big|\Phi\rangle = \widehat{H}\big|\Phi\rangle$$

Eq. 6

Without the external laser pulse, the solution of $\widehat{H}_0$, or the wavefunction $|\Phi\rangle$ becomes,

$$|\Phi\rangle = \sum_n c_n e^{-iE_n t/\hbar}|n\rangle$$

Eq. 7

When the laser pulse interacts with the molecule, the molecule should be in a linear combination of eigenstates as represented by c_n. By substituting Eq. 7 into Eq. 6, the time dependence of c_n is found to be,

$$\frac{\partial}{\partial t}c_m(t) = -\frac{i}{\hbar}\sum_n c_n(t)e^{-i(E_n-E_m)t/\hbar}\big\langle m\big|\widehat{W}(t)\big|n\big\rangle$$

Eq. 8

The wavefunction after interacting with the laser pulse for a duration t can be calculated from Eq. 8. For a two-level system of the ground and first excited states, substituting Eq. 3 and defining $\omega_{01} \equiv (E_1 - E_0)/\hbar$ in Eq. 8, two coupled differential equations obtained are

$$\frac{\partial}{\partial t}c_1(t) = +\frac{i}{\hbar}c_0(t)e^{-i\omega_{01}t}\langle 1|\hat{\mu}|0\rangle E(t)$$

$$\frac{\partial}{\partial t}c_0(t) = +\frac{i}{\hbar}c_1(t)e^{+i\omega_{01}t}\langle 0|\hat{\mu}|1\rangle E(t)$$

Eq. 9

where $\langle n|\hat{\mu}|m\rangle$ is the transition dipole moment which will be referred to as $\hat{\mu}_{\mathrm{nm}}$, and can be written as,

$$\langle n|\hat{\mu}|m\rangle = \frac{d\mu}{dt}\langle n|\hat{x}|m\rangle$$

Eq. 10

In this last expression, x is the coordinate for the vibrating bond, and the $d\mu/dt$ is the change of the static dipole of the molecule when the bond vibrates. Therefore, after the laser pulse, the molecule is in a linear combination of two eigenstates ($|0\rangle$ and $|1\rangle$), or

$$\langle \Phi(t)\rangle = c_0 e^{-iE_0 t/\hbar}|0\rangle + ic_1 e^{-iE_1 t/\hbar}|1\rangle$$

Eq. 11

This is a so-called coherent linear superposition of states, which is also known as a wavepacket, created due to the interaction with the laser pulse. The time dependence of the wavepacket is the time dependence of the isolated molecular Hamiltonian Eq. 7, which is known as the molecular response, $R(t)$. If there were numerous molecules interfered with the laser pulse, they would initially vibrate in phase right after the field interaction. Thus, a nonequilibrium charge distribution in the molecules has been created, which is referred to as macroscopic polarization, $P(t)$. This polarization evolves with time according to the response function in Eq. 11, providing structural and dynamical information for the molecular interaction, solvent environment, energy transfer and other properties. The 2DIR spectroscopy is aimed at measuring the macroscopic polarization, $P(t)$ and extracting the molecular response, $R(t)$. Since the laser field is coupled to the molecule through the interaction term as shown in Eq. 3, it is reasonable that the same coupling term also accounts for the emission of the field. Thus, the macroscopic polarization can be derived as the expectation value of the transition dipole $\hat{\mu}_{\mathrm{nm}}$,

$$P(t) = \langle \mu \rangle = \langle \Phi(t) | \hat{\mu} | \Phi(t) \rangle =$$

$$\left(c_0 e^{iE_0 t/\hbar} \langle 0| - i c_1 e^{iE_1 t/\hbar} \langle 1| \right) \hat{\mu} \left(c_0 e^{-iE_0 t/\hbar} |0\rangle + i c_1 e^{-iE_1 t/\hbar} |1\rangle \right) =$$

$$c_0 c_1 \langle 0|\hat{\mu}|1\rangle \sin(\omega_{01} t) + c_0^2 \langle 0|\hat{\mu}|0\rangle + c_1^2 \langle 1|\hat{\mu}|1\rangle$$

Eq. 12

Here, $\langle 0|\hat{\mu}|0\rangle$ or $\langle 1|\hat{\mu}|1\rangle$ represents the static dipoles of the molecule in the ground or first excited states, they are not time-dependent and can be ignored. In addition, it is most likely that after the laser pulse, $c_0 \ll c_1$, so $c_1 \approx 1$. With above approximations, Eq. 12 becomes[116],

$$P(t) \equiv c_0 c_1 \mu_{01} \sin(\omega_{01} t) \propto +\mu_{01}^2 \sin(\omega_{01} t)$$

Eq. 13

The product of c_0 and c_1 coefficients is dependent on the transition dipole μ_{01}, which is responsible for the time-dependent vibrational dipole. Because the vibrator oscillates at the difference in frequency of the two states $|0\rangle$ and $|1\rangle$, it will emit a field at the fundamental frequency of the vibrator.

According to Maxwell's equations,[117, 118] charged oscillators create an electromagnetic wave with a 90° phase shift from the macroscopic polarization. So based on Eq. 13, the emitted electric field is proportional to $-\mu_{01}^2 \cos(\omega_{01} t)$. From a quantum mechanical perspective, the laser pulse prepares a vibrational coherence after it creates a linear superposition of eigenstates which later radiates. The emitted field can be measured and Fourier transformed into an absorption spectrum, which is known as linear absorption.

If there are more than two eigenstates, such as the overtone state $|2\rangle$, a second pulse can be used in order to couple $|1\rangle$ and $|2\rangle$, hence creating a coherence between $|0\rangle$ and $|2\rangle$. Up to this point, it is validated that by tailoring sequences of pulses, linear superpositions of eigenstates can be created, where an emitted electric field of the eigenstates will assist the study of the system.

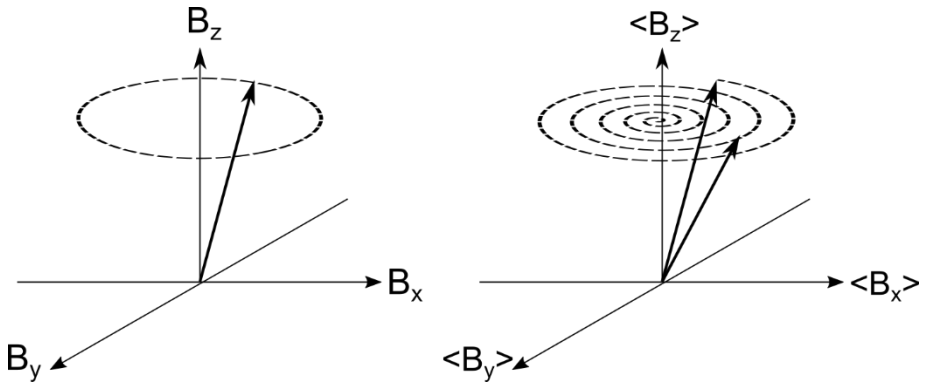

Figure 2.1. Left: vector diagram of Eq. 15 and Eq. 16. The vector precesses around the z-axis. Right: trajectory of a Bloch vector for a molecular ensemble with dephasing. The vector spirals towards the z-axis, while the projections of the vector reduce to zero on the x- and y-axes.

2.2. Bloch vector and density matrix for molecular ensemble

2.2.1. Bloch vector

In the condensed phase, each molecule in the sample is in a slightly different environment from the others, so the same vibrational mode should have different frequencies for different molecules. Under this circumstance, quantum mechanics alone is not sufficient to explain the interference in molecular ensembles. Instead, statistical mechanics is utilized to calculate how the polarizations from an ensemble of molecules interfere with each other and how the macroscopic polarization is created. For instance, the polarization for a system with two molecules can be written as

$$P(t) = c_0^{(1)} c_1^{(1)} \mu_{01} \sin\left(\omega_{01}^{(1)} t\right) + c_0^{(2)} c_1^{(2)} \mu_{01} \sin\left(\omega_{01}^{(2)} t\right)$$

Eq. 14

When a laser pulse interacts with the molecular system, the molecules are in a coherent state. Without the laser pulse, the molecules gradually become out of phase and the polarizations destructively interfere. Thus for a molecular ensemble, the polarization should decay irreversibly.

To clarify the generation of macroscopic polarization, Bloch vector is used to visualize the quantum mechanical coherence. The vector of a molecule in the coherent superposition of quantum states $|0\rangle$ and $|1\rangle$ has been presented in Eq. 11, which is

$$|\Phi(t)\rangle = c_0 e^{-iE_0 t/\hbar}|0\rangle + ic_1 e^{-iE_1 t/\hbar}|1\rangle \equiv c_0(t)|0\rangle + ic_1(t)|1\rangle$$

Eq. 15

The three components of the Bloch vector can be defined as

$$B_z(t) = c_0(t)c_0^*(t) - c_1(t)c_1^*(t)$$

$$B_x(t) = i\big(c_0(t)c_1^*(t) - c_0^*(t)c_1(t)\big) = c_0 c_1 \sin(\omega_{01} t)$$

$$B_y(t) = c_0(t)c_1^*(t) + c_0^*(t)c_1(t) = c_0 c_1 cos(\omega_{01} t)$$

Eq. 16

which is shown in Figure 2.1. In this case, right after the laser pulse ($t = 0$), the vector lies in the (z, y)- plane at an angle depending on the strength of the pulse. As time progresses, it precesses around the z-axis, which is responsible for the emitted field. Note that the macroscopic polarization P is proportional to the B_x as presented by Eq. 13 and Eq. 16. The coherence of the state is enclosed in B_x and B_y while the population of the state is included in the B_z.

The concept of Bloch vector can be applied to a molecular ensemble where the molecules have slightly different frequencies. In this case, the macroscopic polarization $P(t)$ is the sum of the individual projection B_x of each molecule s,

$$P(t) = \langle \mu \rangle = \langle B_x \rangle = \sum_s ip_s\big(c_0^s(t)c_1^{s*}(t) - c_0^{s*}(t)c_1^s(t)\big)$$
$$= i(\langle c_0(t)c_1^*(t)\rangle - \langle c_0^*(t)c_1(t)\rangle)$$

Eq. 17

The brackets in above equation represent an ensemble average and p_s weights the contribution of each molecule. In this method, the three components of the averaged vector can be derived as

$$\langle B_z \rangle = \langle c_0(t)c_0^*(t) \rangle - \langle c_1(t)c_1^*(t) \rangle$$

$$\langle B_x \rangle = i(\langle c_0(t)c_1^*(t) \rangle - \langle c_0^*(t)c_1(t) \rangle)$$

$$\langle B_y \rangle = \langle c_0(t)c_1^*(t) \rangle + \langle c_0^*(t)c_1(t) \rangle$$

Eq. 18

When the molecules in the sample have a distribution of frequencies that are not dependent on time, such distribution is said to be inhomogeneous. When the frequencies of a molecular ensemble are time-dependent, the frequency fluctuations lead to dephasing and the distribution of frequencies is said to be homogenous. Both inhomogeneous and homogeneous dynamics can cause a decay of macroscopic polarization in time. As shown in Figure 2.1, the vector spirals towards the direction of $\langle B_z \rangle$ while the projections on $\langle B_x \rangle$ and $\langle B_y \rangle$ decay to zero. The homogeneous and inhomogeneous decays cannot be discerned by linear spectroscopy, so the non-linear spectroscopy such as 2DIR spectroscopy is vital for qualifying dephasing mechanisms through multi-pulse experiments. In addition, the population of the excited states decreases until the wavefunction coefficient $c_0 = 1$ and $c_1 = 0$. Such population relaxation makes $\langle B_z \rangle$ increase until $B_z = +1$ and $B_x = B_y = 0$.

2.2.2. Density matrix

The coherence and dephasing of the molecular ensemble can also be represented by a density matrix. In a vibrational system with two quantum states $|0\rangle$ and $|1\rangle$, the density matrix is defined as,

$$\rho = \begin{pmatrix} \rho_{00} & \rho_{01} \\ \rho_{10} & \rho_{11} \end{pmatrix} = \begin{pmatrix} \langle c_0'(t)c_0'^*(t)\rangle & \langle c_0'(t)c_1'^*(t)\rangle \\ \langle c_1'(t)c_0'^*(t)\rangle & \langle c_1'(t)c_1'^*(t)\rangle \end{pmatrix}$$

Eq. 19

Since $c_0' = c_0$ and $c_1' = ic_1$, Eq. 19 becomes

$$\rho = \begin{pmatrix} \langle c_0(t)c_0^*(t)\rangle & \langle -ic_0(t)c_1^*(t)\rangle \\ i\langle c_1(t)c_0^*(t)\rangle & \langle c_1(t)c_1^*(t)\rangle \end{pmatrix}$$

Eq. 20

The relation between Bloch vector and density matrix representations is,

$$\langle B_z\rangle = \rho_{00} - \rho_{11}$$

$$\langle B_x\rangle = -(\rho_{01} + \rho_{10})$$

$$\langle B_y\rangle = i(\rho_{01} - \rho_{10})$$

Eq. 21

Therefore, the diagonal terms of density matrix are the populations, while the off-diagonal terms are the source of quantum mechanical coherences, which result in the emitted electric field, $E_{sig}(t)$. Without dephasing and population relaxation, the off-diagonal terms evolve with time and are written as,

$$\rho_{00}(t) = c_0^2$$

$$\rho_{11}(t) = c_1^2$$

$$\rho_{01}(t) = -ic_0c_1e^{+i\omega_{01}t}$$

$$\rho_{10}(t) = ic_0c_1e^{-i\omega_{01}t}$$

Eq. 22

When homogeneous dephasing and population relaxation are included, the matrix terms become,

$$\rho_{11}(t) = \rho_{11}(0)e^{-\frac{t}{T_1}}$$

$$\rho_{00}(t) = 1 - \rho_{11}(t)$$

$$\rho_{01}(t) = -ic_0c_1e^{+i\omega_{01}t}e^{-\frac{t}{T_2}}$$

$$\rho_{10}(t) = ic_0c_1e^{-i\omega_{01}t}e^{-t/T_2}$$

Eq. 23

T_1 is the population relaxation time and T_2 is the homogeneous dephasing time. The two times are related by the following,

$$\frac{1}{T_2} = \frac{1}{2T_1} + \frac{1}{T_2^*}$$

Eq. 24

where T_2^* is the pure dephasing time due to the fluctuations of the environment.

The density matrix can be represented by a quantum mechanical operator, $\rho = |\varphi\rangle\langle\varphi|$. The elements in the matrix are found by the expansion of the wavefunction φ^s for each eigenstate:

$$|\varphi^s\rangle = \sum_n c_n^s|n\rangle$$

$$\langle\varphi^s| = \sum_n c_n^{s*}\langle n|$$

Eq. 25

Performing the ensemble average by summing over all molecules gives,

$$\hat{\rho}_{nm} = \langle c_n c_m^*\rangle|n\rangle\langle m|$$

Eq. 26

It is clear that matrix elements are related to a coherence between states $|n\rangle$ and $\langle m|$. It is worth noting that the polarization is calculated by,

$$P(t) = \langle \mu \rangle = \sum_{nm} \langle c_n c_m^* \rangle \mu_{nm} = \sum_{nm} \rho_{nm} \mu_{nm}$$

Eq. 27

The right side of Eq. 27 is the trace of $\rho\mu$,

$$\langle \mu \rangle \equiv Tr(\rho\mu) \equiv \langle \rho\mu \rangle$$

Eq. 28

2.3. Molecular response

2.3.1. Response function

The time evolution of molecular ensemble is discussed in terms of density matrix. The laser pulses interact with the molecules through the transition dipole operator $\widehat{W}(t) = -\hat{\mu}E(t)$ as shown in Eq. 3. In order to evaluate the effect of $\widehat{W}(t)$ on the ensemble of wavefunctions, the density matrix can be time-propagated according to the influence of the time-dependent Hamiltonian during the laser pulse, as shown in Eq. 4. This propagation in time will be further discussed in chapter 2.6. Lineshape of 2DIR spectra.

The transition dipole operator is written as,

$$\mu = \begin{pmatrix} 0 & \mu_{01} \\ \mu_{01} & 0 \end{pmatrix}$$

Eq. 29

Multiplying ρ with μ from both ket and bra sides of ρ describes the interaction of a laser pulse with the molecules. Such procedure can be represented by,

$$\rho^{(1)} = i\big(\mu(0)\rho(-\infty) - \rho(-\infty)\mu(0)\big)$$

Eq. 30

The electric field $E(t)$ is neglected for the moment. The macroscopic polarization is obtained by taking the trace of $\langle \mu(t_1)\rho^{(1)} \rangle$ (Eq. 28), so the linear response function is derived,

$$R^{(1)}(t_1) = i\langle\mu(t_1)\mu(0)\rho(-\infty)\rangle - i\langle\mu(t_1)\rho(-\infty)\mu(0)\rangle$$

$$= i\langle\mu(t_1)\mu(0)\rho(-\infty)\rangle - i\langle\rho(-\infty)\mu(0)\mu(t_1)\rangle$$

Eq. 31

The superscript in $R^{(1)}$ means this is the first term in a perturbative expansion. With the matrix of the response function, the macroscopic polarization of the molecular ensemble can be calculated, which is what infrared spectroscopy detects.

2.3.2. Rotating wave approximation

The role of the electrical field $E(t)$ has been ignored in previous discussion about the macroscopic polarization $P(t)$. $E(t)$ plays a role in $P(t)$ through the perturbation term $\widehat{W}$ of the Hamiltonian. To precisely include $E(t)$ in the polarization, the time-dependent Schrodinger equation should be solved. The linear response theory is used to solve this problem, where the laser pulse is assumed to be weak so that the macroscopic polarization changes linearly with the electric field strength. When the envelope of the electric field is a δ-function in time, or $E'(t) = \delta(t)$, the macroscopic polarization can reproduce the molecular response,

$$P^{(1)}(t) \propto R^{(1)}(t)$$

Eq. 32

With linear response theory, the finite width pulse is treated as a sum of δ-function pulses which gives the pulse envelope $E'(t)$. The first-order response function is convoluted with the laser pulse to calculate the macroscopic polarization,

$$P^{(1)}(t) = \int_0^\infty dt_1 E'(t - t_1) R^{(1)}(t_1)$$

Eq. 33

The electric fields have real values in experiments, but they can be written with positive and negative frequencies as the following,

$$2E'(t)\cos(\omega t) = E'(t)\left(e^{-i\omega t} + e^{+i\omega t}\right) = E(t) + E^*(t)$$

Eq. 34

Substituting Eq. 34 into Eq. 33 gives,

$$P^{(1)}(t) = \int_0^\infty dt_1 (E(t-t_1) + E^*(t-t_1)) R^{(1)}(t_1)$$

Eq. 35

To continue the derivation, the function of linear response is required. As in Eq. 31, there are two terms in the response function. Therefore, the resulting macroscopic polarization should have four combinations of electric fields and molecular responses. When the homogeneous dephasing is added to the first term in Eq. 31, the response function becomes,

$$R^{(1)}(t_1) = i\langle \mu(t_1)\mu(0)\rho(-\infty)\rangle = ie^{-i\omega_{01}t_1}e^{-t_1/T_2}$$

Eq. 36

Assuming the laser field is resonant with the transition ($\omega = \omega_{01}$), the macroscopic polarization for the first term becomes,

$$P^{(1)}(t) \propto ie^{-i\omega t}\int_0^\infty dt_1 E'(t-t_1)e^{-\frac{t_1}{T_2}} + ie^{+i\omega t}\int_0^\infty dt_1 E'(t-t_1)e^{-\frac{t_1}{T_2}}e^{-i2\omega t_1}$$

Eq. 37

The first term of Eq. 37 is slowly varying as a function of time t_1, while the second term is highly oscillating. Thus, the second integral is much smaller than the first. When the smaller term is ignored, this method is named the rotating wave approximation (RWA). With this approximation, it is found that $E(t)$ creates the coherence and the linear polarization is represented by one term only:

$$P^{(1)}(t) = \int_0^\infty dt_1 E(t-t_1) e^{-\frac{t_1}{T_2}} R^{(1)}(t_1)$$

Eq. 38

while the term interacting with $E^*(t-t_1)$ disappears. The same calculation is applied to the second term of Eq. 31,

$$R^{*(1)}(t_1) = i\langle \rho(-\infty)\mu(0)\mu(t_1)\rangle = -ie^{+i\omega_{01}t_1}e^{-t_1/T_2}$$

Eq. 39

It is found that only $E^*(t-t_1)$ generates the coherence while $E(t-t_1)$ vanishes. RWA is useful for studying the evolution of ground and excited states because it offers an approximate analytic solution for the time-dependent Schrodinger equation.[107]

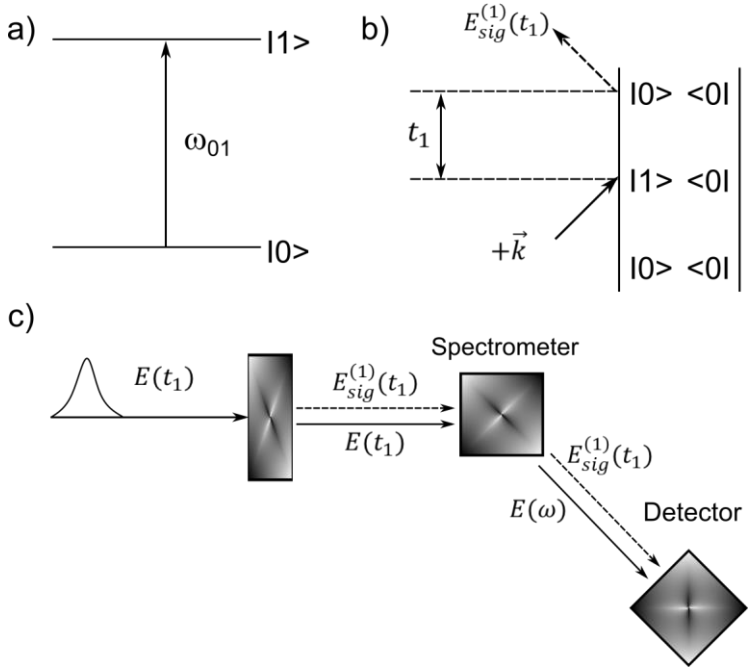

Figure 2.2. a) The transition between two vibrational states, $|0\rangle$ and $|1\rangle$, with a transition frequency of ω_{01}, considered for linear spectroscopy. b) Feynman diagram for the two vibrational states. An electric field is applied on the sample, which is followed by an emission of the electric field from the sample after a duration of time, t_1. c) A schematic of the typical experimental setup for linear spectroscopy. An electric field is applied on the sample as an input, followed by an emission of the electric field from the sample as the output. Both electric fields go through the spectrometer and then the detector to collect IR spectra of the sample.

2.4. Linear spectroscopy

For the linear spectra measured by weak infrared light, there are two vibrational states and one Feynman diagram to consider (Figure 2.2). Before the infrared light, meaning at negative times, the system is in the ground state. At $t = 0$, the off-diagonal element of the density matrix is generated, which depends on the transition dipole moment,

$$\rho_{10} = \rho_{01} \propto i\mu_{01}$$

Eq. 40

It was discussed in Eq. 23 that ρ_{10} oscillates at the frequency ω_{01} and decays with the homogeneous lifetime T_2,

$$\rho_{10} \propto i\mu_{01} e^{-i\omega_{01} t_1} e^{-t_1/T_2}$$

Eq. 41

After a time period t_1, the first-order response of the system due to the interaction with the infrared light can be derived from $\langle \mu \rangle \equiv Tr(\rho \mu_{01})$, which is,

$$R^{(1)}(t_1) \propto i\mu_{01}^2 e^{-i\omega_{01} t_1} e^{-t_1/T_2}$$

Eq. 42

The superscript of $R^{(1)}$ indicates that it is the first term in the general response function. $R^{(1)}$ is convoluted by the envelope of the laser pulse in order to create a macroscopic polarization in the sample,

$$P^{(1)}(t) \propto \int_0^\infty dt_1 R^{(1)}(t_1) E(t - t_1)\, e^{-i\omega(t-t_1) + i\vec{k}_1\vec{r} + i\phi}$$

Eq. 43

The emitted field has a 90° phase shift from $P^{(1)}(t)$,

$$E_{sig}^{(1)} \propto iP^{(1)}(t)$$

Eq. 44

The molecular response of the system is the aim of measurement because it encloses information about the molecules. Since the homogeneous lifetime T_2 is usually in the range of 1-5 ps, femtosecond pulses are needed to measure the molecular response. The necessity of using femtosecond infrared pulses is the main reason that 2DIR has just become practical in the past decades. Notice that the wavevector $\vec{k}_1$ in Eq. 43 has a directionality into the density matrix, where the maximum of the signal is obtained when $\vec{k}_s = \sum \vec{k}_n$.

In linear spectroscopy, the electric field is emitted in the same direction as the incident beam $\vec{k}_s = \vec{k}_1$. (Figure 2.2) A spectrometer is used for the detection in the direction of the emitted field. The spectrometer performs a sequence of operations on the electric fields, where the electric field is initially Fourier transformed and then has its magnitude squared. The detected signal of the electric field after the operations of the spectrometer is written as,

$$S(\omega) \propto \left| \int_0^\infty \left\{ E(t) + E_{sig}^{(1)}(t) \right\} e^{i\omega t} dt \right|^2$$

$$\propto I_0(\omega) + 2\Re\left(\int_0^\infty E(t) e^{i\omega t} dt \cdot \int_0^\infty E_{sig}^{(1)}(t) e^{i\omega t} dt \right) + I_{sig}^{(1)}(\omega)$$

$$\approx I_0(\omega) + 2\Re\left(E(\omega) \cdot E_{sig}^{(1)}(\omega) \right).$$

Eq. 45

$I_{sig}^{(1)}(\omega)$ is the spectrum of the signal $E_{sig}^{(1)}$, which is much smaller than the spectrum of laser pulse $I_0(\omega)$, so it is ignored. The interference term of $E(\omega) \cdot E_{sig}^{(1)}(\omega)$ is due to the heterodyne between emitted field and incident pulse, which should be isolated in order to obtain the information of

the molecules. To achieve this purpose, the absorbance of the sample is calculated by subtracting the spectrum of the laser pulse to the first order,

$$S'(\omega) \equiv -\log\frac{S(\omega)}{I_0(\omega)} \approx 2\Re\left(E(\omega)\cdot E_{sig}^{(1)}(\omega)\right)$$

Eq. 46

Assuming the laser pulse is simply a δ-function in time, the interference term reduces to only the Fourier transform of the emitted electric field, $E_{sig}^{(1)}(\omega)$. Substituting the molecular response $R^{(1)}(t_1)$ from Eq. 42 into Eq. 46 gives the signal as the following,

$$S'(\omega) = 2\Re\int_0^\infty iR^{(1)}(t)e^{i\omega t}dt \propto \Re\int_0^\infty \mu_{01}^2 e^{i(\omega-\omega_{01})t_1}e^{-\frac{t_1}{T_2}}dt_1 \propto \Re\,\mu_{01}^2\frac{1}{i(\omega-\omega_{01})-1/T_2}$$

Eq. 47

After heterodyned with the laser pulse, only the real part of the signal can be obtained, which possesses a Lorentzian lineshape:

$$A(\omega) \propto \mu_{01}^2\frac{1/T_2}{(\omega-\omega_{01})^2+1/T_2^2}$$

Eq. 48

This is called the absorptive part of the band. The full width at half maximum (FWHM) is simply,

$$\Delta\nu = \frac{\Delta\omega}{2\pi} = \frac{1}{\pi T_2}$$

Eq. 49

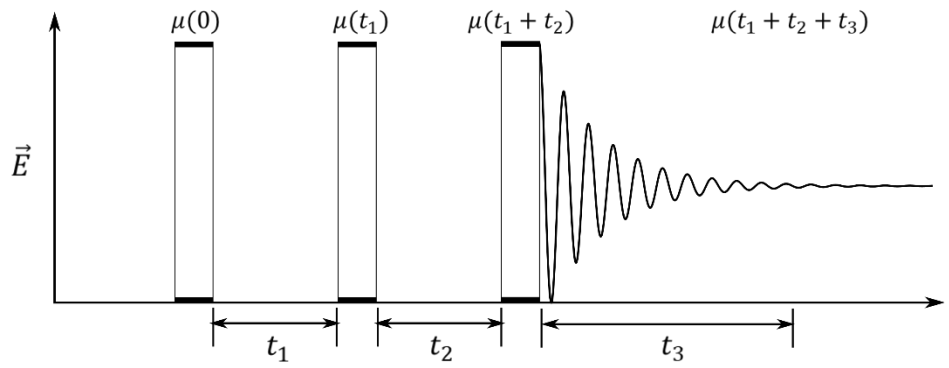

Figure 2.3. Sequence of pulse interactions with dipoles in 2DIR experiment. Three pulses, represented by μ(0), μ(t1), and μ(t1+t2), are used to generate the photon echo from the sample. The time separation between first and second pulses is t1, while the time separation between second and third pulses is t1+t2. The photon echo can be collected after a time duration of t1+t2+t3.

2.5. Non-linear spectroscopy

In non-linear spectroscopy of 2DIR, the emitted field is generated by third-order response functions. The non-linear response function can be derived in a similar way as the linear response function. The pulse sequence for the 2DIR experiment is shown in Figure 2.3. At time $t = 0$, a ρ_{10} off-diagonal matrix element of the density matrix is generated as shown in Eq. 40. During time t_1, the density matrix of the system can be represented by Eq. 41. At time $t = t_1$, a population state is generated by the interaction with the second pulse,

$$\rho_{11} \propto i\mu_{01}^2 e^{-i\omega_{01}t_1} e^{-t_1/T_2}$$

Eq. 50

During time t_2, the population state undergoes a population relaxation with a decay time T_1,

$$\rho_{11} \propto i\mu_{01}^2 e^{-i\omega_{01}t_1} e^{-t_2/T_2} e^{-t_1/T_1}$$

Eq. 51

At $t = t_1 + t_2$, the system interacts with the third pulse and is switched back to a coherent state which dephases during time t_3,

$$\rho_{10} \propto i\mu_{01}^3 e^{-i\omega_{01}t_1} e^{-t_1/T_2} e^{-t_2/T_1} e^{-i\omega_{01}t_3} e^{-t_3/T_2}$$

Eq. 52

At $t = t_1 + t_2 + t_3$, the third-order response function produces the macroscopic polarization and the emitted signal field, as given by $\langle \mu \rangle \equiv Tr(\rho\mu_{01})$,

$$R_4(t_1, t_2, t_3) \propto i\mu_{01}^4 e^{-i\omega_{01}t_1} e^{-t_1/T_2} e^{-t_2/T_1} e^{-i\omega_{01}t_3} e^{-t_3/T_2}$$

Eq. 53

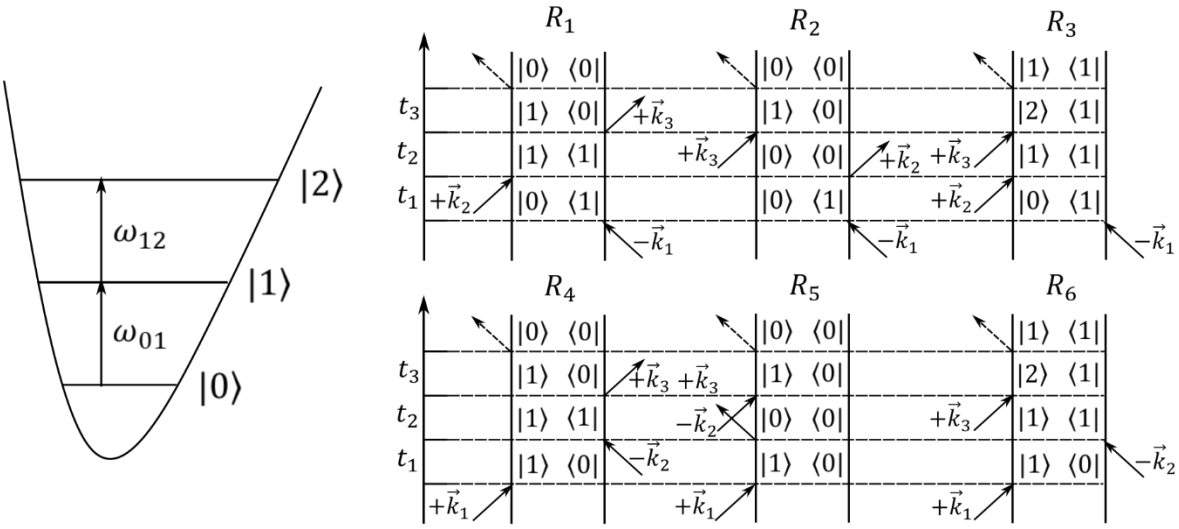

Figure 2.4. Left: energy potential for an anharmonic oscillator with three quantum states, $|0\rangle$, $|1\rangle$ and $|2\rangle$. The transition frequencies are ω_{01} and ω_{12} for the transition from $|0\rangle$ to $|1\rangle$, and $|1\rangle$ to $|2\rangle$, respectively. Right: six Feynman diagrams for third-order non-linear response functions starting from the ground state $|0\rangle\langle 0|$. Rephasing and non-rephasing diagrams are shown in top and bottom panels, respectively. In each diagram, three pulses are used to generate the third-order nonlinear response from the sample. Three pulses are represented by $\vec{k}_1$, $\vec{k}_2$ and $\vec{k}_3$. Details of the diagrams are illustrated in the text.

The third-order response of molecules can be achieved by multiple pathways as shown in the double-sided Feynman diagrams of Figure 2.4. The other five Feynman pathways can be generated by the same procedure. For example, the Feynman diagram R_1 is found to be,

$$R_1(t_1,t_2,t_3) \propto i\mu_{01}^4 e^{+i\omega_{01}t_1} e^{-t_1/T_2} e^{-t_2/T_1} e^{-i\omega_{01}t_3} e^{-t_3/T_2}$$

Eq. 54

where the element oscillates as the complex conjugate of R_4 during time t_1. It turns out that R_2 and R_1, or R_5 and R_4, have the same sequences of coherences, so $R_2 = R_1$, $R_5 = R_4$. On the other hand, the pathways R_3 and R_6 involve the overtone state $|2\rangle$. The corresponding response functions are,

$$R_3(t_3,t_2,t_1) \propto i\mu_{01}^2\mu_{12}^2 e^{+i\omega_{01}t_1 - t_1/T_2^{(01)}} e^{-t_2/T_1} e^{-i\omega_{12}t_3 - t_3/T_2^{(12)}}$$

$$R_6(t_3,t_2,t_1) \propto i\mu_{01}^2\mu_{12}^2 e^{-i\omega_{01}t_1 - t_1/T_2^{(01)}} e^{-t_2/T_1} e^{-i\omega_{12}t_3 - t_3/T_2^{(12)}}$$

Eq. 55

It is worth noting that in the vector representations of R_1, R_2 and R_3, the individual vectors rephase after time t_3 ($t_3 = t_1$) to reproduce the macroscopic polarization of the ensemble. The reappearance of the polarization is called a photon echo. Thus R_1, R_2 and R_3 are rephasing pathways. Due to the lack of such photon echo, R_4, R_5 and R_6 are called non-rephasing pathways. The rephasing diagrams are emitted in the direction of $-\vec{k}_1 + \vec{k}_2 + \vec{k}_3$, while the non-rephasing diagrams are emitted in the direction of $+\vec{k}_1 - \vec{k}_2 + \vec{k}_3$. In fact, by switching the time ordering of first two pulses, the rephasing and non-rephasing responses can be easily achieved. In most general form, a 2DIR experiment applies a beam geometry where the laser pulses have different wavevectors from the directions of $\mp\vec{k}_1 \pm \vec{k}_2 + \vec{k}_3$, so that the output field can be emitted noncollinearly with any input fields. Such a phase matching direction is shown in Figure 2.5.

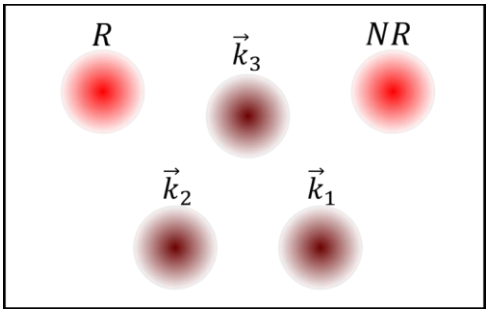

Figure 2.5. Phase matching direction selected in 2DIR setup. R stands for the light from rephasing responses in the direction of $-\vec{k}_1 + \vec{k}_2 + \vec{k}_3$, which is shown in the left, top corner. NR stands for the light from non-rephasing responses in the direction of $+\vec{k}_1 - \vec{k}_2 + \vec{k}_3$, which is shown in the right, top corner. The other light beams are from the input pulses, $\vec{k}_1$, $\vec{k}_2$ and $\vec{k}_3$. $\vec{k}_3$ is positioned close to the center of the figure, while $\vec{k}_1$ and $\vec{k}_2$ are below $\vec{k}_3$. $\vec{k}_1$ is on the left and $\vec{k}_2$ is on the right.

2.6. Lineshape of 2DIR spectra

Previously, the transition frequency ω_{01} was considered as a constant, meaning it is not time-dependent. In a real sample, the potential energy surface of the vibrational transition of the molecule is deformed, so the frequency ω_{01} changes in time. In this section, Kubo's stochastic theory of lineshape is applied to describe the dephasing of coherences.[119, 120] The variation of ω_{01} in time results in pure and inhomogeneous dephasing, which is useful for studying the structure and dynamics in the solution.

For a single molecule during a coherence time, the time evolution of the density matrix can be written as,

$$\dot{\rho}_{01}(t) = -i\omega_{01}(t)\rho_{01}(t)$$

Eq. 56

and should follow the Liouville-von Neumann equation[107, 121, 122],

$$\dot{\rho} = -\frac{i}{h}\left[\hat{H}_0(t), \rho(t)\right]$$

Eq. 57

Integration of Eq. 56 gives the following,

$$\rho_{01}(t) \propto \exp\left(-i\int_0^t \omega_{01}(\tau)d\tau\right)$$

Eq. 58

The average of density matrix over all individual molecules is,

$$\rho_{01}(t) \propto \langle \exp\left(-i\int_0^t \omega_{01}(\tau)d\tau\right)\rangle$$

Eq. 59

where the notation $\langle ... \rangle$ indicates the ensemble average. The instantaneous frequency $\omega(t)$ should change with time due to the variation of environment, which fluctuates around the average frequency ω_{01}. The time-dependent transition frequency of the vibrational state can be represented by,

$$\omega_{01}(t) = \omega_{01} + \delta\omega_{01}(t)$$

Eq. 60

where the first term is the mean frequency and the second term is the frequency fluctuation. The time average of the fluctuation term is 0, meaning $\langle \delta\omega_{01} \rangle = 0$, so Eq. 59 becomes,

$$\rho_{01}(t) \propto e^{-i\omega_{01}t} \langle \exp\left(-i\int_0^t \delta\omega_{01}(\tau)d\tau\right)\rangle$$

Eq. 61

Following this procedure, all response functions can be translated into a new form where ω_{01} is time-dependent. For instance, the linear response function in Eq. 42 becomes,

$$R^{(1)}(t_1) = i\mu_{01}^2 e^{-i\omega_{01}t_1} \langle \exp\left(-i\int_0^{t_1} d\tau\delta\omega_{01}(\tau)\right)\rangle$$

Eq. 62

The ensemble average for all molecules in Eq. 61 is slowly converging due to the oscillatory exponential function, so the expression can be expanded with cumulant expansion truncated after the second order. Thus, the second exponential term in Eq. 61 can be expanded in powers of $\delta\omega_{01}$,

$$\langle \exp\left(-i\int_0^t d\tau\,\delta\omega_{01}(\tau)\right)\rangle = 1 - i\int_0^t d\tau\langle\delta\omega_{01}(\tau)\rangle - \frac{1}{2}\int_0^t\int_0^t d\tau' d\tau''\langle\delta\omega_{01}(\tau')\delta\omega_{01}(\tau'')\rangle + \cdots$$

Eq. 63

In addition, this expression can be written as,

$$\langle \exp\left(-i\int_0^t \delta\omega_{01}(\tau)d\tau\right)\rangle \equiv e^{-g(t)} = 1 - g(t) + \frac{1}{2}g^2(t) + \cdots,$$

Eq. 64

and the $g(t)$ can be expanded in powers of $\delta\omega_{01}$,

$$g(t) = g_1(t) + g_2(t) + \cdots$$

Eq. 65

In the above equation, $g_1(t)$ is on the order of $\delta\omega_{01}$, $g_2(t)$ is on the order of $\delta\omega_{01}^2$, etc. Inserting Eq. 65 into Eq. 64 gives,

$$e^{-g(t)} = 1 - (g_1(t) + g_2(t) + \cdots) + \frac{1}{2}(g_1(t) + g_2(t) + \cdots)^2 + \cdots$$

Eq. 66

The term of $\delta\omega_{01}$ vanishes by construct ($g_1(t) = 0$), because $\langle\delta\omega_{01}\rangle = 0$. Therefore, the dominant term is $g_2(t)$, which is called the lineshape function,

$$g(t) = \frac{1}{2}\int_0^t\int_0^t d\tau' d\tau''\langle\delta\omega_{01}(\tau')\delta\omega_{01}(\tau'')\rangle$$

Eq. 67

Because the lineshape for a molecule is measured at the equilibrium, the absolute time of measurements is not important. Instead, the difference between times of measurements matters, which means the frequency fluctuation function is stationary. Moreover, because the time correlation function is stationary, it should also be even. Thus, the correlation function can be written as,

$$\langle \delta\omega_{01}(\tau')\delta\omega_{01}(\tau'')\rangle = \langle \delta\omega_{01}(\tau'-\tau'')\delta\omega_{01}(0)\rangle = \langle \delta\omega_{01}(\tau''-\tau')\delta\omega_{01}(0)\rangle$$
$$= \langle \delta\omega_{01}(\tau)\delta\omega_{01}(0)\rangle$$

Eq. 68

The function $\langle \delta\omega_{01}(\tau)\delta\omega_{01}(0)\rangle$ is called the frequency-frequency correlation function (FFCF).

Plugging $g(t)$ into Eq. 62, the linear response function becomes,

$$R^{(1)}(t_1) = i\mu_{01}^2 e^{-i\omega_{01}t_1}e^{-g(t)}$$

Eq. 69

and the linear absorption spectrum is obtained,

$$S(\omega) \propto \Re \int_0^\infty e^{i(\omega-\omega_{01})t}e^{-g(t)}dt$$

Eq. 70

The same formalism can be extended to non-linear spectra. In 2.5. Non-linear spectroscopy, the response functions with dephasing can be represented as,

$$R_{1,2}(t_1,t_2,t_3) \propto i\mu_{01}^4 e^{+i\omega_{01}t_1}e^{-t_1/T_2}e^{-i\omega_{01}t_3}e^{-t_3/T_2}$$

$$R_{4,5}(t_1,t_2,t_3) \propto i\mu_{01}^4 e^{-i\omega_{01}t_1}e^{-t_1/T_2}e^{-i\omega_{01}t_3}e^{-t_3/T_2}$$

Eq. 71

In the above equation, the terms of the sort $e^{\pm i\omega_{01}t}e^{-t/T_2}$ can be replaced by $e^{\pm i\omega_{01}t}\langle \exp\left(\pm i\int_0^t d\tau\omega_{01}(\tau)\right)\rangle$, so the third-order response functions of a two-level system are,

$$R_{1,2} = i\mu_{01}^4 e^{-i\omega_{01}(t_3-t_1)} \langle \exp\left(+i\int_0^{t_1}\delta\omega_{01}(\tau)d\tau - i\int_{t_2+t_1}^{t_3+t_2+t_1}\delta\omega_{01}(\tau)d\tau\right)\rangle$$

$$R_{4,5} = i\mu_{01}^4 e^{-i\omega_{01}(t_3+t_1)} \langle \exp\left(-i\int_0^{t_1}\delta\omega_{01}(\tau)d\tau - i\int_{t_2+t_1}^{t_3+t_2+t_1}\delta\omega_{01}(\tau)d\tau\right)\rangle$$

Eq. 72

In addition, when applying the cumulant expansion truncated after second order as shown in Eq. 64 to Eq. 66, the response functions become,

$$R_{1,2} = i\mu_{01}^4 e^{-i\omega_{01}(t_3-t_1)} e^{-g(t_1)+g(t_2)-g(t_3)-g(t_1+t_2)-g(t_2+t_3)+g(t_1+t_2+t_3)}$$

$$R_{4,5} = i\mu_{01}^4 e^{-i\omega_{01}(t_3+t_1)} e^{-g(t_1)-g(t_2)-g(t_3)+g(t_1+t_2)+g(t_2+t_3)-g(t_1+t_2+t_3)}$$

Eq. 73

The non-linear response function can be simplified to the same lineshape function $g(t)$ (Eq. 67) and the same FFCF $\langle\delta\omega_{01}(\tau)\delta\omega_{01}(0)\rangle$ (Eq. 68). FFCF is one important function that can be measured in infrared spectroscopy, and tells us about the dynamics of frequency fluctuations of the molecules. In principle, the FFCF can be measured by linear spectroscopy (Eq. 69 and Eq. 70), but in fact, such measurement is ill-conditioned and not practical due to the presence of experimental noise and double integral. Thus, non-linear spectroscopy is a much better method for determining the FFCF of molecules.

2.7. Spectral diffusion in 2DIR spectra

Several methods have been proposed to extract the frequency-frequency correlation function (FFCF) from 2DIR spectra. The information of FFCF is included in the evolution of the 2DIR peak shape with time, which is called spectral diffusion. Mathematically, the determination of FFCF requires the fitting of experimental 2DIR spectra, which involves constructing a physically motivated model of FFCF, applying the model through corresponding response

functions and the Fourier transform, as well as varying the parameters in FFCF until a good agreement is reached. Instead of above complicated procedure, certain features of the 2DIR spectra can be measured in order to determine the FFCF. For instance, the tilt of the nodal line between the 0-1 peak and 1-2 peak can be a good representation of FFCF, when the anharmonicity is larger than the linewidth of the transition.[107]

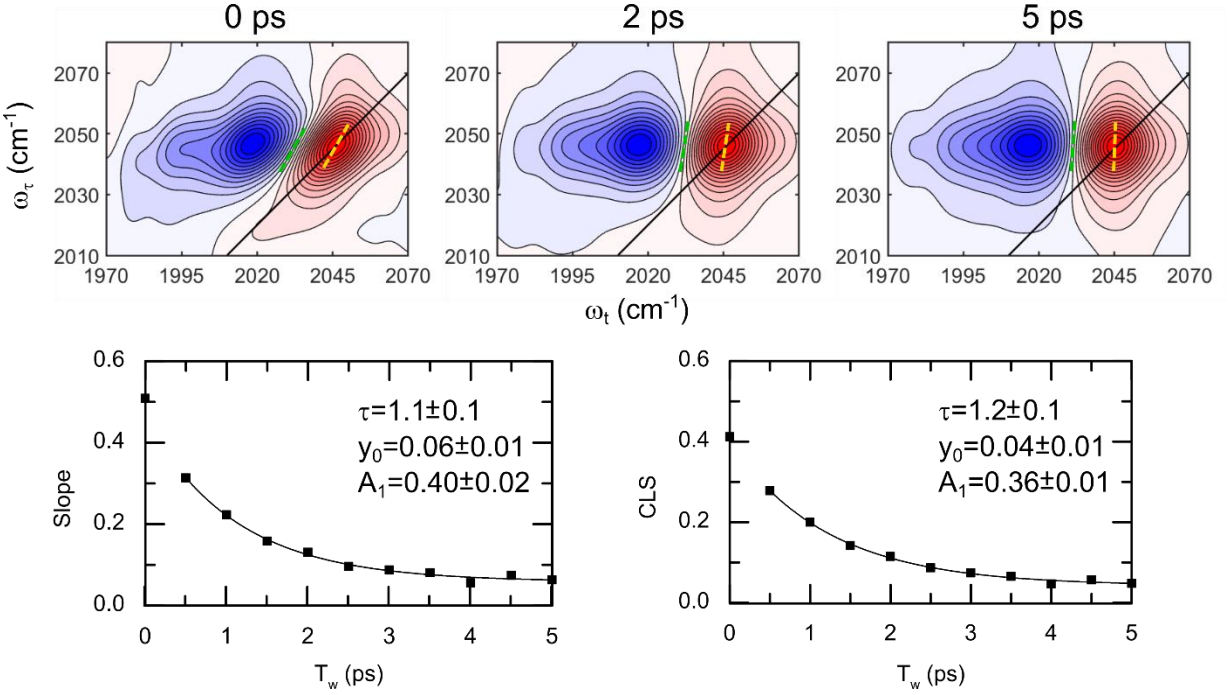

Figure 2.6. An example of extracting FFCF dynamics in D_2O solution of 50 mM sodium azide (NaN_3). 2DIR spectra of azide stretch at waiting time of 0, 2 and 5 ps are shown in the top panel. X- and y-axis are probe and pump frequencies, respectively. Green and yellow dashed lines represent the nodal line and center line of 0-1 peak, respectively. The slope of the nodal line (slope, bottom left) and center line slope (CLS, bottom right) were used to extract FFCF dynamics of azide stretch. The slopes were fitted by a single exponential decay with an offset, while the fitting parameters are listed in the plots. Both methods give the dynamics of ~1.1 ps.

If the anharmonicity is smaller than or equal to the transition, the two peaks overlap and cancel in part, making the tilt of the nodal line a measurement of anharmonicity.[123] In the case of a very inhomogeneous transition, the tilt of the nodal line is 45° at early time $t = t_0$, which rotates towards 90° at late time $t = t_0 + \tau$. Since the tilt of a line can be represented by the slope

of the line, the qualitative measurement of FFCF can be achieved by plotting the slope of nodal line with time t. An example of extracting the nodal line is shown in Figure 2.6. To obtain the FFCF dynamics of the azide stretch, the plot of slope vs. time is fitted by single exponential decay because the FFCF has a form of,

$$\langle \delta\omega_{01}(t)\delta\omega_{01}(0)\rangle = \Delta\omega_1^2 e^{-t/\tau_1} + \Delta\omega_2^2 e^{-t/\tau_2} \approx \Delta\omega_1^2 e^{-t/\tau_1} + y_0$$

Eq. 74

where $\Delta\omega_1$ and $\Delta\omega_2$ are the frequency fluctuation amplitudes, τ_1 and τ_2 are the FFCF dynamics, and y_0 is the offset. When the τ_2 is much longer than the investigated time window, the second term of the exponential decay is approximated to be a constant, which is the offset y_0. The first point at 0 ps is excluded in the fitting due to the presence of the non-resonant signal.

Another method of describing spectral diffusion in 2DIR spectra is the center line slope (CLS).[124] At a given pump frequency ω_τ, a slice through the 2DIR spectrum parallel to the probe frequency ω_t is a spectrum when the slice is projected onto the ω_t axis. The maximum of this spectrum around the measured transition is one point on the center line. Searching for all maxima of the spectra at each ω_τ reveals a set of points. The line connecting the points is the center line.

Similar to the nodal line, the center line is tilted along the diagonal line at early time $t = t_0$, while it gets more upright at late time $t = t_0 + \tau$. So the slope of the center line is a good indication of spectral diffusion, where FFCF can be retrieved by plotting the CLS vs. the waiting time. The example of CLS for the azide stretch in 50 mM D_2O/NaN_3 solution is shown in Figure 2.6. The CLS was fitted with a single exponential decay as shown in Eq. 74. The resulted parameters are listed in the corresponding plot of Figure 2.6. Comparing the fitting results of CLS with nodal line slope, though there are small differences for y_0 and A_1 between two

methods, the FFCF dynamics τ is statistically the same, which proves that both methods capture the same information from the 2DIR spectra. Some other methods for retrieving FFCF from 2DIR spectra are discussed in the reference.[123]

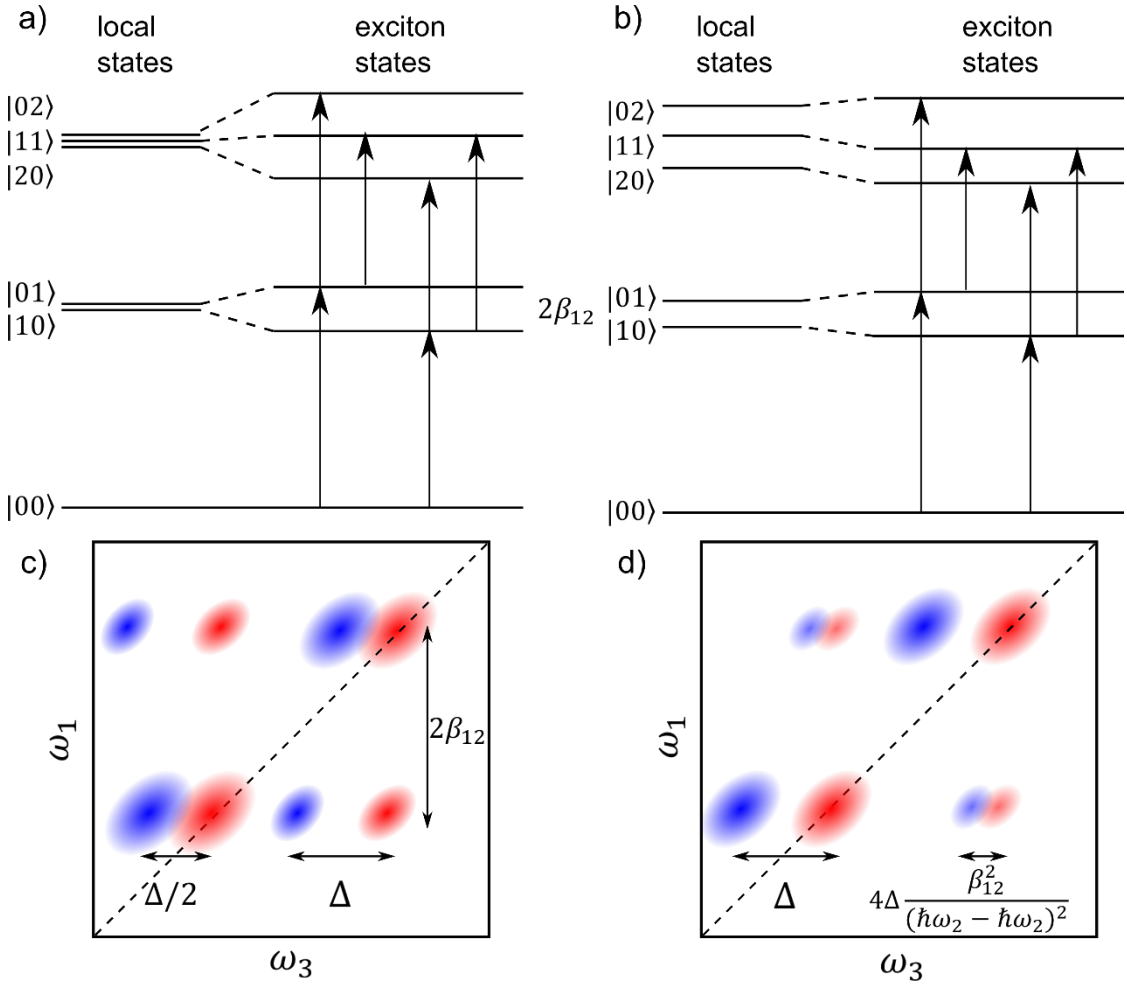

Figure 2.7. Level schemes of two coupled oscillators in two extremes: a) strong coupling regime $|\beta_{12}| \gg |\hbar\omega_2 - \hbar\omega_1|$, and b) weak coupling regime $|\beta_{12}| \ll |\hbar\omega_2 - \hbar\omega_1|$. The schemes of 2DIR spectra c) and d) are shown below the corresponding level schemes a) and b), respectively. The red (high frequency peak) and blue (low frequency peak) represent the 0-1 and 1-2 transitions, respectively. The dash lines are the diagonal lines of y=x. X- and y-axes are pump and probe frequencies, respectively. In strong coupling regime, two cross peaks from the 0-1 and 1-2 transitions are far away in frequency as compared to the diagonal peaks. In weak coupling regime, they are very close in frequency as compared to the diagonal peaks.

2.8. Cross peaks in 2DIR spectra

Another important feature of 2DIR spectra is the cross peak. As shown in Figure 2.7, the low-intensity peaks at the intersection of the two pairs of main peaks are called the cross peaks. Usually, the appearance of cross peaks can result from either vibrational coupling/excitons[66, 77] or chemical exchange.[101, 125]

2.8.1. Vibrational coupling

For a system of coupled local modes, the exciton Hamiltonian should be,

$$H = \hbar\omega_1\left(b_1^\dagger b_1 + \frac{1}{2}\right) + \hbar\omega_2\left(b_2^\dagger b_2 + \frac{1}{2}\right) + \beta_{12}\left(b_1^\dagger b_2 + b_2^\dagger b_1\right)$$

Eq. 75

where the $b_n^\dagger$ and b_n are the creation and annihilation operators of the local oscillators, respectively. The Hamiltonian of Eq. 75 can be expanded on a site basis $\{|ij\rangle\}$ where i and j refer to the quantum number in the two modes. In this example, only two coordinates are considered for clarification. Neglecting the zero-point energies, Eq. 75 can be written as,

$$H = \hbar\omega_1 b_1^\dagger b_1 + \hbar\omega_2 b_2^\dagger b_2 + \beta_{12}\left(b_1^\dagger b_2 + b_2^\dagger b_1\right)$$

Eq. 76

The coupling is included in the terms $b_1^\dagger b_2 + b_2^\dagger b_1$, which describes a hopping of the excitation from one site to the other. For example, $b_1^\dagger b_2|01\rangle = |10\rangle$, where the $|ij\rangle$ is in a local mode basis. The two-mode site basis is used to describe the third-order non-linear spectroscopy up to double excitations, e.g. $\{|ij\rangle\} = |00\rangle, |10\rangle, |01\rangle, |20\rangle, |02\rangle, |11\rangle$, because the pulses in the third-order non-linear spectroscopy do not probe higher eigenstates. The expanded Hamiltonian can be represented by,

$$H = \begin{pmatrix} 0 & & & & & \\ & \hbar\omega_1 & \beta_{12} & & & \\ & \beta_{12} & \hbar\omega_2 & & & \\ & & & 2\hbar\omega_1 & 0 & \sqrt{2}\beta_{12} \\ & & & 0 & 2\hbar\omega_1 & \sqrt{2}\beta_{12} \\ & & & \sqrt{2}\beta_{12} & \sqrt{2}\beta_{12} & \hbar\omega_1 + \hbar\omega_2 \end{pmatrix}$$

Eq. 77

The Hamiltonian has only the quantum conserving terms, so it can be divided into three blocks: the ground state, the one-exciton Hamiltonian, and the two-exciton Hamiltonian. Although the Hamiltonian includes the coupling terms between two local modes, it is still harmonic and thus cannot be detected by 2DIR spectroscopy.[107] For a potential energy surface to create a 2DIR spectrum, the terms of higher than second order need to be included in the Hamiltonian, especially the ones that allow us to describe the local modes as anharmonic potentials and are quantum-conserving. Under these conditions, the Hamiltonian becomes,

$$H = \hbar\omega_1 b_1^\dagger b_1 + \hbar\omega_2 b_2^\dagger b_2 + \beta_{12}\left(b_1^\dagger b_2 + b_2^\dagger b_1\right) - \frac{\Delta}{2} b_1^\dagger b_1^\dagger b_1 b_1 - \frac{\Delta}{2} b_2^\dagger b_2^\dagger b_2 b_2$$

Eq. 78

where the terms $-b_n^\dagger b_n^\dagger b_n b_n$ decrease the site energies of the doubly excited local modes by an energy Δ, which is the local mode anharmonic shift. Expanding the Hamiltonian of Eq. 78 on the same basis as previously discussed, a new Hamiltonian is expressed as,

$$H = \begin{pmatrix} 0 & & & & & \\ & \hbar\omega_1 & \beta_{12} & & & \\ & \beta_{12} & \hbar\omega_2 & & & \\ & & & 2\hbar\omega_1 - \Delta & 0 & \sqrt{2}\beta_{12} \\ & & & 0 & 2\hbar\omega_1 - \Delta & \sqrt{2}\beta_{12} \\ & & & \sqrt{2}\beta_{12} & \sqrt{2}\beta_{12} & \hbar\omega_1 + \hbar\omega_2 \end{pmatrix}$$

Eq. 79

In this representation, the ground state and one-exciton Hamiltonians are still the same, but the two-exciton Hamiltonian is different because of the anharmonicity of the local modes. Therefore, assume the frequencies of two local modes are similar ($\omega_1 \approx \omega_2 \equiv \omega$), the Hamiltonian after diagonalization becomes,

$$H = \begin{pmatrix} 0 & & & & & \\ & \hbar\omega - \beta & & & & \\ & & \hbar\omega - \beta & & & \\ & & & 2\hbar\omega - \frac{1}{2}\Delta - \frac{1}{2}\sqrt{\Delta^2 + 16\beta^2} & & \\ & & & & 2\hbar\omega - \frac{1}{2}\Delta + \frac{1}{2}\sqrt{\Delta^2 + 16\beta^2} & \\ & & & & & 2\hbar\omega - \Delta \end{pmatrix}$$

Eq. 80

In this case, the local mode anharmonicity mixes into all double-excited states, which creates diagonal and off-diagonal anharmonic shifts that can be measured by 2DIR spectroscopy.

Now that the exciton Hamiltonian is introduced, the spectroscopy of the excitons can be studied. The vibrational coupling or the excitonic nature of the transitions provides valuable information about the 3D structure of the molecular system. In the model of two coupled transition dipoles, the coupling between the pair of dipoles can be written as,

$$\beta_{ij} = \frac{1}{4\pi\epsilon_0}\left[\frac{\vec{\mu}_i \cdot \vec{\mu}_j}{r_{ij}^3} - 3\frac{(\vec{r}_{ij} \cdot \vec{\mu}_i)(\vec{r}_{ij} \cdot \vec{\mu}_j)}{r_{ij}^5}\right]$$

Eq. 81

where $\vec{\mu}_i$, $\vec{\mu}_j$ are the transition dipoles of the local modes and $\vec{r}_{ij}$ is the vector connecting the sites i and j.

For the linear spectrum of a coupled dimer, the one-exciton Hamiltonian is considered, which is:

$$H_1 = \begin{pmatrix} \hbar\omega_1 & \beta_{12} \\ \beta_{12} & \hbar\omega_2 \end{pmatrix}.$$

Eq. 82

The eigenvalues of above Hamiltonian are:

$$E_{1,2}^{(ex)} = \frac{\hbar\omega_1 + \hbar\omega_2 \mp \sqrt{4\beta_{12}^2 + (\hbar\omega_2 - \hbar\omega_1)^2}}{2}$$

Eq. 83

The eigenstates of above Hamiltonian are:

$$|\Phi_1\rangle = +\cos\alpha|10\rangle - \sin\alpha|01\rangle$$

$$|\Phi_2\rangle = +\sin\alpha|10\rangle + \cos\alpha|01\rangle$$

Eq. 84

for the eigenvalues of $E_1^{(ex)}$ and $E_2^{(ex)}$, respectively, with a mixing angle of $\tan 2\alpha = 2\frac{\beta_{12}}{\hbar\omega_2 - \hbar\omega_1}$.

The transition dipole moments can be derived in the same way,

$$\vec{\mu}_1^{(ex)} = +\cos\alpha \cdot \vec{\mu}_1 - \sin\alpha \cdot \vec{\mu}_2$$

$$\vec{\mu}_2^{(ex)} = +\sin\alpha \cdot \vec{\mu}_1 + \cos\alpha \cdot \vec{\mu}_2$$

Eq. 85

Thus, the intensities of the two observed transitions, which are $\left|\vec{\mu}_1^{(ex)}\right|^2$ and $\left|\vec{\mu}_2^{(ex)}\right|^2$, are dependent on the relative orientation of the two coupled transition dipoles, the coupling strength β_{12} and frequency separation $(\hbar\omega_2 - \hbar\omega_1)$. In principle, linear spectra can provide structural information for different geometries of molecules. However, the linear spectra of the molecules can be so convoluted that the peaks from different structures are not distinguishable.

2DIR spectroscopy can make the distinction between different structures by mixing the local mode anharmonicity Δ into the two-exciton states as shown in Eq. 80. In the strong

coupling limit where $|\beta_{12}| \gg |\hbar\omega_2 - \hbar\omega_1|$, the cross peaks in 2DIR spectra have a larger separation than the diagonal peaks since the excitons are delocalized over the two local modes. In the weak coupling limit with $|\beta_{12}| \ll |\hbar\omega_2 - \hbar\omega_1|$, the excitations are localized so the resulting 2DIR spectrum looks similar to the uncoupled spectrum. In this limit, the diagonal anharmonicities are $\Delta_{11} \approx \Delta_{22} \approx -\Delta$, so the off-diagonal anharmonicities can be calculated[126],

$$\Delta_{12} = -4\Delta \frac{\beta_{12}^2}{(\hbar\omega_2 - \hbar\omega_1)^2}$$

Eq. 86

In the weak coupling limit, the splitting of the cross peaks is proportional to the squared strength of the coupling constant. Since the splitting is usually smaller than the spectral widths, the two cross peaks from 0-1 and 1-2 transitions overlap partially and cancel. Therefore, instead of one pair of cross peaks, only one peak with low intensity can be observed. In addition, the diagonal peak intensity in 2DIR spectra is proportional to $|\vec{\mu}|^4$ while the peak intensity in linear spectra is only proportional to $|\vec{\mu}|^2$, so the strong peak becomes even more prominent in 2DIR spectra. Since the cross peak intensity is proportional to $|\vec{\mu}_1|^2|\vec{\mu}_2|^2$, the cross peak will disappear when the diagonal peak disappears. During the measurement of non-linear spectra, the Hamiltonian of a coupled dimer changes at different population times (t_2, Figure 2.3), which leads to energy transfer between eigenstates that can change the intensity of cross peaks or even create new peaks. In fact, the intensity of cross peak grows with increasing t_2 and will decrease at very long time after a plateau. The lineshape of the peaks also changes due to the fluctuations of the solvent and molecular structure. Thus, the evolution of cross peaks in time can provide dynamical information about the structure and environment of molecules, e.g. population relaxation, population transfer and coherence transfer.

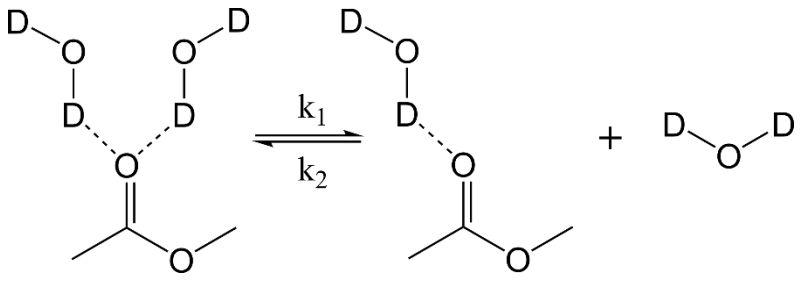

Figure 2.8. Scheme of hydrogen bond making and breaking of methyl acetate in deuterated water (D_2O). On the left side of the equilibrium, two D_2O molecules form hydrogen bonds with the oxygen atom of the methyl acetate. On the right side of the equilibrium, one hydrogen bond breaks between the methyl acetate and one D_2O molecule, leaving only one hydrogen bond between methyl acetate and the other D_2O molecule.

2.8.2. Chemical exchange

The other process that causes time-dependent cross peaks is chemical exchange. For example, the FTIR spectrum of methyl acetate in D_2O has one broad band with two sub-bands in the carbonyl stretch region.[127] The sub-band at low frequency side corresponds to the carbonyl group forming two hydrogen bonds with deuterated water, while the sub-band at high frequency side corresponds to the carbonyl group forming one hydrogen bond with the deuterated water. The band of hydrogen-bonded carbonyl stretch is red-shifted from the free carbonyl stretch because the hydrogen bonding strongly deforms the potential energy curve of the carbonyl stretch. Multiple peaks of the same vibrational mode can occur when this mode is positioned in multiple environments, or in other words, has different potential surfaces. Since the hydrogen bonds are usually weak, they can constantly form and break on a femtosecond to picosecond time scale as shown in Figure 2.8, which creates a kinetic/chemical exchange between the two states of the transition. The exchange between different transition states like this can be probed by 2DIR spectroscopy via the appearance of cross peaks.[128] At waiting time zero, the two states of carbonyl stretch are observed as the diagonal peaks, while the cross peaks are absent because the making and breaking of hydrogen bonds happen on a longer time scale and the coupling

between two states is negligible. As waiting time increases, the two states exchange, which creates the cross peaks on the off-diagonal line. As a result, the dynamics of the cross peak is a direct observation of the exchange dynamics of the two states.

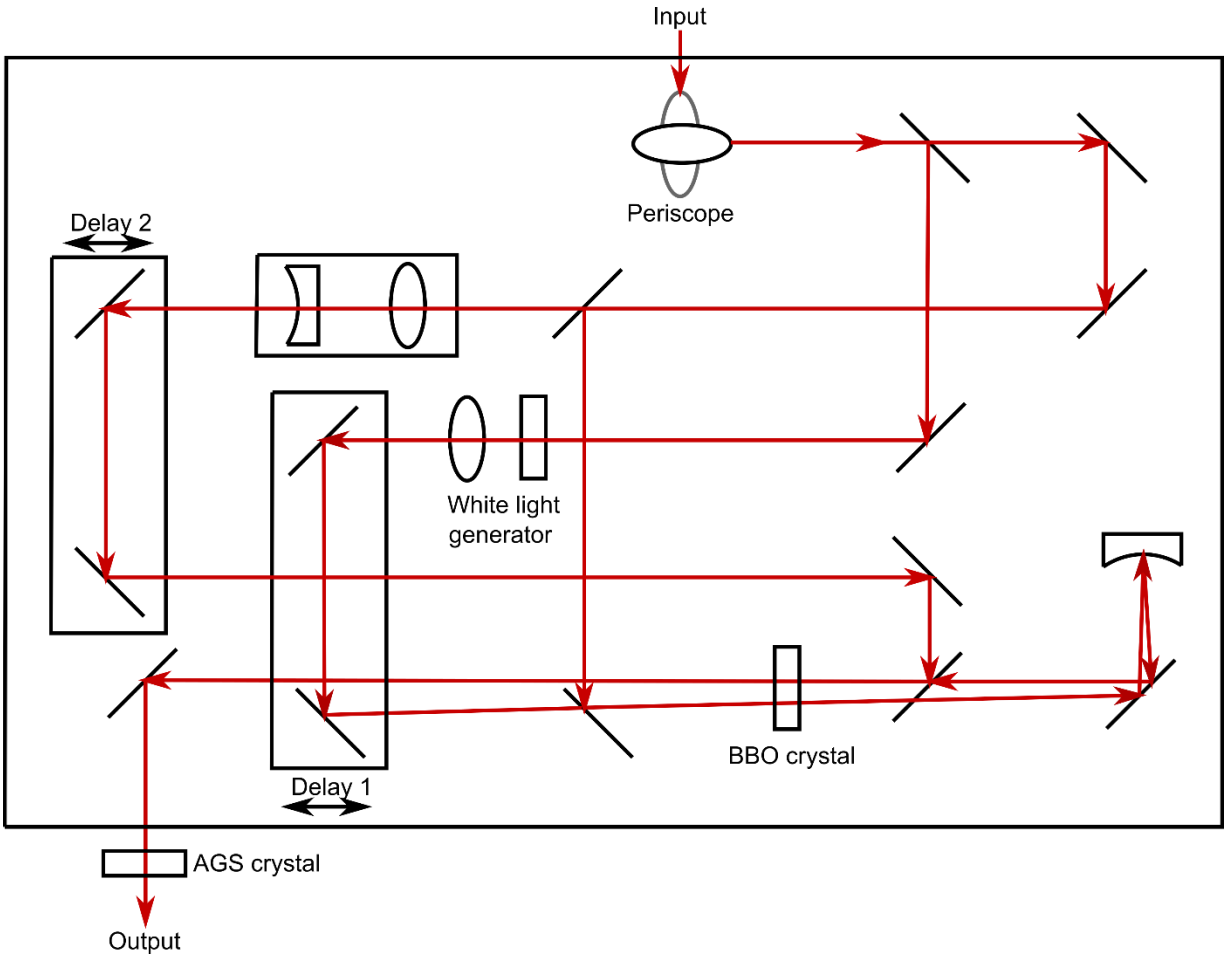

Figure 2.9. Simplified schematic layout of the optical parametric amplifier used for generating infrared pulses. Details of the layout are illustrated in the text.

2.9. 2DIR experimental setup

2.9.1. Laser pulse generation

The Mai-Tai SP with Spitfire Ace High-performance Ti:sapphire system is used to generate an ultrafast laser pulse. Ultrafast pulses are produced with passive mode locking technique, where the continuum wave light is focused into a Ti:sapphire crystal, and shortened in

the cavity exploiting non-linear optical Kerr-Lens effect.[129] The other cavity components are an end mirror, an output coupler, and a prism pair in order to compensate for the dispersion of Ti:sapphire crystal. The resulting pulse is centered at ~800 nm with low peak power, which serves as the seed pulse to be amplified. To avoid serious damage to the amplification cavity, chirped pulse amplification technique was utilized.[130] In this case, the ultrafast laser pulse is first stretched out temporally, then amplified, and finally compressed again. After the compressor, a laser pulse centered at ~800 nm with 5 kHz repetition rate, a temporal width of ~60fs, and an average power of 5.0 W is safely generated.

An optical parametric amplifier (OPA) is used for generating pulses in the mid-infrared region with the amplified ~800 nm pulse as input. The simplified schematic layout of the OPA is shown in Figure 2.9. The input pulse is split into three beams, two of which serve as the pump pulses with the last one working as the white light seed. The white light seed is focused on a 2 mm thick sapphire plate in order to generate the white light. The resulting white light and the pump pulses are focused on a β-BaB_2O_4 crystal (BBO, type II, 2 mm thickness) to generate the signal and idler beams in two steps. First, the white light and one of the pump pulses (~50 μJ) are combined on the BBO crystal in order to preamplify the desired frequency component of the output beam. Second, the preamplified beam is overlapped with the other pump pulse (~ 270 μJ) on the same BBO crystal at a different spot in order to amplify the power of signal beam. After the power amplifier, signal and idler beams are separated from the pump using dichroic mirrors. The mid-infrared pulse is later generated by difference frequency generation (DFG) between signal and idler beams focused on a $AgGaS_2$ crystal (AGS, type II, 1 mm thickness). The pulses other than the desired infrared pulse will be filtered by a germanium filter so that only the infrared pulse can be transmitted.

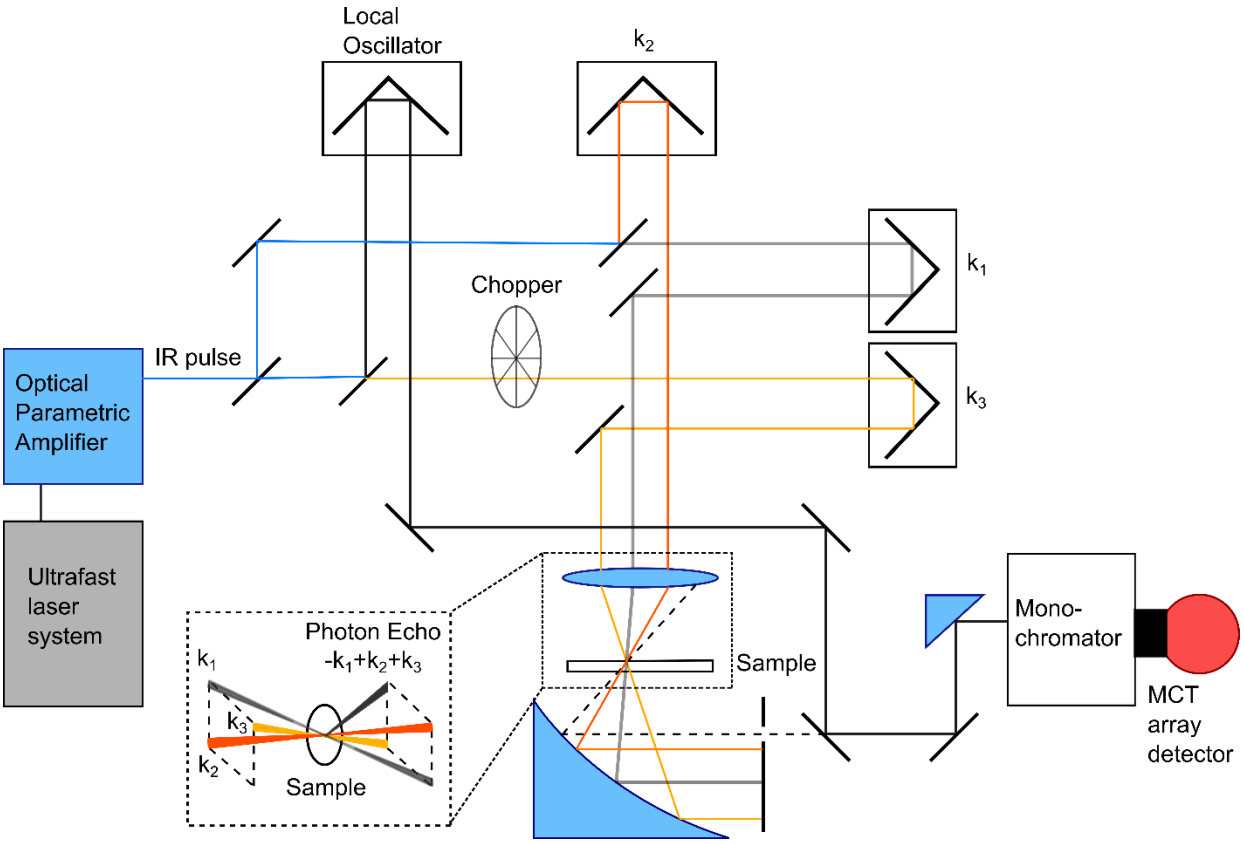

Figure 2.10. Simplified schematic layout for 2DIR spectroscopy setup. Details of the layout are illustrated in the text.

2.9.2. 2DIR spectroscopy

Several ways of experimental setup design have been proposed for collecting heterodyned photon echo signals generated by three incident pulses. In our lab, the most commonly used geometry of 2DIR setup is employed, which is called the box-CARS phase-matching geometry.[131] The simplified schematic layout of the 2DIR setup is shown in Figure 2.10. The incident beam is split into four pulses: the local oscillator (LO), $\vec{k}_1$, $\vec{k}_2$ and $\vec{k}_3$. The path of each pulse can be modified with a computer-controlled translation stage that moves at a nanometer scale. With the precise motion of the stage, the time interval between pulses can be modified with attosecond time resolution. A synchronized chopper at the frequency of 2.5 kHz is

positioned on the path of $\vec{k}_3$ to allow for the subtraction of the local oscillator intensity. The three pulses $\vec{k}_1$, $\vec{k}_2$ and $\vec{k}_3$ are focused on the sample to generate the photon echo signal. The liquid sample is held in a mounted O-ring-sealed sample cell with two CaF_2 windows separated by a Teflon spacer. The emitted photon echo is overlapped and heterodyned with the LO on a CaF_2 beamsplitter. The interfered signal is then detected by a liquid nitrogen-cooled 64-element MCT array detector through a monochromator. The experimental setup is enclosed in an air-tight hand-made box, which is purged with CO_2 and H_2O filtered air to avoid contact with CO_2 and water. The coherent time τ and the center wavelength λ are varied in the experiment to collect absorptive 2DIR spectra for the vibrational modes of interest at different waiting times.

After the raw data are collected in the form of time τ and wavelength λ, they are first inverse Fourier transformed from $S(\tau, T, \lambda_k)$ to $S(\tau, T, t)$, followed by another Fourier transform from $S(\tau, T, t)$ to $S(\omega_\tau, T, \omega_t)$, where T is the waiting time between $\vec{k}_2$ and $\vec{k}_3$, λ_k is the wavelength of the kth detector element, t is the coherent time between $\vec{k}_3$ and LO, and ω_τ/ω_t is the evenly spaced pump/probe frequency. The inverse Fourier transform is performed as:

$$S(\tau, T, t) = \sum_{k=1}^{64} \tilde{S}(\tau, T, \lambda_k) e^{-i\omega_k t} \Delta\omega_k$$

Eq. 87

where $\omega_k = \frac{2\pi c}{\lambda_k}$ and $\Delta\omega_k = \frac{2\pi c}{\lambda_k - \frac{1}{2}\Delta\lambda} - \frac{2\pi c}{\lambda_k + \frac{1}{2}\Delta\lambda}$. $\Delta\lambda$ is the wavelength difference between two neighboring elements of the detector. The final coherent time t is obtained by moving the time delay for LO and examining the interference between LO and photon echo. Notice that the LO always precedes the photon echo by 0.5 to 1 ps for full data acquisition. Then the double Fourier transform of the signal is performed as:

$$\tilde{S}(\tau, T, \omega_t) = \sum_t S(\tau, T, t) e^{i\omega_t t} \Delta t$$

$$\tilde{S}(\omega_\tau, T, \omega_t) = \sum_t S(\tau, T, \omega_t) e^{i\omega_\tau t} \Delta \tau$$

Eq. 88

Both rephasing and nonrephasing data are processed in the same method following the procedure discussed above. The final frequency domain data are corrected by putting a relative phase between the rephasing and nonrephasing signals.

CHAPTER 3. STRUCTURE AND DYNAMICS OF THE LITHIUM ION SOLVATION SHELL IN UREAS

Lithium ion batteries have become ubiquitous to modern life due to its use in the energy storage needs of our daily lives. In past several decades, much effort has been put into studying the molecular structure of electrolytes composed of organic carbonates. However, other solvents with similar properties but better thermal stabilities, such as tertiary amides, have not received the same level of scrutiny. In this work, solutions of lithium salts in ureas, tertiary amides with structure RR'N-CO-NR''R''', with different sizes and connectivity are studied. Ureas present an interesting case study because unlike organic carbonates the amide bond is planar and has restricted conformational change. In addition, ureas cannot bind the lithium ion through their nitrogen atoms. By using steady-state and time-resolved infrared spectroscopies and ab-initio computational methods, detailed descriptions of the changes to the lithium ion solvation structure as a result of the urea structure were derived for three ureas bearing a strong resemblance to commonly used organic carbonates. These results show that the solvation shell of ureas has a tetrahedral structure similar to other organic solvents. Although the structure of the amide bonds in these ureas is similar to that of carbonate molecules, the atomic connectivity differs. In addition, the dynamics of the cation solvation shell formed by ureas shows a picosecond motion, which is attributed to deformation of the tetrahedral structure. Our investigations also indicate that the deformation dynamics is controlled directly by the size of the urea due to the rigidity of the amide bond in these molecules. Overall, this work shows that ureas share similarity with their organic carbonate analogues, but the rigid urea structure provides an easier framework for interpreting the vibrational observations in terms of the solvent molecular structure.

This chapter was previously published as Chen, X.; Fulfer, K. D.; Woodard, K. T.; Kuroda, D. G., "Structure and dynamics of the litium ion solvation shell in ureas," *The Journal of Physical Chemistry B*, 2019, 123 (46), 9889-9898, copyright 2019 American Chemical Society.

3.1. Introduction

As energy demands continue to expand, finding safe and efficient means of storing energy is becoming a high priority.[6] Lithium ion batteries currently serve most portable energy storage needs, albeit with a few significant safety and efficiency issues.[132] While these issues are relatively manageable for the portable energy storage industry, the safety and efficiency concerns of lithium ion technology limit its ability to be used for larger scale energy storage.[133-136] One significant contributor to these safety issues, is the high flammability and low flash points of the solvents used in the current electrolytes.[137]

A common metric used to determine good solvents for an electrolyte is the dielectric constant and viscosity.[5, 138-140] The organic carbonates, especially those of cyclic structure, have particularly high dielectric constants, with ethylene carbonate having a dielectric constant of 90.0 and dimethyl carbonate having a dielectric constant of 3.2 at 25°C, hence the widespread use of carbonate solvents in lithium ion battery electrolytes.[6] While other alternatives to organic carbonates have been presented in the literatures, these alternatives have some drawbacks such as: high viscosity, low dielectric constant, low boiling point, etc. However, ureas are an alternative which has not been fully investigated in the literature. Notably, replacing the ethereal oxygen of the carbonates with a nitrogen atom does not result in large loss of dielectric constant since 1,3-dimethyl-2-imidazolidinone (DMI) and tetramethylurea (TMU) have dielectric constants of 37.6 and 23.5 respectively, at 25°C.[141, 142] From a safety perspective, ureas have a significant larger flash point, which makes them less susceptible to problem associated with thermal runoff.[143] In comparison, DMI has a flash point of ~120 °C and TMU has a flash point of ~75 °C, while the typical commercially used lithium ion battery electrolyte has a flash point of

~28 °C.[137, 141, 144] Thus, the favorable flash points, dielectric constants and similar structures to carbonates, give a promising prospectus for urea-based electrolytes.

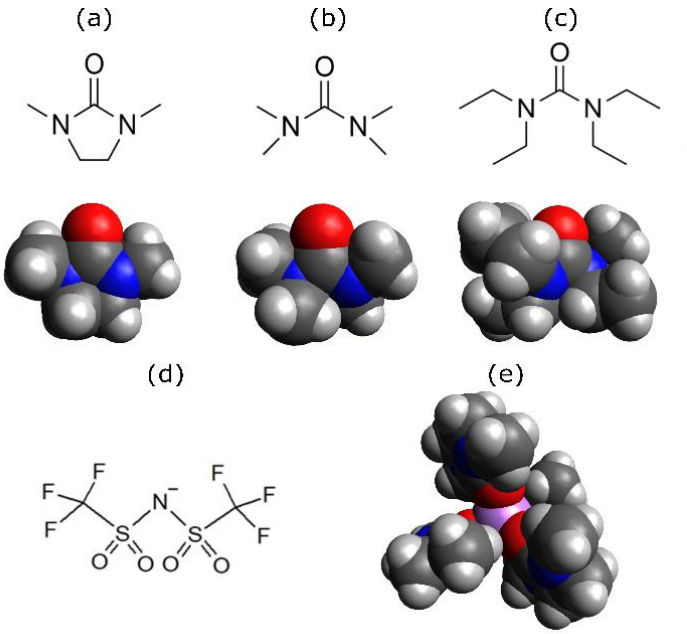

Scheme 3.1. Structure and space-filled model of ureas: (a) 1,3-dimethyl-2-imidazolidinone (DMI), (b) tetramethylurea (TMU), (c) tetraethylurea (TEU), (d) bis(trifluromethanesulfonyl)imide (TFSI-) anion, and (e) lithium ion solvated with four urea molecules (DMI).

From a molecular perspective, ureas have the additional methyl groups crowding the oxygen and potentially making it less available to bind with lithium ion (Li^+) than the carbonyl oxygen of carbonates, as seen in the structure and space-filled model of some ureas (Scheme 3.1).[77] Furthermore, the groups directly bonded to the ethereal oxygen in organic carbonates (Scheme 3.1) have the ability to rotate with very low energy barriers.[145] The isomerization is avoided in the case of ureas due to the double bond character of the amide C-N bond,[146-148] which not only inhibits the conformational rotation of the group, but also makes the ureas much more rigid than its analogue carbonate. Finally, ureas do not have the possibility of binding Li^+ through their nitrogen atoms because they are doubly substituted (Scheme 3.1). Thus, the change

in structure of the solvent from carbonates to ureas is expected to have structural, and potentially dynamical effects on the lithium ion (Li^+) solvation shell, which are known to play a significant role in the properties of the electrolyte.[149]

In this work, a combination of infrared spectroscopic techniques and computational methods was used to characterize the structure and dynamics of the Li^+ solvation complexes in ureas. Specifically, Li^+ solutions formed by mixing lithium bis(trifluromethanesulfonyl)imide (LiTFSI) and a urea (DMI, TMU or TEU, Scheme 3.1) were studied with linear (FTIR) and two-dimensional infrared (2DIR) spectroscopies, and DFT calculations. In particular, two-dimensional infrared spectroscopy (2DIR) has been previously shown to be an excellent tool for characterizing the structure and dynamics of solvation complexes with strongly coupled vibrational modes.[72, 74, 77, 83] Compared to linear infrared spectroscopy (FTIR), 2DIR has advantages with regard to structure determination and dynamics investigation, including enhanced spectral resolution and the ability to sense vibrational coupling.[150-155]

3.2. Methods

3.2.1. Solution preparation

LiTFSI 98% pure from Acros Organics, DMI 98% pure from Alfa Aesar, TMU 99% pure from Alfa Aesar, and TEU 99% pure from TGI were dried with molecular sieves for two days prior to use. LiTFSI was dried in a vacuum oven overnight at 150 °C. Note that LiTFSI was selected due to its higher solubility in the ureas. The prepared samples were tested for less than 200 ppm of water after preparation. Urea-Li^+ solutions were prepared at different concentrations with molar fractions of Li^+, $X(Li^+)$, equal to 0, 0.025, 0.05, 0.075 and 0.1. In this case, $X(Li^+)$ is defined as the moles of Li^+ over the total moles of Li^+ and solvent. Sample cells for FTIR were

comprised of the Li^+-urea solution sandwiched between two CaF_2 windows without spacer. For 2DIR experiments, sample cells consisted of a CaF_2 window and a CaF_2 convex lens with 1 m focal length.[74, 77, 83] All solutions and sample cells were prepared inside a N_2-filled glovebox in order to minimize water contamination.

3.2.2. Fourier transform infrared spectroscopy (FTIR)

FTIR experiments were performed on a Bruker Tensor 27 equipped with a liquid nitrogen cooled MCT detector with a spectral resolution of 0.5 cm^{-1}. Reported spectra were averaged over 40 scans. FTIR data were modeled using OriginLab software.

3.2.3. Pump probe spectroscopy

The frequency selective pump-probe experiments were performed using the same experimental setup as previously published.[84] In this case, the pump-probe signal was collected from -0.4 ps to 5 ps in 0.1 ps intervals for the first 1.6 ps, and followed by 0.4 ps intervals due to the short vibrational lifetime of the ureas. The anisotropy of each sample was computed from the different polarized selective pump probe experiments as: $r(t) = [I_{\parallel}(t) - I_{\perp}(t)]/[I_{\parallel}(t) + 2I_{\perp}(t)]$, where $I_{\parallel}$(t) and $I_{\perp}$(t) are the pump-probe signals measured for parallel and perpendicular polarization between the pump and probe, respectively.

3.2.4. Vibrational photon echo infrared spectroscopy (2DIR)

The experimental setup used for 2DIR photon echo experiments has been described previously,[114, 150] and thus, is only briefly described here. A Spectra Physics Spitfire Ace Ti:sapphire amplifier with a 5 kHz repetition rate followed by an OPA-800C was used to generate broadband infrared pulses with a temporal width of ~60 fs. Each infrared pulse was split into four identical pulses, three of which were focused onto the sample in a boxcar

configuration.[107] The time intervals between the infrared pulses were adjusted using four computer-controlled delay stages and were denoted as follows: τ (between pulses 1 and 2), T_w (between pulses 2 and 3, the latter of which produces the photon echo), and t (between the generated photon echo and pulse 3). Photon echo produced with all parallel polarization pulses (XXXX) in the $-\mathbf{k}_1+\mathbf{k}_2+\mathbf{k}_3$ phase-matching direction was heterodyned with the local oscillator, dispersed with a Triax monochromator (100 grooves/mm), and detected on a liquid nitrogen cooled 64 element MCT array. To obtain the 2DIR spectrum, the photon echo signal was transformed from $S(\tau, T_w, t)$ to $S(\omega_\tau, T_w, \omega_t)$ with a double Fourier transform along τ and t, while keeping the waiting time (T_w) as a parameter. Data were collected for waiting times, T_w, of 0 to 5 ps in 0.5 ps steps. For each T_w time, the first time interval, τ, was scanned from -4 ps to +4 ps in 5 fs steps in order to collect both the rephasing and non-rephasing data. The local oscillator was set to precede the photon echo signal by ~0.5 ps. It should be noted that the $T_w = 0$ data point was excluded from some of the data analysis due to possible distortions arising from the presence of non-resonant signals.[156]

3.2.5. Density functional theory calculations (DFT)

Density functional theory calculations were performed with Gaussian 16 software at PBE1PBE level of theory using the 6-311++G** basis set.[157] Initial molecules and solvation shells were built in the Avogadro software where the structures were first minimized using a classical force field (MMFF94). Geometry optimizations, frequency calculations and Natural Bond Orbital (NBO) analysis were performed in the gas phase.

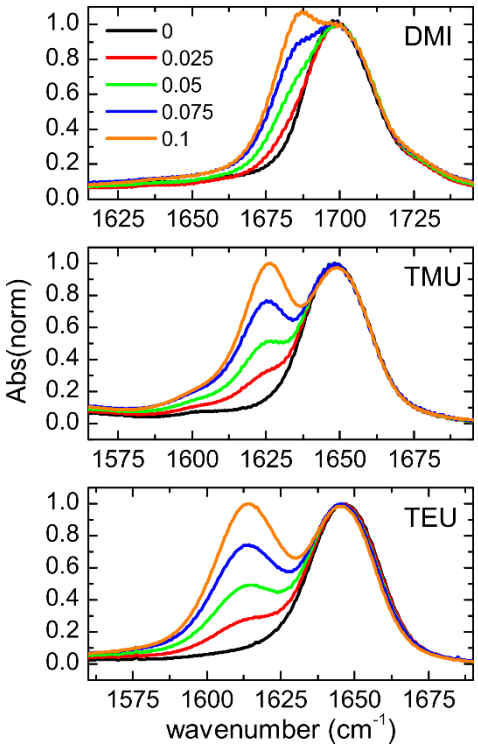

Figure 3.1. Concentration-dependent FTIR spectra for LiTFSI in DMI, TMU and TEU for the following concentrations: 0 (black), 0.025 (red), 0.05 (green), 0.075 (blue) and 0.1 (orange) in mole fraction of Li+. Details of the figure are illustrated in the text.

3.3. Results

FTIR spectroscopy was first used to study the solvation structure of Li^+ in the three ureas. Concentration-dependent IR spectra in carbonyl stretch region (1600-1700 cm^{-1}) are shown in Figure 3.1. The normalized FTIR spectra of urea-based electrolytes are similar to those of carbonate-based electrolytes where the pure ureas show only one band in the carbonyl stretch region and a low frequency band grows with the addition of Li^+.[74, 77, 158-163] Due to the change of the bands with Li^+ concentration, the high and low frequency bands have been referred as the free and coordinated band, respectively, which is the same convention used here. In the case of ureas, the free bands are located at ~1700 cm^{-1} for the cyclic urea (i.e., DMI) and at ~1650 cm^{-1} for the linear ureas (i.e., TMU and TEU). In contrast, the coordinated band appears at ~1685 cm^{-1}

for DMI, at ~1625 cm^{-1} for TMU, and at ~1612 cm^{-1} for TEU. It is important to note that DMI presents a small Fermi resonance in the high frequency side of the band (~1725 cm^{-1}) as seen in the spectra of DMI in different solvents (Figure 3.2). However, the Fermi resonance is significantly away from the free carbonyl band; thus, its presence is not expected to produce major changes in the analysis and it is not taken into consideration in our later analysis.

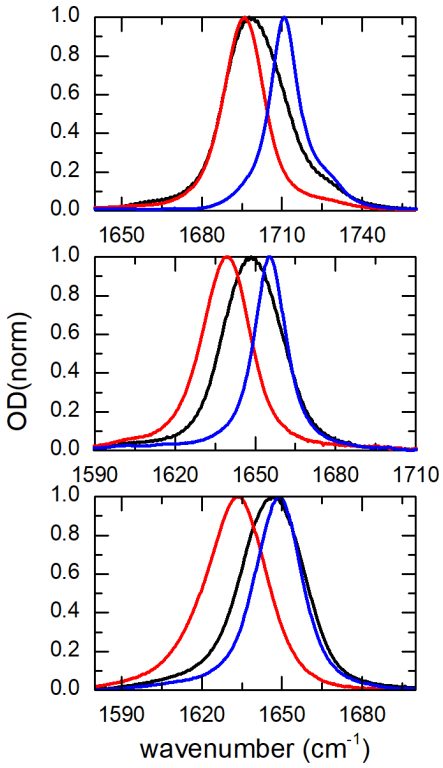

Figure 3.2. FTIR spectra of amides and amides diluted in DMSO and THF. From top to bottom, the spectra are from DMI, TMU and TEU, respectively. Black, red and blue represent neat amides, amides in DMSO and amides in THF, respectively.

The structure and dynamics of the Li^+ solvation shell formed by ureas were further investigated using 2DIR spectroscopy. 2DIR spectra collected for all three ureas with a LiTFSI concentration of ~1 M ($X(Li^+)$ ~ 0.1) are shown in Figure 3.3. In all the studied ureas, the 2DIR spectra present two pairs of peaks along the diagonal ($\omega_\tau=\omega_t$, shown as a black solid line) in accordance to the peaks observed in the FTIR (Figure 3.1). The red (right) peaks represent

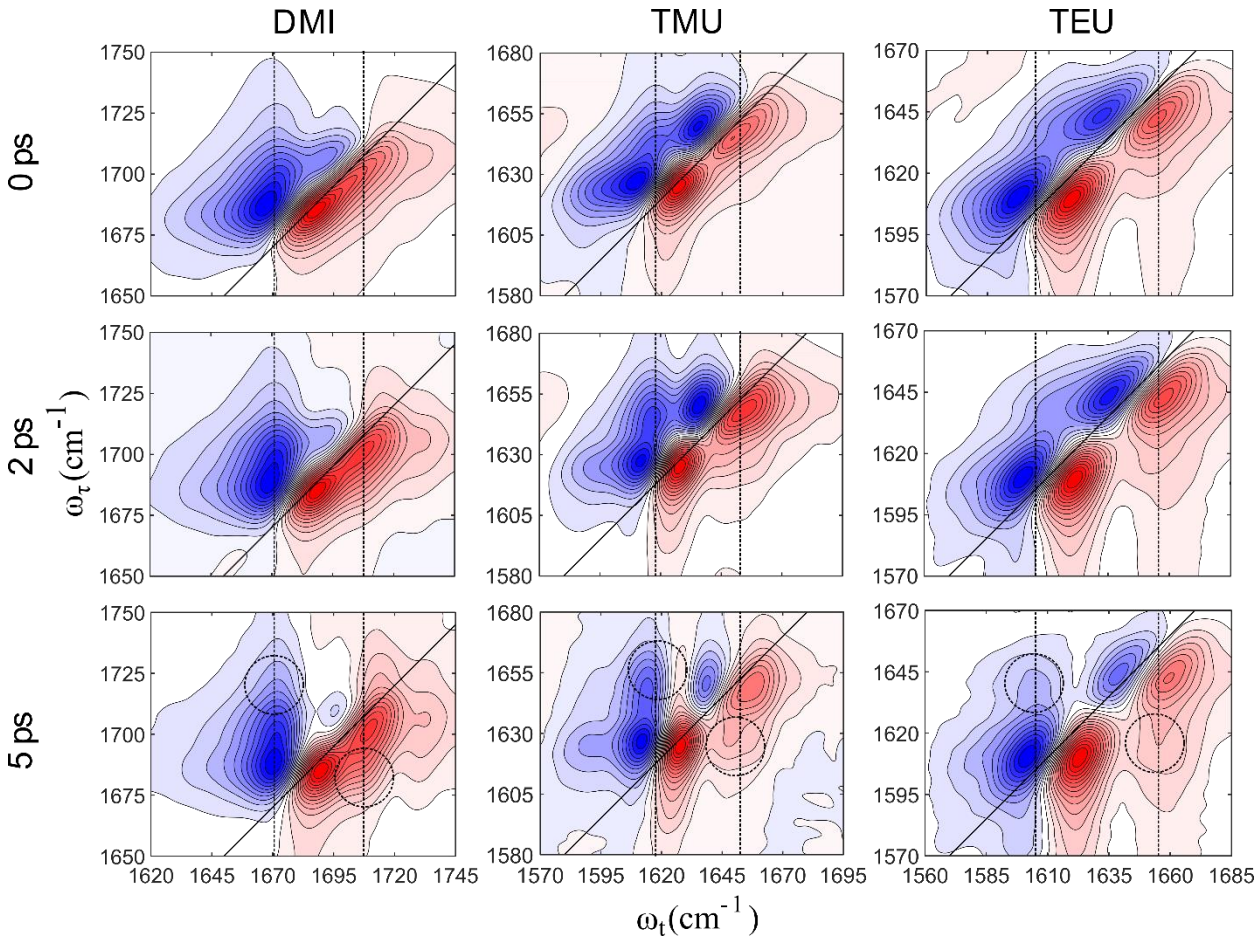

Figure 3.3. 2DIR spectra of ~1M LiTFSI in each of DMI, TMU and TEU at Tw = 0, 2 and 5 ps. Dashed lines show the approximate frequency locations of the peak and dashed circles highlight the cross peaks when they are most noticeable.

transitions between the ν = 0 and ν = 1 vibrational states and blue (left) peaks represent ν = 1 to ν = 2 vibrational transitions. As in the FTIR, the high frequency pair of peaks corresponds to the free carbonyl stretch, while the low frequency pair of peaks corresponds to the Li^+-coordinated carbonyl stretch. The waiting time dependence of the 2DIR spectra reveals that the peaks acquire a more upright shape from their initially elongated shape along the diagonal. This change in the shape of the peaks with waiting time evidences the process of spectral diffusion in these systems.[107] Further, the 2DIR spectra of all samples present off-diagonal features, denoted as cross peaks, which are evident at longer waiting time and in approximately the following

locations: (ω_τ, ω_t) = (1686 cm^{-1}, 1709 cm^{-1}) and (1710 cm^{-1}, 1671 cm^{-1}) for the DMI sample, at (1624 cm^{-1}, 1657 cm^{-1}) and (1647 cm^{-1}, 1618 cm^{-1}) for the TMU sample and at (1609 cm^{-1}, 1661 cm^{-1}) and (1643 cm^{-1}, 1590 cm^{-1}) for the TEU sample. The time dependence of the 2DIR spectra shows that the intensity of the cross peaks grows as waiting time progresses, which indicates that a dynamical process with a picosecond time scale is occurring in these systems, similar to the observations in the 2DIR spectra of Li^+ in organic carbonate.[74, 77, 83]

3.4. Discussion

3.4.1. Structure of the Li^+ solvation shell

Previously, the presence and growth of cross peaks in the 2DIR spectra was shown to be the spectral signature of either vibrational coupling or ultrafast chemical exchange.[107, 114, 150, 164] However, it was previously demonstrated for the carbonate solutions of Li+ that the cross peaks at Tw = 0 between the free and lithium-coordinated carbonyl stretch bands arise due to the vibrational coupling among C=O stretch modes of the tetrahedral solvation complex around Li+ since they showed to be polarization-dependent featutes.[77, 81, 165] Similarly, the cross peaks in the 2DIR data of ureas (Figure 3.3) could evidence a vibrational coupling mechanism between carbonyl stretch modes of the Li+ tetrahedral solvation complex. The mechanism behind the growth of the cross peak was also measured by polarization-dependent 2DIR spectroscopy for the three urea solutions at Tw=0. For pulse polarizations different from parallel (<XXXX>), the 2DIR spectrum containing vibrationally coupled transitions is expected to show enhanced cross peak because of the dependence of the third-order non-linear response with the pulse polarizations and the angle between the dipole directions of the two transitions, which in the case of ureas is 90°.[166, 167] The polarization dependence spectra show off-diagonal features that resemble to that of cross peaks (Figure 3.4), but no direct conclusion can be drawn from these

experiments due to their small amplitude of the off-diagonal features. Thus, the cross peak mechanism was further investigated by measuring the anisotropy dynamics of the coordinated peak for the TMU solution.

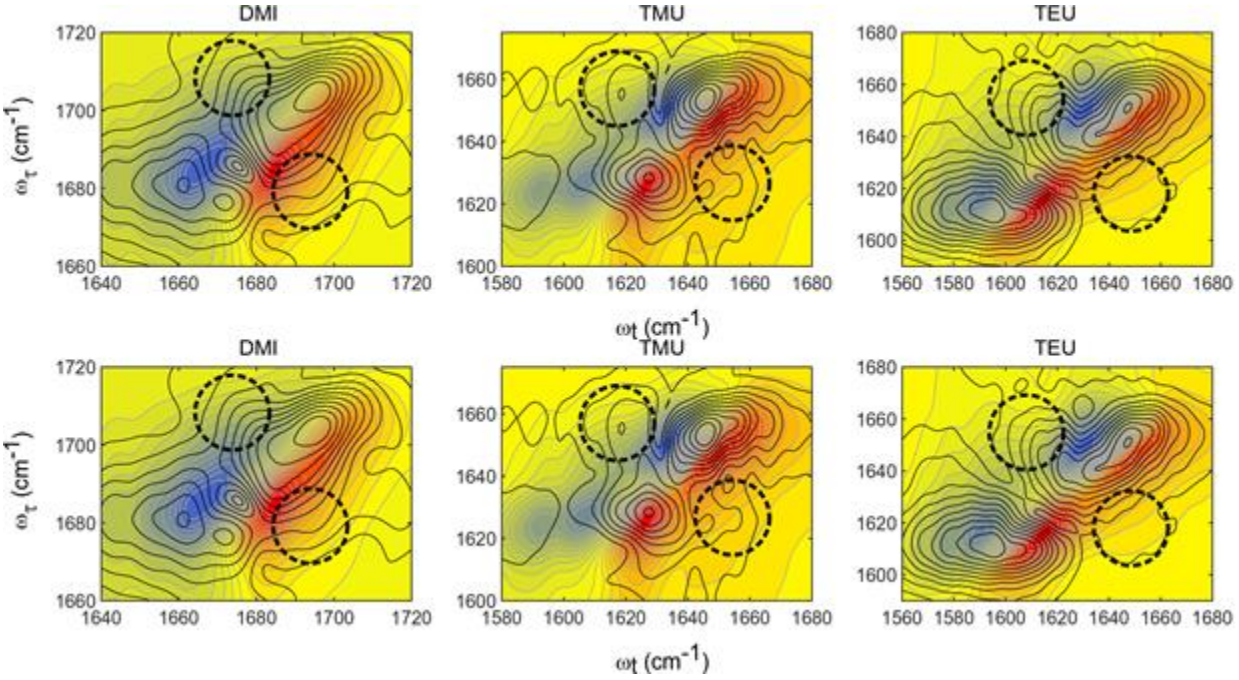

Figure 3.4. Absorptive 2DIR spectra of DMI, TMU and TEU at T_W=0ps in blue and red contours. The black contours show the absolute value of the different 2DIR spectra with <XXXX> and <XX, Y+X, Y+X>. The dashed circles show the location of the possible off-diagonal features.

The anisotropy displays an ultrafast decay with a characteristic time of ~0.9 ps for Li^+ in pure TMU, but its time scale becomes considerably larger (~5 ps) for a dilute solution of the urea in BC. (Figure 3.5) While one could interpret the result as a the system undergoing ultrafast chemical exchange as proposed by Cho and co-workers where the fast exchange dynamics causes the localization of the initially delocalized transition,[72] the 2DIR spectra of Li^+ in the same dilute solution of the urea (LiTFSI:TMU:BC=2:1:17), where coupling effects are inhibited, does not present a cross peak growing with waiting time. (Figure 3.6) This last result demonstrates not only that the cross peaks arise from the vibrational modes of the urea

tetrahedral solvation shell, but also that process of chemical exchange does not occur within the investigated time window. Furthermore, the result is in agreement with a recent ab-initio molecular dynamics simulation study of Li^+ in organic carbonates, which showed that the chemical exchange rates have time scales larger than 20 ps.[81] Overall, the data presented here provides a strong argument for supporting a mechanism of cross peak growth arising exclusively from vibrational energy transfer.

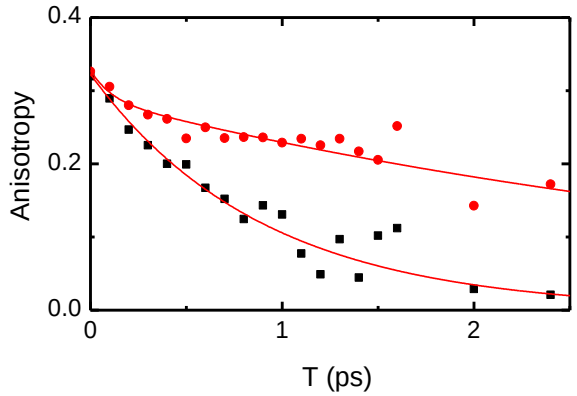

Figure 3.5. Anisotropy decay data (dots) of the solutions of Li+ in pure TMU (black squares) and in a dilute solution in BC (red circles) as described in text. The fitting models (red lines) are exponential decays with a characteristics time of ~0.9 ps and ~5 ps for pure TMU and TMU:BC mixture respectively.

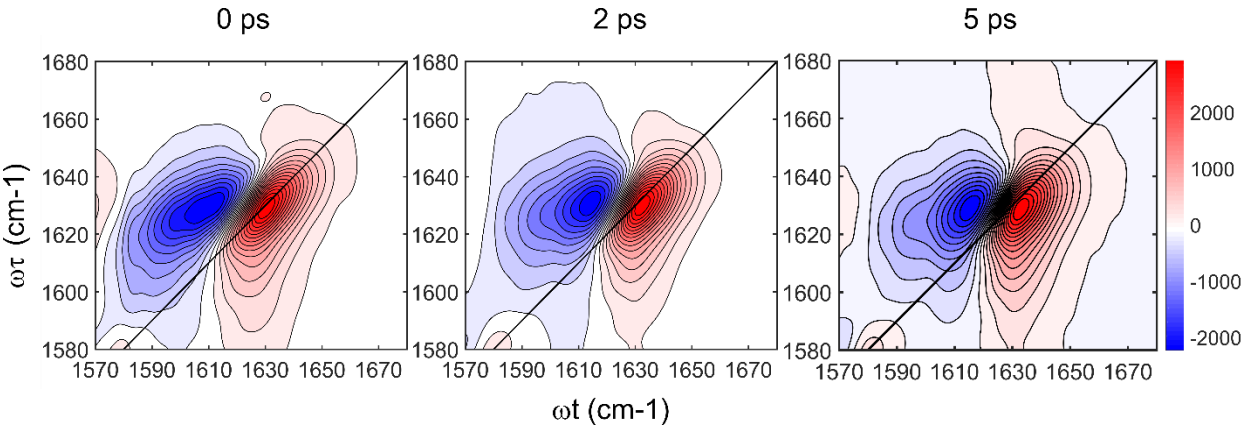

Figure 3.6. 2DIR spectra of dilute urea electrolyte, 0.1 LiTFSI in TMU and BC (molar ratio of Li:TMU:BC = 2:1:17). Left to right: 2DIR spectra at 0, 2 and 5 ps, respectively. CLS of the coordinated band for the diluted urea solution gives a dynamics much slower than 5 ps.

The mechanism of vibrational energy transfer could arise from energy transfer either between molecules in the first and second solvation shells or among urea molecules exclusively in the first solvation shell. Whereas the energy transfer between urea molecules in different solvation shell could occur, it has been previously observed for similar carbonates that the dipole of the molecules in the first and second solvation shells are separated by at least 4 Å.[81] In addition, it was previously demonstrated by Cho and co-workers via a dilution experiment that this mechanism was unlikely to occur.[71] Thus, it is likely that the vibrational energy transfer occurs entirely among molecules located in the first solvation shell.

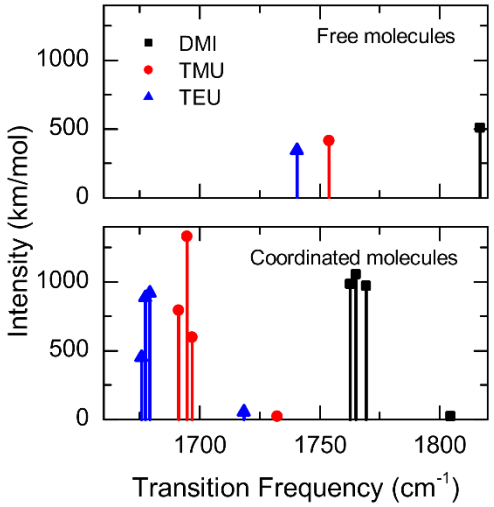

Figure 3.7. Results of frequency calculations from DFT. Top panel: frequencies of single ureas. Bottom panel: frequencies of four ureas coordinated to Li+, or Li(urea)$_4$+. For details, see Table 3.1.

In agreement with an energy transfer among molecules in the first solvation shell, the frequency location of cross peak demonstrates an underlying transition situated at the same frequency position as the free carbonyl band irrespective of the solvent. This high frequency band has been previously assigned to the symmetric carbonyl stretch combination mode for a tetrahedral arrangement of carbonyls around Li^+ with a Hamiltonian of the form:[77]

$$H(t) = \begin{bmatrix} \omega_{10}+\delta\omega(t)-\beta(t) & 0 & 0 & 0 \\ 0 & \omega_{10}+\delta\omega(t)-\beta(t) & 0 & 0 \\ 0 & 0 & \omega_{10}+\delta\omega(t)-\beta(t) & 0 \\ 0 & 0 & 0 & \omega_{10}+\delta\omega(t)+3\beta(t) \end{bmatrix} = \begin{bmatrix} \omega_{as}(t) & 0 & 0 & 0 \\ 0 & \omega_{as}(t) & 0 & 0 \\ 0 & 0 & \omega_{as}(t) & 0 \\ 0 & 0 & 0 & \omega_{s}(t) \end{bmatrix}$$

where ω_{10} is the transition frequency for each isolated carbonyl stretch, $\delta\omega(t)$ describes the time-dependent change in frequency for the modes and $\beta(t)$ defines the time-dependent coupling between the two vibrational modes.[74] In this model, the frequency difference between the symmetric and asymmetric transitions is given by 4β, which experimentally corresponds to ~4 cm^{-1}, ~6 cm^{-1}, and ~8 cm^{-1} for DMI, TMU and TEU, respectively. DFT computations (Figure 3.7) predict a tetrahedral solvation with a vibrational manifold of carbonyl stretches with three asymmetric stretches and one symmetric stretch, in which the former are fully allowed IR transitions and the latter is only weakly. Moreover, the computations also predict a frequency difference between the weakly allowed symmetric and the fully allowed asymmetric transitions of ~40 cm^{-1}, or equivalent, a coupling constant of $\beta = 10cm^{-1}$ for all the ureas (Figure 3.7), which is in reasonable agreement with the experiment. Thus, the formation of a tetrahedral solvation shell around Li^+ by ureas is also in agreement with DFT calculations. In addition, the DFT results are a direct indication of vibrational coupling among symmetric and asymmetric modes of the ureas in the solvation shell. One consequence of having a vibrational manifold with strong coupling among sites is that the resulting asymmetric and symmetric vibrational modes of the tetrahedral complex should have a cross peak in the 2DIR spectra. The cross peak arises from the combinational mode between symmetric and asymmetric carbonyl stretches in the two quanta vibrational manifold since the symmetric stretch is weakly allowed and the modes are coupled (Scheme 3.2).[77] Overall, the experimental features of the carbonyl stretch region observed in the linear and 2DIR spectra as well as the predicted modes by DFT computations support a Li^+

solvation shell with four ureas in a tetrahedral arrangement similar to the structure of organic carbonates.[6, 77, 80, 95, 149, 168-170]

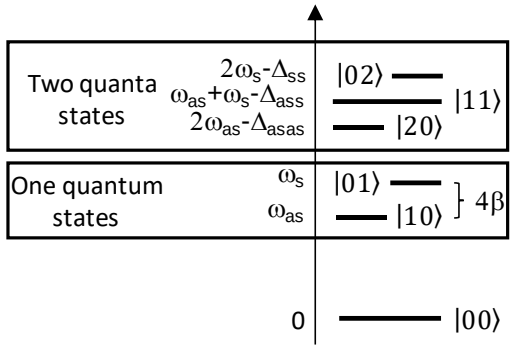

Scheme 3.2. Energy diagram describing a coupled, anharmonic, four-mode system where ω_{as} and ω_s represent the frequencies of the three degenerate asymmetric and one symmetric stretches, respectively, and Δs are their anharmonicities.

The structure of the solvation shell complex formed by ureas does not appear to differ significantly from other solvents such as carbonates.[6, 80, 149, 171-174] However, the linear IR and 2DIR spectra of the ureas appear to show significant differences with molecular structure. One difference is observed in the frequency difference between the free and coordinated bands of each urea (Figure 3.8), which is ~17 cm^{-1} for DMI, ~26 cm^{-1} for TMU and ~33 cm^{-1} for TEU. The change in the frequency shift among ureas of different structure contrasts the observations in carbonates where the shift is observed to be ~30 cm^{-1} irrespective of the molecular arrangement.[74, 77, 83, 158, 160-162] The molecular origin of the difference between free and coordinated frequencies for various ureas was investigated by dilution experiments. In this case, the solutions consist of LiTFSI, one urea and a co-solvent (acetonitrile, tetrahydrofuran or butylene carbonate) at a molar ratio of 2:1:17 (Li^+:urea:co-solvent). It is important to note that in these dilution experiments the possibility of having more than one urea molecule per Li^+

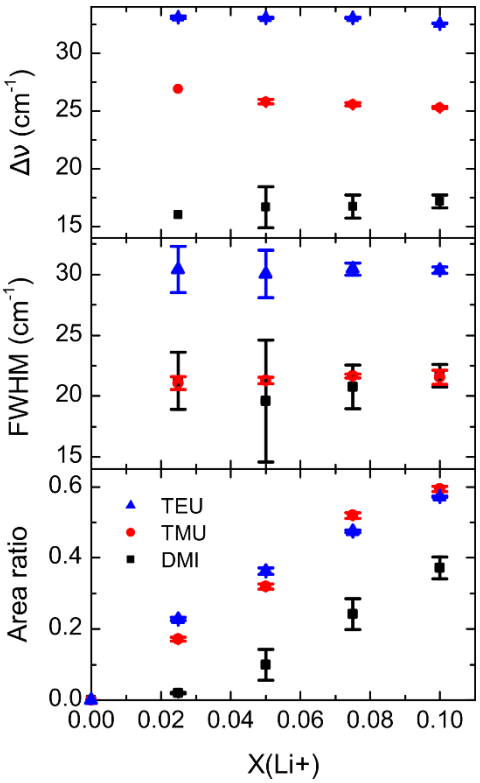

Figure 3.8. Parameters from modeling of the concentration-dependent FTIR spectra. Black, red and blue represent DMI, TMU and TEU, respectively. Top panel, frequency difference between coordinated and free peaks ($\Delta\upsilon_{exp}$) with concentration. Middle panel, full width at half maximum (FWHM) of coordinated peaks with concentration. Bottom panel, ratio between the area of coordinated peak and total area of both coordinated and free peaks, with concentration.

solvation shell is minimized at this concentration. In addition, the ureas in solutions of organic carbonates are predominantly coordinated to Li^+ since they have a higher interaction with the cation as compared to the organic carbonate.[159] The frequency differences ($\Delta\upsilon_{exp}$) between free and coordinated peaks in diluted solutions (LiTFSI:urea:co-solvent = 2:1:17) and in pure ureas (LiTFSI:urea = 1:9) show a strong correlation (Figure 3.9 and Figure 3.10), indicating that the frequency shift is not directly related to the shift caused by the vibrational coupling that gives rise to the formation of highly coupled vibrational transitions (excitons), but to the interaction between the urea molecule and Li^+. This last hypothesis is proved with DFT computations, which reveals a similar trend in frequency (Table 3.1 and Figure 3.11) as observed

experimentally; i.e., $\Delta\upsilon_{calc}$(TEU) > $\Delta\upsilon_{calc}$(TMU) > $\Delta\upsilon_{calc}$(DMI). In addition, natural bond orbital (NBO) analysis reveals that the frequency shift is caused by pure electronic effects since the C=O bond polarization in the presence of Li^+ follows the same trend as the frequency shift; i.e., TEU>TMU>DMI.[175] It is interesting to observe that this trend can be explained using the concept of electron donating ability of a group commonly used in organic chemistry: ethyl (TEU) > methyl (TMU) > methylene (DMI).

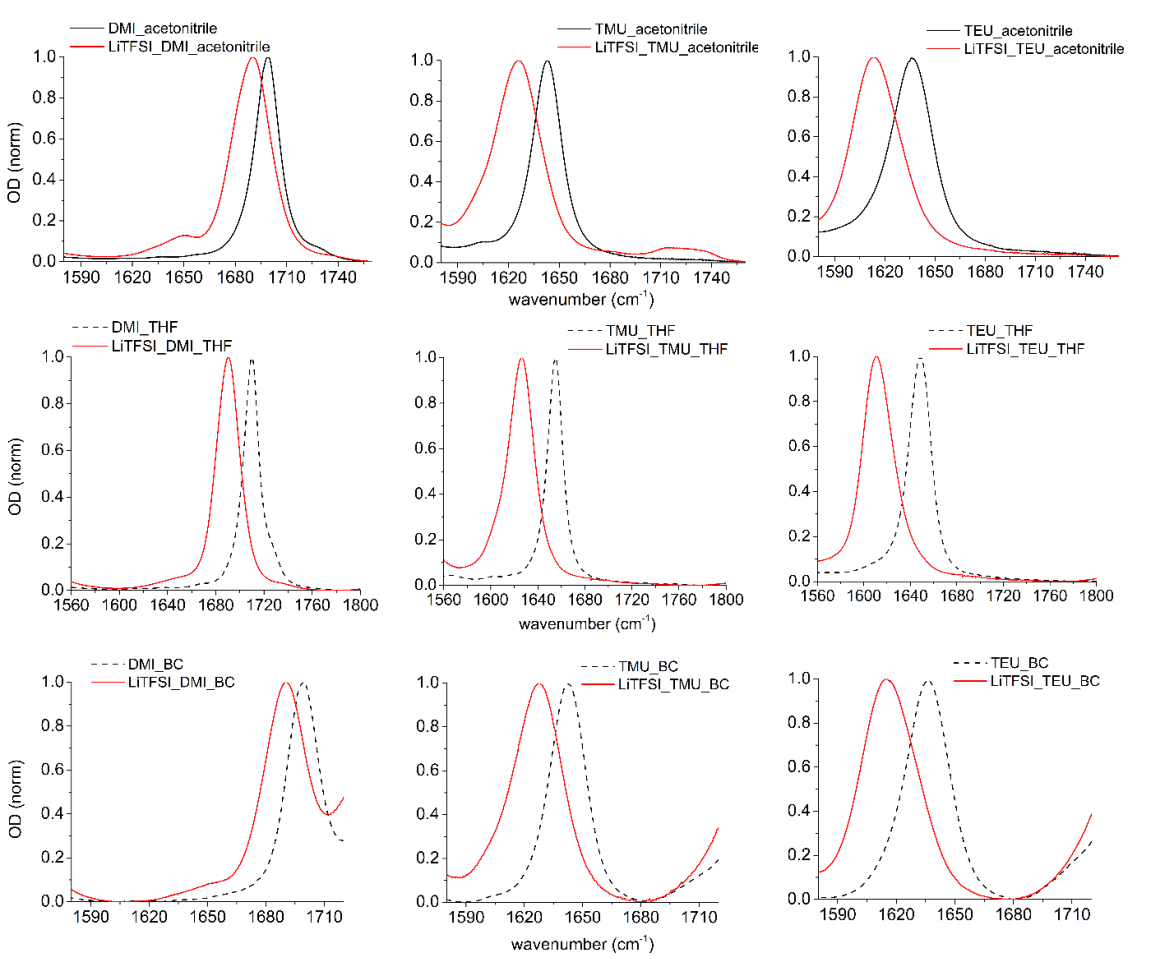

Figure 3.9. FTIR spectra of dilute experiments for LiTFSI in ureas and co-solvents. Molar ratio of LiTFSI:urea:co-solvent is 2:1:17. The upper panel shows the spectra in AN. The middle panel shows the spectra in THF. The lowest panel shows the spectra in BC.

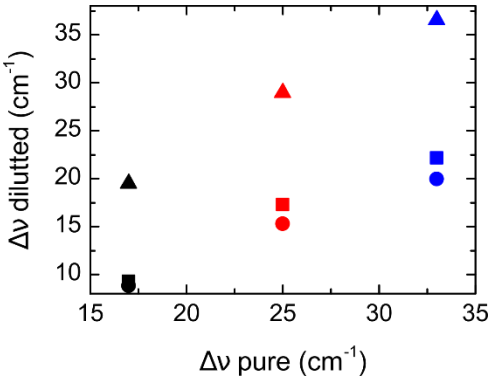

Figure 3.10. Frequency shift in solvent mixtures (LiTFSI:urea:solvent = 2:1:17) versus that in pure ureas (LiTFSI:urea = 1:9). Black, red and blue represent DMI, TMU and TEU, respectively. Square, circle and triangle shapes represent acetonitrile, butylene carbonate and tetrahydrofuran, respectively.

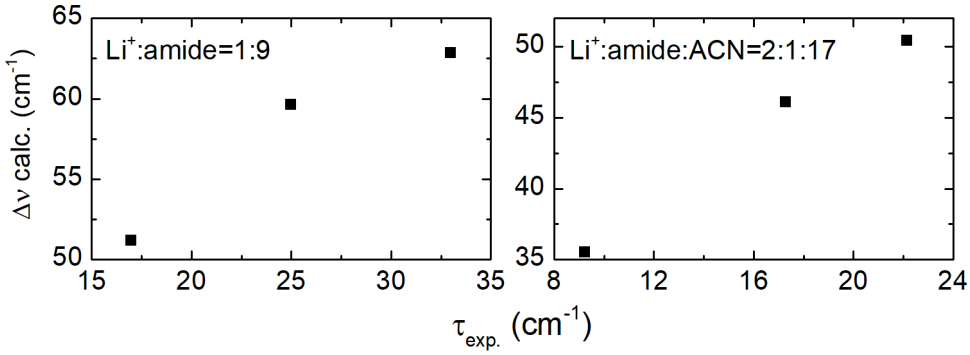

Figure 3.11. Frequency difference from DFT vs. frequency difference from FTIR. The regression coefficient is found to be R^2=0.97 (pure urea) and R^2=0.99 (dilute urea).

Table 3.1. Results of DFT frequency calculations for free and coordinated carbonyl stretching mode frequencies in ureas and urea-based electrolytes. All frequencies in cm^{-1} and intensities in km/mol.

Species	Free	Free	Symmetric	Symmetric	Asymmetric	Asymmetric
	Freq.	Intensity	Freq.	Intensity	Freq.	Intensity
$Li^+(DMI)_4$	1816.84	508.67	1804.66	25.00	1762.74	984.88
					1765.10	1052.42
					1769.27	969.42
$Li^+(TMU)_4$	1753.81	415.31	1732.26	21.69	1691.21	793.14
					1694.74	1331.85
					1696.85	599.42
$Li^+(TEU)_4$	1740.59	346.49	1718.38	55.46	1675.61	453.82
					1677.23	888.21
					1679.28	920.82

FTIR spectra with increasing concentration show that the area ratios of coordinated peaks, derived by Voigt modeling of the bands, present different growths among ureas. For example, the fractional areas of the coordinated bands in linear ureas are always larger than the cyclic analogue (Figure 3.8). The high fractional area of the Li^+-coordinated band in the urea solution is likely to indicate that Li^+-O=C angles are closer to 180°.[74] This result is also substantiated by the possibility of the intercalation of the cyclic urea molecules of the second solvation shell into the tetrahedral complex as seen from theoretical studies in organic carbonates.[81] In this case, the intercalation produces a more distorted solvation shell, which results in the decrease (increase) of transition dipole magnitudes for the asymmetric (symmetric) excitonic states of the urea solvation shell, or equivalently, a lower area ratio between coordinated and free bands. Thus, the higher coordinated area ratio in linear ureas is likely to indicate that these molecules form a more tetrahedral solvation complex, with respect to the Li^+-O=C angle, than their cyclic analogue. Finally, the concentration dependence of the area ratio for ureas shows that the area ratio of TEU and DMI grows non-linearly, while TMU grows almost linearly (Figure 3.8). This effect is likely to arise from any process that can distort the Li^+ tetrahedral solvation shell since a deformed tetrahedral solvation shell will decrease the transition dipole magnitude of the asymmetric stretch modes, but will increase the transition dipole magnitude of the symmetric stretch mode. Thus, the non-linear trend in the area ratio could be the result of the intercalation phenomenon or solvent separated ion pair formation. In both cases, the addition of ureas or anions to the solvation shell results in a less tetrahedral Li^+ solvation shell. Note that the change in the area ratio is not caused by the presence of contact ion pairs since the Raman spectrum (Figure 3.12) does not show the ~220 cm^{-1} band observed for the formation of contact ion pairs of TFSI.[78]

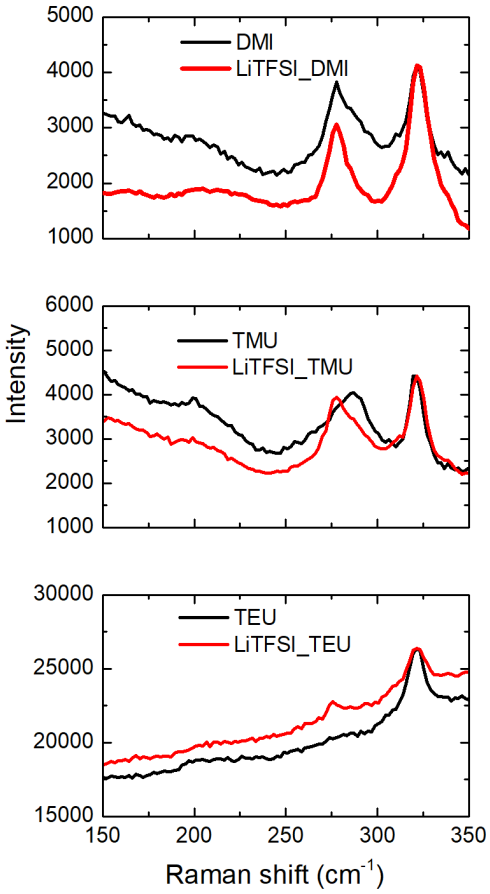

Figure 3.12. Raman spectra of 0.1 LiTFSI in ureas compared with the spectra of pure ureas.

Another spectral feature derived from modeling the FTIR spectra is the FHWM of the coordinated bands. For each urea, the carbonyl coordinated band did not show any significant change with Li+ concentration, which indicates that the structure and dynamics of the Li+ solvation is likely to remain invariant for the studied concentrations ($X(Li^+)$=0.02-0.1). However, the FWHM among ureas is observed to be different. While the FWHMs are comparable between TMU and DMI, both are smaller than TEU for any studied Li^+ concentration (Figure 3.8). The result is surprising given that the FWHM of the coordinated band of the cyclic carbonate doubles that of its linear analogue at any given Li^+ concentration.[77] Furthermore, the FWHM of the coordinated bands in any of the urea solutions is very similar to that of the linear carbonates.[74]

While the trend in the area ratios might indicate the possibility of cyclic urea intercalating into the primary solvation complex of Li^+, this phenomenon is expected to change the linewidth of the band as previously seen for cyclic carbonates.[163] However, in the case of the cyclic urea, the small separation of the bands produces an uncertainty in the FWHM of the coordinated band that does not allow us to confirm the expected trend in the FWHM as a function of Li^+ concentration. It is also possible that the additional methyl groups flanking the carbonyl group of the urea molecule inhibit the urea-urea interaction through steric interactions of these methyl groups.

3.4.2. Dynamics of the Li^+ solvation shell

Dynamics of the solvation shell is evident in the evolution of the 2DIR diagonal features with waiting time. This time evolution of the diagonal peaks is interpreted as the change of the correlation between the frequencies of the oscillators initially labeled by the IR pump (ω_τ) and the frequencies read by the IR probe (ω_t). Here, the characteristic time of the frequency-frequency correlation function (FFCF) was extracted using the center line slope (CLS) methodology.[124] The time evolutions of the CLS for both free and coordinated bands of each electrolyte are shown in Figure 3.13. For each solution, the time evolution of the CLS shows a temporal behavior, which is well modeled with an exponential decay of the form: $f(T_w) = A * e^{(-T_w/\tau)} + y_0$, where T_w is the waiting time, τ is the decorrelation time, and y_0 is an offset. The parameters obtained from modeling the CLS data are presented in Table 3.2. The CLS of the free band shows that TEU has the largest τ value (slowest dynamics), while DMI and TMU have similar dynamics but almost twice as fast as TEU. This result is not surprising given that TEU is the largest molecule and TMU and DMI have very similar structures, but both smaller than TEU. Interestingly, the frequency decorrelation dynamics of the coordinated band ($\tau_{TEU}>\tau_{TMU}>\tau_{DMI}$)

presents a similar trend as the free band ($\tau_{TEU}>\tau_{TMU}\approx\tau_{DMI}$). However, the coordinated FFCF shows a difference between TMU and DMI which is not observed on the FFCF of the free band. Moreover, it appears that DMI has a slow component as seen by the presence of an offset (Table 3.2), which could be caused by the intercalation of molecules from the second solvation shell.

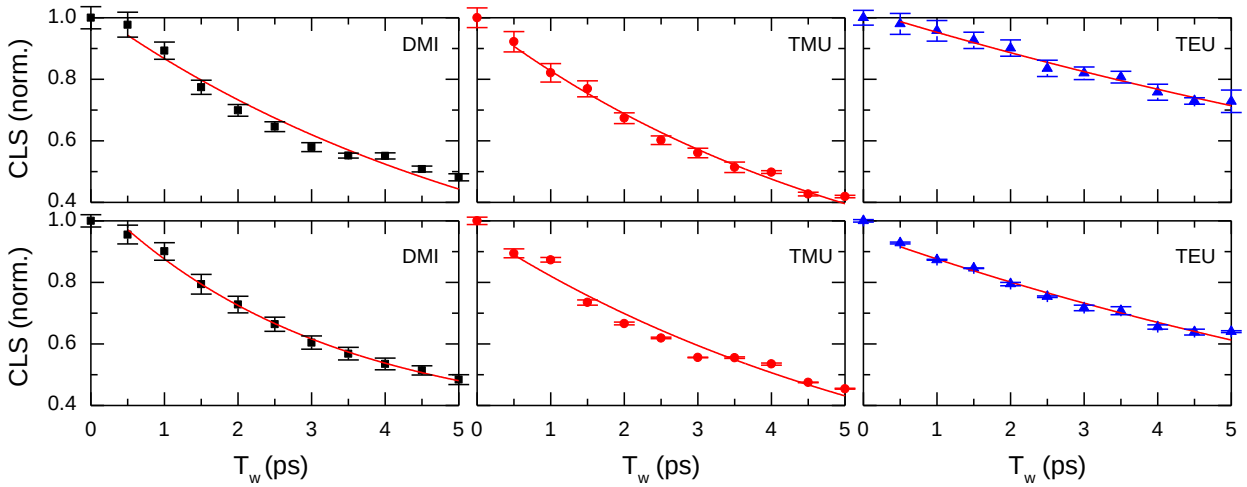

Figure 3.13. Normalized CLS time evolution for the free carbonyl stretch (top) and coordinated carbonyl stretch (bottom) of 0.1 LiTFSI in DMI (black squares), TMU (red circles) and TEU (blue triangles). Red lines correspond to the model fitting as described in the text.

Table 3.2. Model parameters for the fitting of experimental FFCF of the free and coordinated carbonyl stretch (Figure 3.13) and of the cross peak growth (Figure 3.15).

Solvent	Free	Coordinated	Coordinated	Cross peak growth
	τ (ps)	τ (ps)	offset*	τ_{et} (ps)
DMI	6.0 ± 0.4	3.1 ± 0.4	0.20 ± 0.04	2.3±0.2
TMU	5.4 ± 0.2	6.2 ± 0.4	--	2.2±0.3
TEU	13.9 ± 0.6	11.2 ± 0.5	--	1.2±0.3

The decays of both the coordinated and free carbonyl stretch FFCFs appear to be correlated to the size of the molecule. This result is in line with the decorrelation time of free molecules, given the larger size of TEU compared to the other two ureas. However, it has been previously shown that the dynamics of the tetrahedral solvation shell is related to the rate of the solvation shell deformation, due to the excitonic nature of the band.[77] The fast decay of the

anisotropy (Figure 3.5) shows that the initially delocalized exciton experiences a fast randomization of its dipole direction due to the mixing of the states from energy transfer. However, the ultrafast randomization of dipole orientation does not necessarily imply that the excitonic mixing is fully localizing the initially mixed states into a single urea. For example, a mechanism where the initial asymmetric state flips its transition dipole by 90˚ caused by population transfer among the three asymmetric stretches will also produce a decay in the anisotropy, but the mixing of the asymmetric modes does not necessarily imply that the delocalized modes will be localized to a single carbonyl stretch. Thus, the FFCF dynamics is likely to indicate the decorrelation of the solvation shell due to fluctuations of the coupling constant arising from deformation of the tetrahedral solvation shell of Li^+. This model is also supported by the frequency fluctuations observed in the urea dilute experiments (Figure 3.6) in which a single urea solvating Li^+ shows a very slow decay of the FFCF. In other words, the slow FFCF decay for a single site demonstrate that the motions of the other carbonyl groups and/or of Li^+ are not sufficient to produce a fast decorrelation and that the changes in the coupling constant must be primarily responsible for the fast decay of the FFCF of the coordinated band.

To test the feasibility of the deformation of the solvation shell as the mechanism of the FFCF, the potential energy surface around the Li^+-O=C equilibrium angle for the three ureas was computed (Figure 3.14 and Table 3.3). While this is one of the possible deformation coordinates for the solvation shell, it has been previously shown to be the most representative motion of the solvation shell coordinate of organic carbonates interacting with Li^+.[81] The computations reveal that all ureas have shallow potential wells, which allow the system to move in this molecular coordinate simply by thermal energy. Moreover, it is observed that the three ureas have similarly

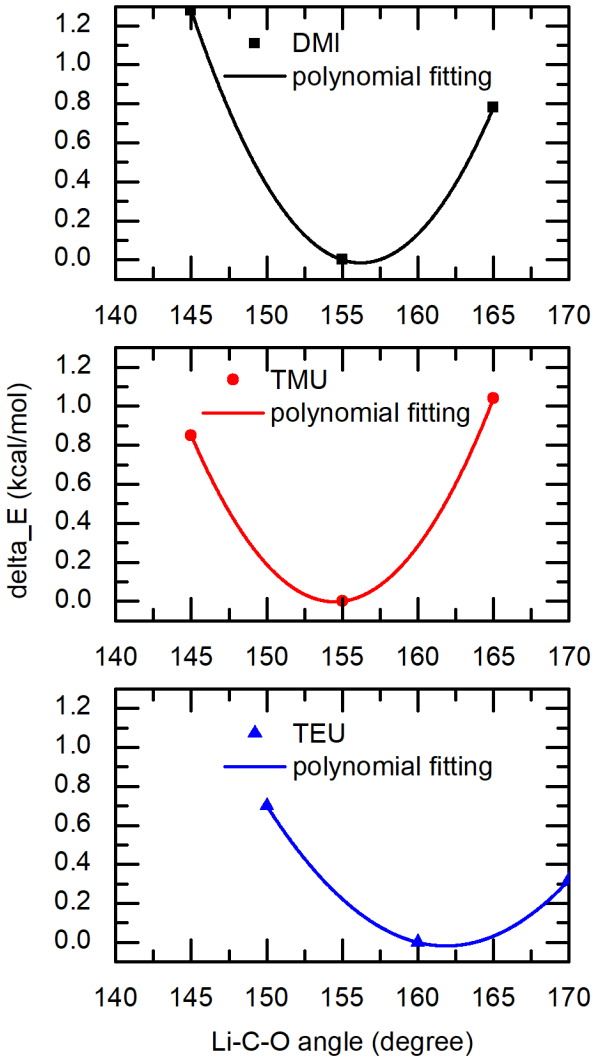

Figure 3.14. Potential surface of urea solvation shell vs. change in angle Li-C=O.

Table 3.3. Harmonic force constant k of data in Figure 3.14 with $V = \frac{1}{2}k(\theta - \theta_0)^2$.

Type	Force constant K (kcal/(mol.degree^2))
DMI	0.010
TMU	0.018
TEU	0.012

small harmonic force constants, indicating that the urea solvation shells can have fast thermal fluctuations. Finally, the motions in the Li^+-O=C coordinate also produce fluctuations in the

frequency on the order of ~5 to ~10 cm^{-1}, further supporting our hypothesis in which thermal deformations of the solvation shell are responsible for the observed FFCF dynamics of the urea coordinated band.

Another important dynamics of the system can be retrieved from the waiting time evolution of the off-diagonal features in 2DIR spectra. Off-diagonal features appear in the 2DIR spectra as a result of vibrational energy transfer or chemical exchange. Previous studies have demonstrated that at short time scales the mechanism responsible for cross peak is vibrational energy transfer among excitonic states formed by the vibrational coupling among molecules in the solvation shell.[74, 77, 81, 165] In this case, the carbonyl groups in Li^+ solvation shell are vibrationally coupled, generating combinational states between symmetric and asymmetric carbonyl modes in the second excited vibrational manifold.[107] These mixing modes cause the appearance of cross peaks in 2DIR spectra at all waiting times. In particular, the dynamics of cross peaks represents the rate of energy transfer between asymmetric and symmetric carbonyl stretch modes in the tetrahedral solvation complex, resulting from fluctuations in the angles between neighboring solvent molecules.[74, 77, 81, 83] Energy transfer is evident in the growth of the cross peak area relative to the diagonal peak area for the coordinated mode with increasing waiting time (Figure 3.15).[74, 176-179] Cross peak growth with T_w indicates that the Li^+ solvation shell undergoes deformations which change the vibrational coupling among carbonyls and produce a localization of the initially excitonic states.

The cross peak growth was determined by fitting the ω_τ traces of the 2DIR spectrum passing through the maximum of the coordinated band as a function of waiting time. The time dependence was modeled with an exponential growth of the form: $f(T_w) = A\left(1 - e^{(-T_w/\tau_{et})}\right)$, where τ_{et} is the characteristic energy transfer time (Table 3.2). The τ_{et} in these urea solutions has

a characteristic time of ~2 ps, which indicates that urea molecules have fast fluctuations of the tetrahedral structure of Li^+ solvation shell in agreement with the potential energy surface calculations. Moreover, the fast time constant observed for the cross peak growth validates the observed picosecond dynamics in the FFCF since the fluctuations of the vibrational coupling among carbonyl groups is likely the main mechanism for both FFCF and cross peak growth. However, to find the detailed connection between the fluctuations of the excitonic frequencies and the coupling constant of the urea carbonyls, a more detailed analysis such as those performed in references [180-182] is needed, which is beyond the scope of this study. The data also reveals the presence of an underlying oscillation, which might be attributed to coherence energy transfer pathways between the excitonic transitions.[74] In addition, it is observed that the oscillation is more pronounced for TEU than TMU, but barely noticeable in DMI. This result is in agreement with the FFCF dynamics trend ($\tau_{TEU}>\tau_{TMU}>\tau_{DMI}$) since fast fluctuations of the coupling (β) will rapidly dephase the coherence states producing the oscillation.

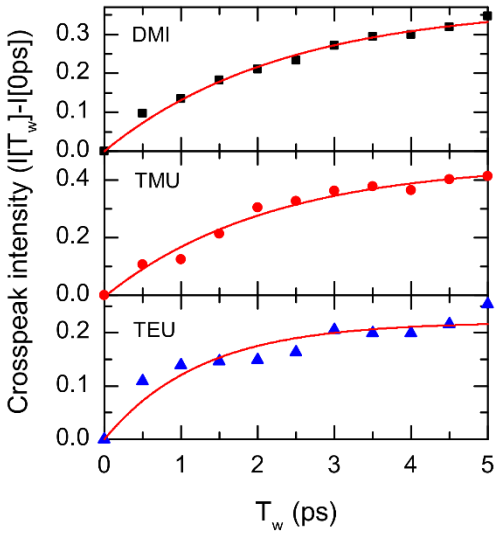

Figure 3.15. Growth of relative cross peak area for each electrolyte as a function of T_w in ps. Black, red and blue represent the cross peak growth for DMI, TMU and TEU, respectively.

3.5. Summary

The present study shows the characterization of the molecular structure and dynamics of the solvation shell around the lithium ion formed by ureas with different molecular structure. In particular, the characterization is focused on three ureas, in which two are linear (TMU and TEU) and one is cyclic (DMI). The experimental results in conjunction with theoretical calculations reveal that ureas form tetrahedral solvation shell, which is similar to other organic molecules containing carbonyl groups such as organic carbonates. In addition, it is observed that the C=O bond of the ureas is polarized more as the substituents in the nitrogen have more carbon atoms. Moreover, it appears that the width of the coordinated band is larger for the largest urea, which is likely to be attributed to its slow dynamics. In addition, the observed dynamics of the Li^+ solvation shell is in-line with the molecular structure of the ureas, where TMU and TEU have an overall faster dynamics than DMI likely due to the intercalation of cyclic urea molecules in the first solvation shell of Li^+, but TEU has slower rearrangements than TMU due to its size. Furthermore, it is observed that the deformation shell dynamics occurs on a picosecond time scale. The dynamics of the first solvation shell motions is observed through both the FFCF and cross peak growth as expected from excitonic transitions originated from the strong coupling among carbonyl groups of the urea molecules in the Li^+ solvation shell.

CHAPTER 4. MOLECULAR MOTIONS OF ACETONITRILE MOLECULES IN THE SOLVATION SHELL OF LITHIUM ION

Lithium ion solutions in organic solvents have become ubiquitous because of their use in energy storage technologies. The widespread use of lithium salts has prompted a large scientific interest in elucidating the molecular mechanisms, giving rise to their macroscopic properties. Due to the complexity of these molecular systems, only few studies have been able to unravel the molecular motions and underlying mechanisms of the lithium ion (Li^+) solvation shell. Lately, the atomistic motions of these systems have become somewhat available via experiments using ultrafast laser spectroscopies, such as two-dimensional infrared spectroscopy. However, the molecular mechanism behind the experimentally observed dynamics is still unknown. To close this knowledge gap, this work investigated solutions of a highly dissociated salt [LiTFSI: lithium bis(trifluoromethanesulfonyl)imide] and a highly associated salt (LiSCN: lithium thiocyanate) in acetonitrile (ACN) using both experimental and theoretical methods. Linear and non-linear infrared spectroscopies showed that Li^+ is found as free ions and contact ion pairs in ACN/LiTFSI and ACN/LiSCN systems, respectively. In addition, it was also observed from the non-linear spectroscopy experiments that the dynamics of the ACN molecules in the Li^+ first solvation shell has a characteristic time of ∼1.6 ps irrespective of the ionic speciation of the cation. A similar characteristic time was deducted from ab initio molecular dynamics simulations and density functional theory computations. Moreover, the theoretical calculations showed that molecular mechanism is directly related to fluctuations in the angle between Li^+ and the coordinated ACN molecule ($Li^+\cdots N{\equiv}C$), while other structural changes such as the change in the distance between the cation and the solvent molecule ($Li^+\cdots N$) play a minor role. Overall, this

This chapter was previously published as Chen, X.; Kuroda, D. G., "Molecular motions of acetonitrile molecules in the solvation shell of lithium ions," *The Journal of Chemical Physics*, 2020, 153 (16), 164502, copyright 2020 American Institute of Physics.

work uncovers the time scale of the solvent motions in the Li^+ solvation shell and the underlying molecular mechanisms via a combination of experimental and theoretical tools.

4.1. Introduction

The solvation of lithium salts in organic solvents has gained significant attention in the last ten years due to its direct implication for designing electrolytes in lithium ion battery (LIB).[5, 149, 183, 184] In the past, most studies had focused on the macroscopic electrochemical aspects of the electrolytes,[185-189] while only a few were able to study the molecular structure and dynamics of lithium ion electrolyte solutions.[74, 77, 81, 83, 190] In particular, the problem of elucidating the molecular arrangements and interactions in lithium salt solutions arises from the ultrafast changes in the speciation of Li^+ as well as the fast motions of the molecular components.[71, 72, 74, 77, 83, 165] To this end, many experimental methodologies have been utilized to study the structure and dynamics of lithium ion electrolyte solutions, including Raman spectroscopy,[10, 191, 192] X-ray scattering,[193-195] nuclear magnetic resonance (NMR),[196-198] mass spectrometry,[199-201] and linear infrared spectroscopy.[66, 74, 77, 92, 202, 203] In addition, theoretical studies using different levels of theories have been presented.[81, 171, 173, 204, 205] Notwithstanding the major findings of the previously used methodologies, the use of ultrafast infrared techniques to probe the molecular structure of lithium ion solutions has allowed us to gain dynamical information of the molecular motions occurring in these systems with a time resolution similar to that of the atomic.[74, 77]

It is now well accepted that dilute solutions of lithium salts have the lithium ions (Li^+) coordinating four solvent molecules (tetrahedral arrangement) when the solvent has one primary interaction site, such as carbonates and nitriles.[77, 79-81, 173, 206] At high concentration, the formation of contact ion pairs, solvent separated ion pairs and aggregates is observed, but the tetrahedral coordination of Li^+ is maintained.[77, 83, 92, 190, 202, 206] Time-resolved infrared spectroscopy enables

the investigation of the dynamics of the Li^+ solvation shell.[107] In particular, the motions of the first solvation shell have been probed through the carbonyl stretch of carbonate molecules coordinated to Li^+.[74, 77, 83] From those studies, the dynamics of the Li^+ solvation shell was found to occur with a characteristic time of a few picoseconds.[74, 77] However, in the non-linear IR studies, it has been very difficult to decipher the molecular mechanisms giving rise to the observed dynamics due to the vibrational couplings that lead to complex vibrational manifold for the solvent molecules in Li^+ solvation shell.

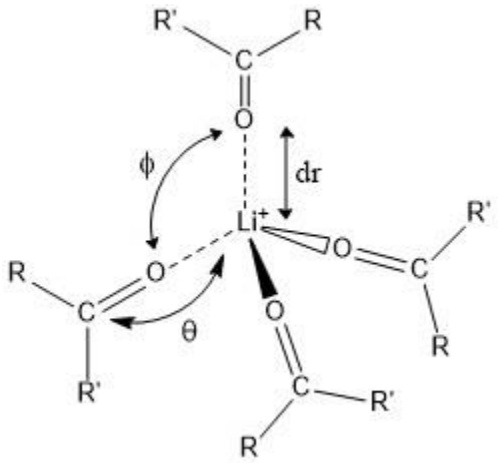

Scheme 4.1. Geometrical factors describing the Li^+ solvation shell of carbonyl containing solvent molecules.

In previous studies, the dynamics of the solvent (carbonates) molecules in the solvation shell were described in terms of three geometrical factors (Scheme 4.1): the distance between Li^+ and carbonyl oxygen atom (dr, $Li^+\cdots O$), the angle between Li^+ and coordinated carbonyl group (θ, $Li^+\cdots O{=}C$) and the angle between two coordinated carbonyl groups (ϕ, $O\cdots Li^+\cdots O$).[74, 77, 83] It is found that the potential well for the distance between Li^+ and coordinated carbonate molecule is narrow and deep, indicating that the thermal fluctuation of dr is highly restricted.[74, 81] While the distance between Li^+ and a single coordinated linear carbonate molecule appears to have an insignificant role in the Li^+ solvation shell motions, the fluctuations around the angles θ and ϕ

emerge as the motions dominating the rearrangements of the solvation shell at room temperature. Subsequent theoretical work has further supported that the thermal changes in the angular factors dominate the motions of Li^+ solvation shell since the characteristic times for the dynamics of their fluctuations match the dynamics observed in the experiments.[77, 81] It was also proposed that the most dominating factor in the motions of the Li^+ solvation shell is likely to be the angle ϕ as a result from the change in vibrational coupling for coordinated carbonyl stretches. Overall, the theoretical study supported the hypothesis that geometrical factors are good descriptors of the vibrational dynamics due to the strong vibrational coupling (excitonic nature) of the carbonyl stretch in carbonates. However, the excitonic nature of the vibrational manifold for coordinated carbonate molecules deterred the characterization of molecular motions of individual solvent molecules coordinated to Li^+. Thus, the direct link between the experimentally observed dynamics and the specific molecular motions is still missing. For this purpose, a solvent presenting low vibrational coupling is needed to characterize the molecular motions of individual solvent molecules coordinated to Li^+.

In this work, a combination of experimental and theoretical methods was employed to study the molecular mechanisms behind the dynamics of individual molecules in the Li^+ solvation shell. Acetonitrile (ACN-H3, Scheme 4.1) was chosen as a solvent because it has a dielectric constant higher than linear carbonates, and yet comparable to cyclic carbonates. In addition, the ACN-H3 molecule coordinates exclusively to Li^+ through its nitrile group, which can be probed via its nitrile (CN) stretch using IR spectroscopy, as previously demonstrated.[79, 207-209] To examine the CN stretching band, deuterated acetonitrile (ACN-D3) was used because it does not have the combination band found in nitrile stretching region.[210] Another key property of ACN is the transition dipole moment of its CN stretch, which is significantly lower than the

corresponding carbonyl stretch of carbonates (Table 4.1). Moreover, the small transition dipole of the nitrile stretch reduces substantially the vibrational coupling between adjacent molecules[107] and permits the characterization of the motions of individual ACN molecules in the Li^+ solvation shell via time-resolved IR spectroscopy.

Table 4.1. Dielectric constant of BC, DMC and ACN at 25 °C. Transition dipole moment magnitudes of CO stretch of carbonates, and that of CN stretch of ACN were obtained from DFT calculations of single molecules in gas phase.

Solvents	Dielectric constant, ε_r @ 25 °C	$\lvert\vec{\mu}_{01}\rvert^2$ (km/mol)
Butylene carbonate (BC)	56	779 (CO)
Dimethyl carbonate (DMC)	3	354 (CO)
Acetonitrile (ACN)	36	14 (CN)

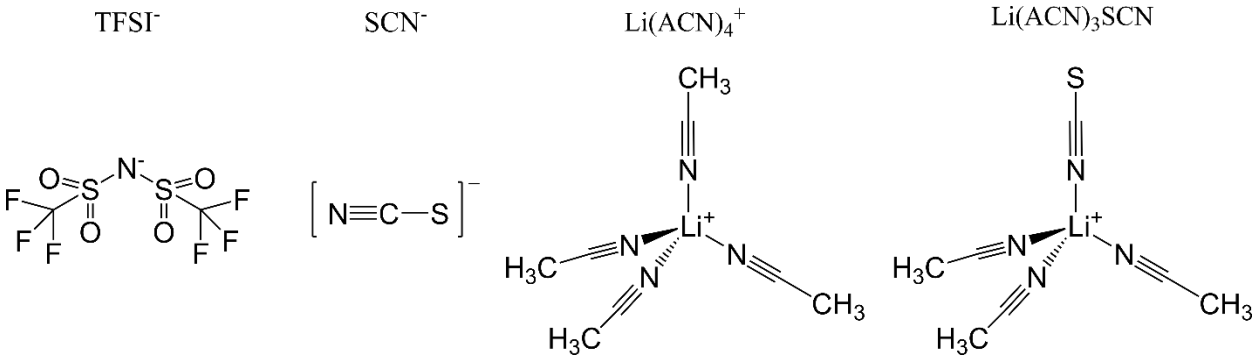

Scheme 4.2. Chemical structures of bis(trifluoromethanesulfonyl)imide ion ($TFSI^-$), thiocyanate ion (SCN^-), Li^+ coordinated to four acetonitrile molecules ($Li(ACN)_4$), and contact ion pair of Li^+ and SCN^- ($Li(ACN)_3SCN$).

The motions of the Li^+ coordinated ACN molecules as a function of the ionic speciation of Li^+ were also investigated. For this purpose, two different salts were selected: lithium bis(trifluoromethanesulfonyl)imide (LiTFSI, Scheme 4.2) and lithium thiocyanate (LiSCN, Scheme 4.2). In the LiTFSI/ACN system, it has been previously shown that most cations have solvation shells formed exclusively by solvent molecules.[51, 67, 97, 211] In contrast, the LiSCN/ACN solutions have the Li^+ forming contact ion pairs.[79, 212-214] Thus, the structure and dynamics of ACN molecules in different Li^+ solvation shells were studied using linear and time-resolved

infrared spectroscopies. In addition, the experimental studies were complemented with ab initio computations and molecular dynamic simulations to uncover the molecular mechanism behind the motions of the ACN molecules coordinated to Li^+.

4.2. Methods

4.2.1. Solution preparation

Tetrabutylammonium thiocyanate (TBASCN, 95% TCI) was used as received. Lithium bis(trifluoromethanesulfonyl)imide (LiTFSI, 98% Acros Organics), lithium thiocyanate hydrate ($LiSCN{\bullet}xH_2O$, LiSCN >63% Alfa Aesar), lithium perchlorate ($LiClO_4$, >95% Aldrich), acetonitrile (ACN-H3, 99% Fisher Biotech) and acetonitrile-D3 (ACN-D3, 99.8% isotope VWR) were dried before use. LiTFSI was dried in a vacuum oven under 150°C for 2 days. $LiSCN{\bullet}xH_2O$ was first dried in a vacuum oven under 60°C for 1 day and then under 110°C for 2 days. $LiClO_4$ was dried in a vacuum oven under 140°C for 2 days. ACN-H3 and ACN-D3 were dried with molecular sieves for 2 days prior to use.

Solutions of either LiTFSI or LiSCN in ACN-D3 were prepared at different concentrations with Li^+ molar fractions of 0, 0.01, 0.025 and 0.05, where the molar fraction of Li^+ (i.e., $X(Li^+)$) is defined as the moles of Li^+ over the total moles of both Li^+ and solvent. Solutions of TBASCN and $LiClO_4$ in ACN-H3 were prepared at different $X(Li^+)$ concentrations (0, 0.01, 0.02, 0.025 and 0.05) while the molar fraction of SCN^- was kept at $X(SCN^-) = 0.05$ in all solutions. Note that TBASCN was used to describe the free ion because it has been previously observed that its presence does not perturb the anion, which allowed us to investigate the speciation of the thiocyanate ion. Sample cells for FTIR and 2DIR consisted of the ACN-D3/Li^+ solution sandwiched between two CaF_2 windows with or without spacer according to the required optical density of the sample. All samples and sample cells were prepared in a N_2-filled

glovebox to minimize water contamination. All prepared samples tested less than 100 ppm of water after preparation. Note that in the rest of the manuscript ACN refers to ACN-D3 unless otherwise noted.

4.2.2. Fourier transform infrared spectroscopy (FTIR)

FTIR experiments were performed on a Bruker Tensor 27 equipped with a liquid nitrogen cooled MCT detector with a spectral resolution of 0.5 cm^{-1}. Reported spectra were averaged over 40 scans. FTIR data were modeled using OriginLab software.

4.2.3. Two-dimensional (2D) IR spectroscopy

The setup used for 2DIR experiments has been previously detailed in the literature, so only a short description is provided here.[107, 150] The input IR pulses were generated with a Spectra Physics Spitfire Ace Ti:sapphire amplifier at a repetition rate of 5 kHz, in combination with an OPA-800C and difference frequency generation crystal. These input IR pulses were then split into three replicas and later focused on the sample using the well-known boxcars geometry.[215] The photon echo signal was measured in the $-k_1 + k_2 + k_3$ phase-matching direction. A heterodyned detection was performed using a fourth pulse (local oscillator). The heterodyned signal was measured in a 64-element MCT array detector after dispersing the heterodyned signal in a spectrometer. The photon echo signal was measured as a function of three critical time intervals: the coherence time τ (interval between pulses 1 and 2), the waiting time T_w (interval between pulses 2 and 3), and the coherence time t (interval between pulse 3 and the detected signal). These time intervals were set via computer-controlled translation stages. Here, 2DIR data were collected by scanning τ time from −4 to +4 ps in increments of 5 fs for each waiting time to collect both the rephasing and nonrephasing data by switching the time ordering.[180] Signals were collected for waiting times from 0 to 3 ps in steps of 0.25 ps. The

data collection in waiting time was confined to a maximum of 3 ps due to the presence of heating effects.[92, 216, 217] In all of the measurements, the local oscillator always preceded the photon echo signal by ~0.6 ps. The time domain signal, collected as a function of (τ, T_w, λ_t) via a monochromator-array detection, is transformed into the 2DIR spectra (ω_τ, T_w, ω_t) by means of Fourier transforms. A detailed explanation of the Fourier analysis has been described elsewhere.[218]

4.2.4. Ab initio molecular dynamics simulations (AIMDS)

The AIMDSs were carried out with the CP2K package (version 3.0).[219] The electronic structure was calculated via Quickstep module[219] using the PBE functional with the D2[220] dispersion scheme and the TZV2P basis set, with Goedecker-Teler-Hutter (GTH) pseudopotentials.[221-223] Periodic boundary conditions were applied to all the systems, and the Nosé-Hoover thermostat was used to keep the temperature constant at 300 K, with the temperature damping constant of 100 fs. A self-consistent field (SCF) convergence criterion was set to 5.0×10^{-7} hartree. The plane wave cutoff was set to 400 Ry.[224] The ACN/LiTFSI system was composed of 1 lithium ion (Li^+), 1 bis(trifluoromethanesulfonyl)imide ion ($TFSI^-$) and 61 acetonitrile-t3 (ACN-T3) in a cubic box with a length of ~17.5 Å. The ACN-T3 (i.e., all hydrogens (H) were replaced by tritium (T)) is required for 1.0 fs time steps in the AIMDSs.[171, 225] Similarly, the ACN/LiSCN system was composed of 1 Li^+, 1 thiocyanate ion and 61 ACN-T3 molecules in a cubic box with a length of ~17.5 Å. In this paper, both box compositions are representative of dilute lithium solutions in acetonitrile (i.e. $X(Li^+) \leq 0.05$) since aggregates are not found at significant concentrations in dilute solutions.[83, 190, 209, 226]

The initial lithium solvation shell of LiTFSI in ACN-T3, consisting of a Li^+ coordinated to 4 acetonitrile molecules (tetrahedral solvation shell), was first optimized by Gaussian 09.[227]

Similarly, the initial structure of LiSCN contact ion pair in ACN-T3, consisting of a Li^+ coordinated to 3 acetonitrile molecules and 1 SCN^-, was also optimized by Gaussian 09.[227] Each optimized solvation shell was then submerged in a box containing the rest of the acetonitrile molecules using Packmol.[228] The molecular box with restraints on the molecules forming the first solvation shell of lithium underwent a minimization run over 500 cycles, a 2 ns NVT and 2 ns NPT process using AMBER software package and GAFF force field.[229, 230] These preparation steps were required to assure the equilibration of the box while maintaining the correct solvation structure around Li^+. In the starting structure of AIMDS, the distance between Li^+ and the N atom of $TFSI^-$ was set at 9.6 Å in the ACN/LiTFSI system, while the distance between Li^+ and the N atom of thiocyanate ion was set at 2.1 Å in the ACN/LiSCN system. In the AIMDSs, the systems were equilibrated for ~20 ps, and the production run was carried out in the NVT ensemble for another ~180 ps.

4.2.5. DFT calculations

DFT calculations were performed with Gaussian 09 software at the PBE1PBE level of theory using the 6-311++G** basis set.[227] In order to obtain reasonable results of structure optimizations and frequency calculations, the initial geometries of the lithium solvation shells were captured from the AIMDS. The captured structure of tetrahedral solvation shell and contact ion pair contained not only the first solvation shells of Li^+ but also appropriate amount of acetonitrile molecules from the second solvation shell. Structure optimization and frequency calculations were performed in the gas phase unless otherwise noted.

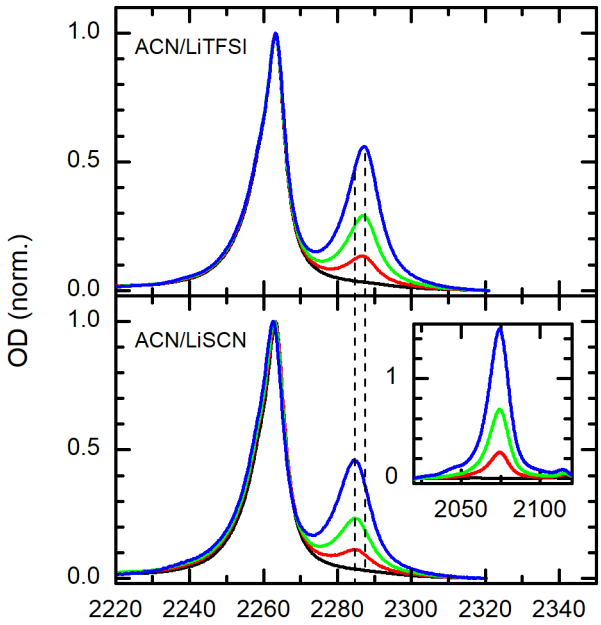

Figure 4.1. Concentration-dependent FTIR spectra in the nitrile stretch region. Top panel corresponds to ACN/LiTFSI in the ACN nitrile stretch region. and bottom panel corresponds to ACN/LiSCN in the ACN nitrile stretch region. The inset in the bottom panel shows the same sample in both ACN and thiocyanate nitrile stretch region. The display concentrations are X(Li^+) = 0 (black), X(Li^+) = 0.01 (red), X(Li^+) = 0.025 (green) and X(Li^+) = 0.05 (cyan).

4.3. Results

4.3.1. FTIR spectroscopy

Linear IR spectroscopy was first used to study the structure of LiTFSI and LiSCN in ACN. Concentration-dependent infrared (IR) spectra in the CN stretching region of ACN (2220 cm^{-1} to 2320 cm^{-1}) are shown in Figure 4.1. In pure ACN, only one asymmetric band is observed at ~2260 cm^{-1}. This band is asymmetric due to an overlap of hot band transition in the low-frequency side.[231-233] The addition of lithium salt gives rise to a new band at the high-frequency side (~2285 cm^{-1}) of the solvent CN stretch band, which becomes more pronounced when the concentration of Li^+ increases. Due to the direct increase of the high frequency band with the addition of salt, the low-frequency and high-frequency bands have been assigned to free and Li^+-coordinated CN stretching bands, respectively.[79] It is to be observed that the spectra reported

here are similar to the spectra from previous studies on similar systems.[79, 207-209, 234, 235] In addition, it is observed in the case of LiSCN in ACN that a band at 2074 cm^{-1} grows with the addition of the lithium salt. This downshifted band corresponds to the nitrile stretch of the anion.

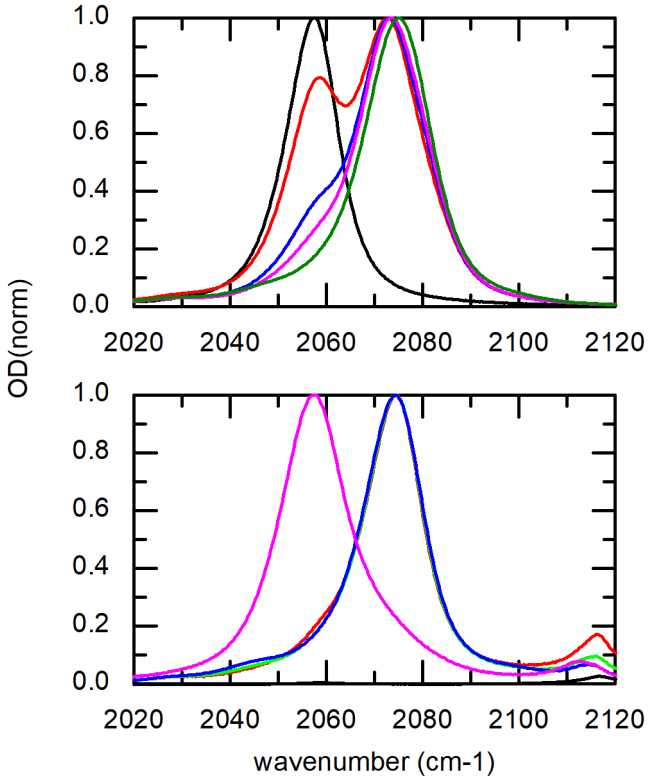

Figure 4.2. Upper panel: ACN solutions with mixed salts of TBASCN and $LiClO_4$ with $X(Li^+)$ equal to 0 (black), 0.01 (red), 0.02 (cyan), 0.025 (magenta) and 0.05 (green). Lower panel: LiSCN in ACN-d3 in the thiocyanate CN stretching region with $X(Li^+)$ equal to 0 (black), 0.01 (red), 0.025 (green) and 0.05 (cyan) as well as 0.05 TBASCN in ACN-d3 (magenta). All spectra were normalized.

It is now well accepted that at low concentrations Li^+ and $TFSI^-$ remain dissociated in high dielectric organic solvents, such as ACN.[51, 67, 97, 211] In addition, previous research has evidenced a solvent coordination number of four in dilute ACN/Li^+ solutions.[67, 79, 207-209, 234, 235] Thus, it is expected that most Li^+ will coordinate four ACN molecules at the investigated concentrations ($0 \leq X(Li^+) \leq 0.05$) in the ACN/LiTFSI system. On the other hand, LiSCN has been proven to be a highly associated salt that can form contact ion pairs (CIPs) in organic

solvents.[79, 212-214] The speciation of SCN^-, characterized using its CN stretch band, allows us to reach the same conclusion. First, a sample containing SCN^- with a non-perturbing cation (TBA) shows a peak at 2057 cm^{-1} (Figure 4.2), which is downshifted by ~20 cm^{-1} from the peak seen for LiSCN in ACN (Figure 4.1). Second, a concentration-dependence of a mixture of TBASCN with varying amounts of $LiClO_4$ shows the rise of the CIP peak at ~2075 cm^{-1} with the addition of Li^+ (Figure 4.2). These results are similar to observations previously made for LiSCN in dimethylformamide, which is a high dielectric constant solvent.[214]

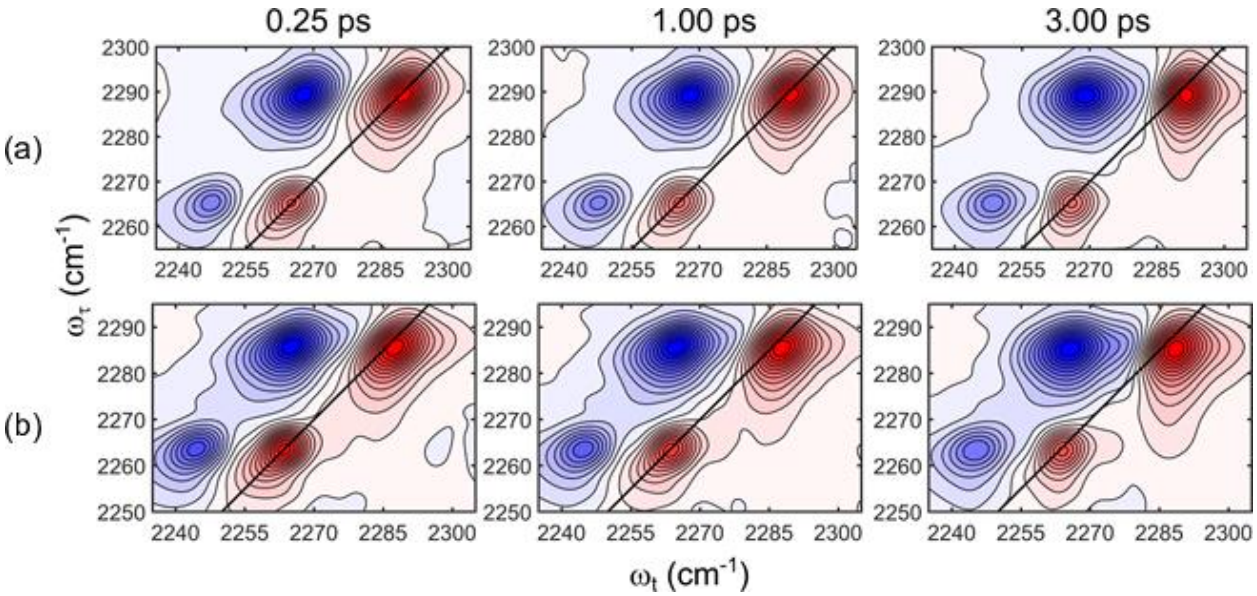

Figure 4.3. 2DIR spectra of (a) LiTFSI in ACN (top panels) and (b) LiSCN in ACN (bottom panels) with $X(Li^+)$ equal to 0.05. The spectra at waiting time of 0.25 ps, 1 ps and 3 ps are shown in left, middle and right panels, respectively.

4.3.2. 2DIR spectroscopy

To gain more structural and dynamical information of the ACN/Li^+ solutions, the 2DIR spectra were collected for the two systems ACN/LiTFSI and ACN/LiSCN at $X(Li^+) = 0.05$. The 2DIR spectra in the region corresponding to the CN stretch of ACN are shown in Figure 4.3. The data was analyzed for waiting times up to 3 ps due to the presence of heating effects.[92, 212, 216, 236] In both solutions, the 2DIR spectra have two pairs of peaks on top of the diagonal line

represented by the solid black line. These red positive peaks are attributed to third order non-linear response arising from the transitions between v=0 and v=1 vibrational states of ACN, while the blue negative peaks downshifted by ~24 cm^{-1} correspond to non-linear signals arising from the transitions between v=1 and v=2 vibrational states. The pair of peaks on the low-frequency and high-frequency side of the 2DIR spectra are the same free and coordinated CN bands seen in the FTIR spectra, respectively.

The waiting time evolution of the spectra shows that the main peaks are more tilted along the diagonal line at early waiting time, indicating the pump and probe frequencies are correlated. However, the 2DIR peaks become more upright at later waiting times, depicting the loss of correlation between pump and probe frequencies as the waiting time progresses. The peak shape dependence with waiting time showcases the randomization of the initially pumped frequencies (spectral diffusion process) in these systems.[107] Interestingly, the peak shapes evolve rapidly within the first 2 ps and only change marginally afterwards for both samples. In addition, the 2DIR spectra do not present off-diagonal features within the first 2 ps.

4.4. Discussion

4.4.1. Speciation of Li^+

The FTIR spectra (Figure 4.1) show only two peaks in the CN stretching region of ACN for either LiTFSI or LiSCN samples. The result indicates that in each solution the solvent is mainly observing two different molecular environments; i.e., bulk solvent and Li+ solvation shell. Li+ is known to form tetrahedral solvation shell in most organic solvents with single coordination sites.[67, 77, 237-240] Thus, the coordinated peak (high frequency) seen in the

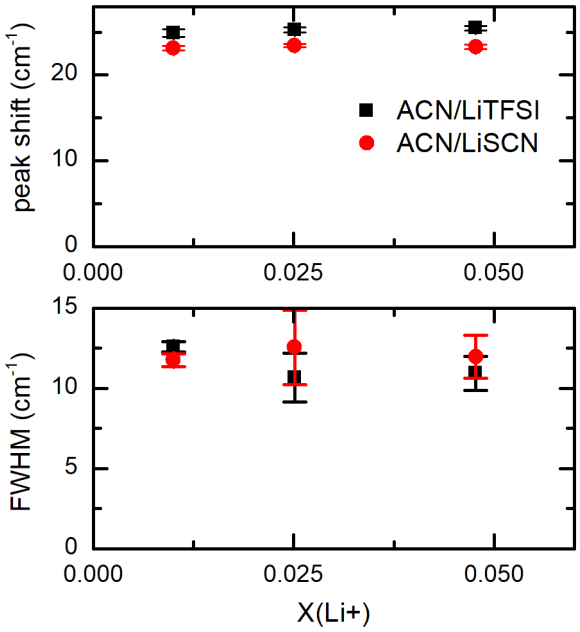

Figure 4.4. Lineshape parameters of the coordinated nitrile stretch of ACN as function of Li+ concentration. Top and bottom panels display the peak shift from free peaks to coordinated peaks and the full width at half maximum (FWHM) of coordinated peaks, respectively. Black squares and red circles represent the LiTFSI/ACN and LiSCN/ACN samples, respectively.

Table 4.2. DFT computations of Li^+ binding SCN- through S or N, calculated in gas phase and polarizable continuum (PCM) using two types of methods (PBE1PBE and MP2). Energy of Li^+ binding SCN^- through S or N reported as the energy difference (ΔE) in kcal/mol with respect to the minimum of energy.

Structure	ΔE (kcal/mol)	ΔE (kcal/mol)	ΔE (kcal/mol)
	PBE1PBE (gas)	MP2 (gas)	PBE1PBE (PCM)
Li---N≡C-S, (through N)	0	0	0
Li---S-C≡N, (through S)	26	23	6

ACN/LiTFSI samples correspond to the ACN molecules in the first solvation shell of Li+. Moreover, the coordinated peak positions relative to the free peaks and the full width at half maximum (FWHM) of coordinated peak (Figure 4.4) remain almost invariant with increasing Li^+ concentration, demonstrating that there is no obvious change in the speciation of Li^+ within the investigated range of concentrations. This last result is in agreement with the large dissociation presented by this salt in ACN.[67] In the case of ACN/LiSCN, Li^+ predominantly exists as a contact

ion pair with a tetrahedral solvation shell which includes the SCN-. It is important to note that in the LiSCN CIP, the anion coordinate Li^+ through the N atom rather than the S atom (Table 4.2).[212] Thus, the two peaks at low- and high-frequency side seen in the CN stretching region of ACN for LiSCN are assigned to free and Li^+-coordinated ACN molecules in the CIP, respectively. Similar to the case of LiTFSI, the spectra of ACN/LiSCN shows a constant relative peak position and FWHM as functions of Li^+ concentrations (Figure 4.4).

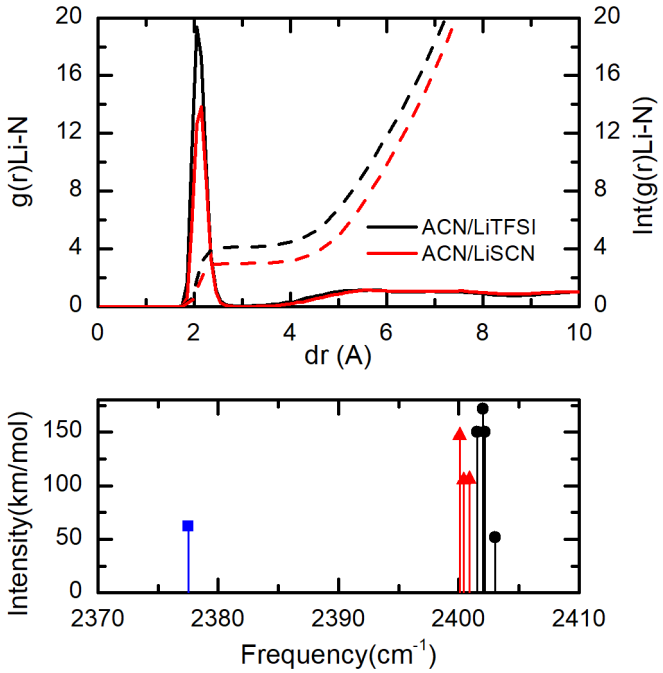

Figure 4.5. Computational results. Top panel shows the radial distribution function (RDF) between Li^+ and nitrogen atom of the coordinated ACNs (g(r)Li^+-NACN, solid line) and its integrated RDF (Int(g(r)Li^+-NACN), dash line) from AIMDS. Black and red correspond to the LiTFSI and LiSCN solutions in ACN, respectively. Bottom panel depicts the DFT frequency calculations (PCM) for free and coordinated ACN. Blue squares, black circles and red triangles represent the frequencies and intensities of the nitrile stretch in a single ACN molecule, in tetrahedral solvation shell of free Li^+ ($Li(ACN)4^+$), and its CIP (Li(ACN)3(SCN)), respectively. The geometry used for these calculations can be found in the SI.

The FTIR spectra of ACN/LiTFSI and ACN/LiSCN appear to be similar (Figure 4.1), but a close inspection reveals that the relative peak position of the coordinated CN of ACN is slightly more upshifted for LiTFSI samples (~25 cm^{-1}) as compared to LiSCN samples (~23 cm^{-1}). This

difference in the relative peak position is attributed to the different speciation of Li^+, which in the case of LiTFSI is mainly $Li(ACN)_4^+$ and in the case of LiSCN is $Li(ACN)_3(SCN)$. The assignment is supported by DFT computations , where a similar upshift of the CN stretch of ACN is seen for the $Li(ACN)_4^+$ when compared to $Li(ACN)_3SCN$ solvation shells (Figure 4.5). Finally, the deduced speciation is also in agreement with the AIMDSs. The radial distribution functions between Li^+ and the nitrogen atom of the coordinated ACN ($g(r)Li\text{-}N_{ACN}$) and the integral of $g(r)Li\text{-}N_{ACN}$ ($int(g(r)Li\text{-}N_{ACN})$) show that in the LiTFSI system, Li^+ coordinates four ACN molecules, but it coordinates three ACN molecules and one thiocyanate ion in the LiSCN system (Figure 4.6). A similar molecular picture is deduced for the LiSCN/ACN system from the radial distribution function between Li^+ and the nitrogen atom of thiocyanate (Figure 4.6).

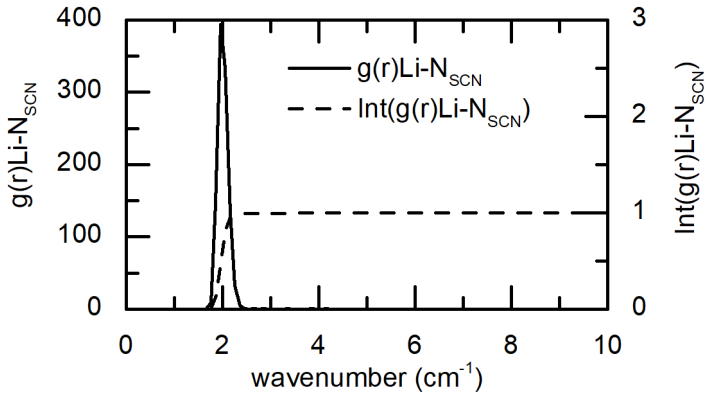

Figure 4.6. Radial distribution function between Li^+ and thiocyanate N ($g(r)Li\text{-}N_{SCN}$, solid line) and integral of g(r)Li-N ($Int(g(r)Li\text{-}N_{SCN})$, dash line) from ab initio MD simulation.

4.4.2. Vibrational coupling

The experiments performed here were designed with the objective of characterizing the molecular motions of the individual solvent molecules coordinating Li^+. Previous attempts on other solvents did not succeed because of the strong coupling among solvent molecules in the Li^+ solvation shell.[74, 77, 83] In contrast with previous systems, ACN has a small transition dipole

magnitude which is ~20 times smaller than dimethyl carbonate (Table 4.1). The small transition dipole for the CN stretch of ACN is directly observed when computing the vibrational spectrum of the complex $Li(ACN)_4^+$. In this case, the separation between the symmetric and asymmetric CN stretches is only ~2 cm^{-1} (Figure 4.5), demonstrating that the vibrational coupling constant is small ($\beta < 0.5$ cm^{-1}). Experimentally, this is confirmed by the FTIR and 2DIR spectra of the ACN/LiTFSI solution (Figure 4.1 and Figure 4.3) since only one peak is observed in the coordinated region in agreement with the symmetric and asymmetric CN stretches being very close to one another in frequency. In addition, the cross peaks due to vibrational coupling between coordinated and free ACN molecules are absent at all measured waiting times.

The lack of cross peak between coordinated and free peaks is in stark contrast with the observation in solutions of solvents containing carbonyl groups.[66, 72, 74, 77, 83] For example, the 2DIR spectra of solution of Li^+ in organic carbonates and ureas presented cross peaks between the asymmetric and symmetric carbonyl stretch modes in 2DIR spectra at $T_w = 0$ ps. Moreover, the characteristic time of vibrational energy transfer in carbonate/Li^+ or urea/Li^+ system is found to be on the order of several to tens of picosecond.[66, 74, 77, 83] However, in the case of ACN/Li^+ solutions, the cross peaks are not observed within the investigated window of $T_w = 3$ ps. The lack of cross peaks between coordinated and free peaks also demonstrates that the chemical exchange characteristic time is much slower than a few picoseconds, but it does not imply that the ACN molecules in the $Li(ACN)_4^+$ complex are not vibrationally coupled. On the contrary, the small vibrational coupling among ACN molecules makes the cross peak due to vibrational coupling between symmetric and asymmetric CN stretches to be located within the diagonal peak of the CN stretches of coordinated ACN molecules.

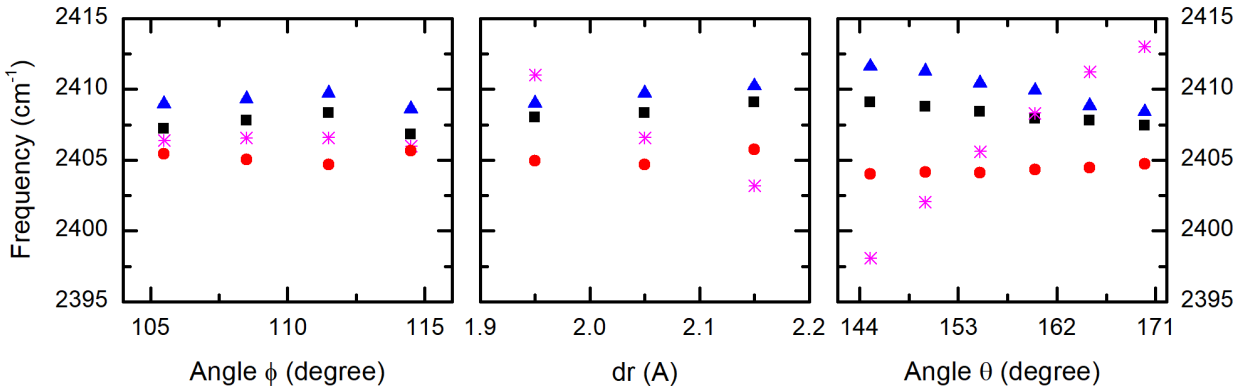

Figure 4.7. Frequency changes of the nitrile stretches computed by DFT as function of different geometrical factors: angle θ (left), distance dr (middle) and angle θ (right) in a solvation shell of $Li(ACN)4^+$. Magenta star, black square, red circle and blue triangle represent the calculated frequencies of the four coordinated nitriles of ACN. Note that only the geometrical factors for the nitrile group represented by the magenta star were varied in the calculation.

The weak vibrational coupling is also seen by computing distortions of Li^+ solvation shell. In this case, adjusting the distance (dr, N···Li^+) or the angles θ (C≡N···Li^+) and ϕ (O···Li^+···O) of one ACN within the $Li(ACN)_4^+$ complex does not significantly affect the CN frequencies of the other coordinated molecules (Figure 4.7). This result further supports our hypothesis that the coupling between coordinated CN groups is weak.

4.4.3. Dynamics of Li^+ solvation shell

The dynamics of the ACN molecules in the $Li(ACN)_4^+$ complex can be retrieved from the waiting time evolution of the coordinated peak shapes in the 2DIR spectra and represents the dynamics of frequency-frequency correlation function (FFCF). In any tetrahedral solvation shell, the Hamiltonian of the CN stretch can be described as:

$$H(t) = \begin{bmatrix} \omega_{10} + \delta\omega_1(t) & \beta_{12}(t) & \beta_{13}(t) & \beta_{14}(t) \\ \beta_{12}(t) & \omega_{10} + \delta\omega_2(t) & \beta_{23}(t) & \beta_{24}(t) \\ \beta_{13}(t) & \beta_{23}(t) & \omega_{10} + \delta\omega_3(t) & \beta_{34}(t) \\ \beta_{14}(t) & \beta_{24}(t) & \beta_{34}(t) & \omega_{10} + \delta\omega_4(t) \end{bmatrix} = \begin{bmatrix} \omega_{10}^{(1)}(t) & 0 & 0 & 0 \\ 0 & \omega_{10}^{(2)}(t) & 0 & 0 \\ 0 & 0 & \omega_{10}^{(3)}(t) & 0 \\ 0 & 0 & 0 & \omega_{10}^{(4)}(t) \end{bmatrix}$$

where ω_{10} is the transition frequency for each isolated CN stretch, $\delta\omega_i(t)$ describes the time-dependent change in frequency for the i^{th} CN stretch and $\beta_{ij}(t)$ defines the time-dependent

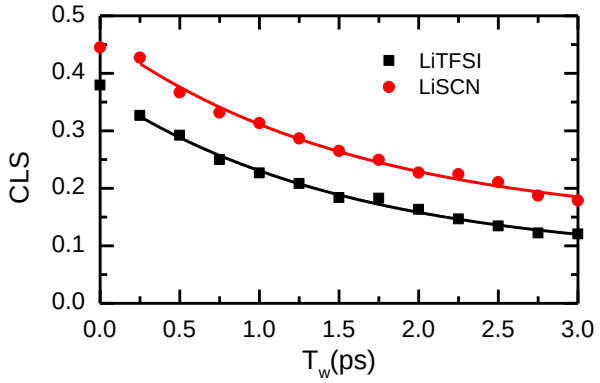

Figure 4.8. CLS of coordinated ACN in LiTFSI and LiSCN solutions with X(Li^+) = 0.05. Black and red represent the data of LiTFSI and LiSCN, respectively. The lines correspond to the model fitting as described in the text.

Table 4.3. Model parameters from the fitting of coordinated CLS in LiTFSI and LiSCN in ACN solutions.

Sample	τ (ps)	y_0	A
ACN/LiTFSI	1.6 ± 0.2	0.08 ± 0.01	0.29 ± 0.01
ACN/LiSCN	1.6 ± 0.2	0.13 ± 0.02	0.33 ± 0.01

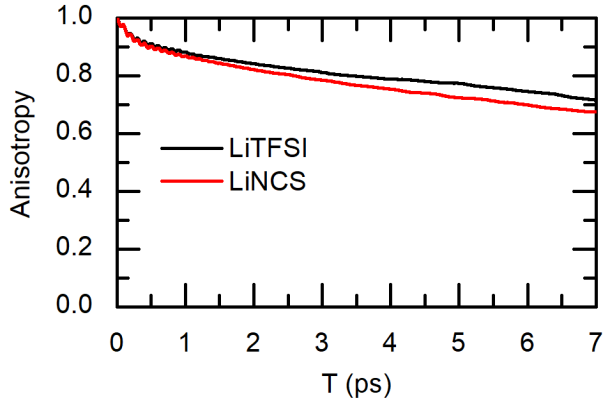

Figure 4.9. Anisotropy decay of the reorientations of coordinated ACN.

Table 4.4. Modeling of the reorientation dynamics (Figure 4.9) of the coordinated ACN in LiTFSI and LiSCN systems in the AIMDSs with an exponential decay of the form, $y = A_1 * e^{(-t/\tau_1)} + A_2 * e^{(-t/\tau_2)}$.

Parameters	LiTFSI in ACN	LiSCN in ACN
A_1	0.10 ± 0.01	0.10 ± 0.01
τ_1 (ps)	0.45 ± 0.01	0.41 ± 0.01
A_2	0.89 ± 0.01	0.89 ± 0.01
τ_2 (ps)	32.9 ± 0.1	24.3 ± 0.1

coupling between the i^{th} and j^{th} CN stretch. Using the previously demonstrated assumption that $\beta_{ij}(t)$ is negligible, the Hamiltonian reduces to a simple expression containing four degenerate frequencies ($\omega_{10}^{(j)}(t) = \omega_{10} + \delta\omega_j(t)$), where each randomly fluctuates according to its $\delta\omega_j(t)$. A similar Hamiltonian is deduced for the CIP, but only contains three sites. Thus, the characteristic time of FFCF directly relates to the fluctuation of the individual sites.

The spectral diffusion of ACN molecules coordinated to Li^+, computed using the center line slope (CLS)[241, 242], is shown in Figure 4.8. The CLSs of the coordinated CN stretches are well modelled with a single exponential decay of the form: $f(T_w) = A * e^{(-T_w/\tau)} + y_0$, where T_w is the waiting time, A is the amplitude, τ is the decorrelation time, and y_0 is an offset. The model parameters (Table 4.3) reveal that the ACN molecules undergo thermal frequency fluctuations in time scales smaller than 2 ps. Moreover, the presence of an offset (y_0) is also observed, which is indicative of the 2DIR peak containing more than one underlying transition that exchanges with a slow characteristic time. For example, the CLS offset in LiTFSI sample could be attributed to the presence of multiple transitions and/or solvent separated ion pairs. While the former case refers to the presence of the four/three CN stretches within the same band,[243] the latter case produces an offset since it is expected that the making and breaking of solvent separated ion pairs occur with a much longer characteristic time.[214] A curious finding is that the CLS of the coordinated CN stretch has very similar value of the spectral diffusion time (τ = 1.6 ps) for both samples even though Li^+ form totally different solvation shells corresponding to a free ion and CIP, as previously described. In other words, the motions of the ACN coordinating Li^+ appear to be very similar even in the presence of an anion in the Li^+ solvation shell. It should be noted that the CLS dynamics of the coordinated ACN molecules only accounts for site frequency fluctuation and not their reorientations[244] since $Li(ACN)_4^+$ complex has a large

molecular size (148 cm^3/mol) compared to a single ACN molecule (38 cm^3/mol). This is in agreement with the reorientation dynamics of 33 ps and 24 ps for a single coordinated ACN (Figure 4.9 and Table 4.4) computed from the AIMDSs for $Li(ACN)_4^+$ and $Li(ACN)_3(SCN)$, respectively. Thus, the fast dynamics seen in CLS of the coordinated peak describes exclusively the thermal motions of the ACN molecules coordinated to Li^+.

4.4.4. Molecular mechanism of FFCF

The molecular mechanism giving rise to the FFCF dynamics was studied using the AIMDSs. Given the simplicity of the Li^+ solvation shells for the free ion and CIP, it is possible to model the effect of the solvation shell with three structural parameters: the $N\cdots Li^+$ distance, the $N\cdots Li^+\cdots N$ angle and the $C{\equiv}N\cdots Li^+$ angle. In the case of ACN, each coordinated ACN molecule in the $Li(ACN)_4^+$ complex undergoes fluctuations of its CN stretch independently of the others due to the weak vibrational coupling between coordinated ACN nitrile stretches. Moreover, the weak coupling makes the frequency of coordinated ACN nitrile stretches to fluctuate slightly when $N\cdots Li^+\cdots N$ angle is changed (Figure 4.7). The lack of change of the CN stretch frequencies with this geometrical factor is in agreement with the single site representation in which changes in the distance and angle between the nitrile group of ACN and Li^+ drive the large frequency fluctuations in the CN stretch. Thus, the modeling of the CN stretch coordinated to Li^+ reduces to two structural factors: the $N\cdots Li^+$ distance and the $C{\equiv}N\cdots Li^+$ angle. Interestingly, the autocorrelation function of these two geometrical factors reveals dynamics with characteristic times in the range of 1-2 ps (Table 4.5), which are both very close to the experimental values of the FFCF. Thus, the dynamics of the structural factors alone does not show to what degree each geometrical factor contributes to the FFCF. To this end, a frequency map of CN stretch was built.

Table 4.5. Modelling of correlation functions of dr or angle θ in LiTFSI and LiSCN systems in the AIMDSs (Figure 4.10) with a single exponential decay of the form, $y = A_1 * e^{(-t/\tau_1)}$.

Geometrical Factor	Parameters	LiTFSI in ACN-d3	LiSCN in ACN-d3
dr	A_1	0.0030 ± 0.0001	0.0011 ± 0.0001
	τ_1 (ps)	1.42 ± 0.01	1.12 ± 0.02
θ	A_1	108.3 ± 0.6	139.2 ± 0.4
	τ_1 (ps)	0.96 ± 0.01	1.70 ± 0.01

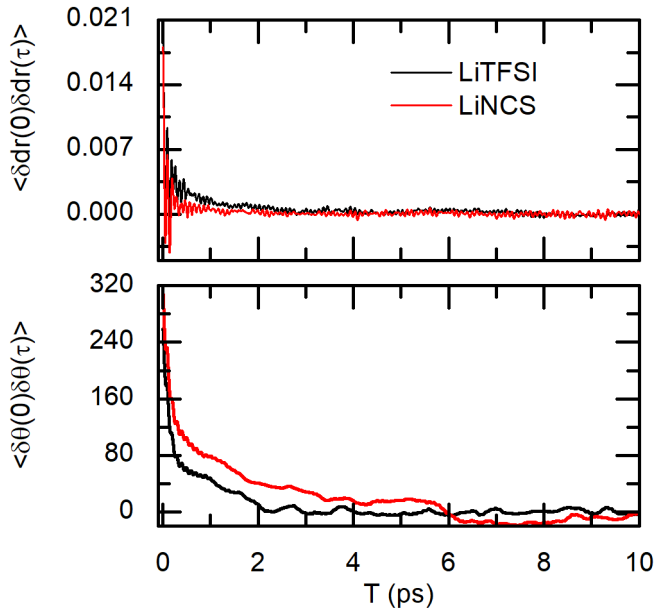

Figure 4.10. Correlation functions of distance dr (top) or angle θ (bottom) in LiTFSI (black) and LiSCN (red) solutions, calculated from AIMD simulations.

The new-built frequency map (Figure 4.11) reflects the effect on the CN stretch frequency of single ACN in the $Li(ACN)_4^+$ or $Li(ACN)_3(SCN)$ complex for the distance dr ($N\cdots Li^+$) and the angle θ ($C{\equiv}N\cdots Li^+$). It is also observed that the frequency fluctuations due to changes in the angle θ are not significantly affected by the changes in the distance dr and vice versa (Figure 4.12). This indicates that frequency changes can be described in first approximation by two independent fluctuation terms as:

$$\omega_{01}(t) = \omega_{01}^{opt} + \delta\omega_\theta(t) + \delta\omega_r(t)$$

where $\delta\omega_\theta$ and $\delta\omega_r$ are the fluctuations of the frequency due to changes in the angle θ and distance dr, respectively. Using the DFT map and the coordinates from the AIMDSs, the instantaneous frequencies were calculated for the ACN in the Li^+ solvation of the ACN/LiTFSI and ACN/LiSCN systems.

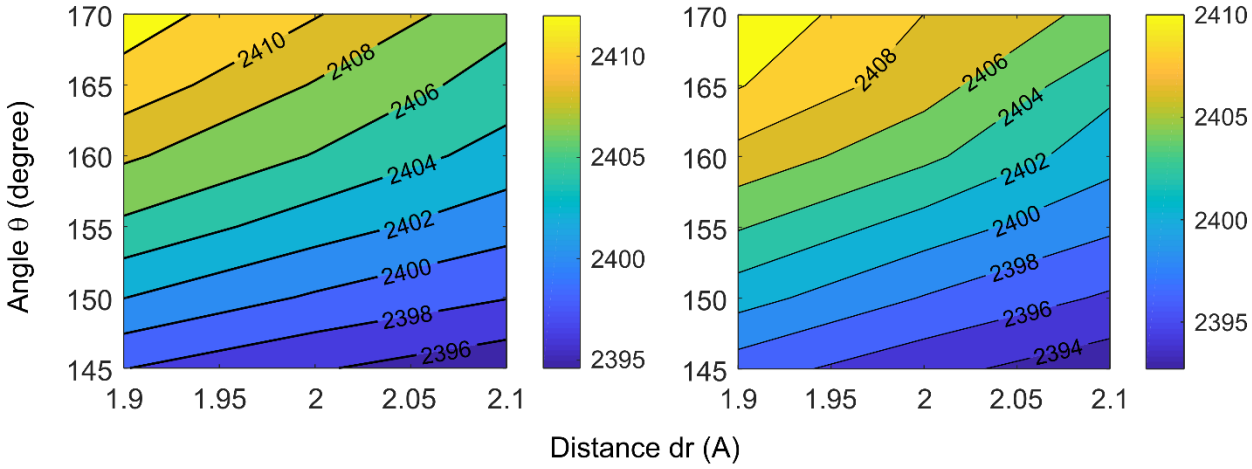

Figure 4.11. Frequency map as contour plots of the nitrile stretch of acetonitrile from DFT computations of solvated tetrahedral solvation shell (left) and solvated contact ion pair with thiocyanate ion (right). X axis: distance dr in Å. Y axis: angle θ in degree. Each contour line is marked with the corresponding frequency in cm^{-1}.

The $\delta\omega_\theta$ as a function of θ and $\delta\omega_r$ as a function of dr were obtained from the fitting of the data in Figure 4.12. As a result for the ACN/LiTFSI system and using that $\omega_{01}^{opt} = 2406.57$ cm^{-1}, the following equation were obtained:

$$\delta\omega_\theta(cm^{-1}) = -0.0089 * \theta^2 + 3.3486 * \theta - 308.9300,$$

$$\delta\omega_r(cm^{-1}) = -24.9417 * r + 51.2219,$$

$$\omega_{01}(cm^{-1}) = 2148.8619 - 0.0089 * \theta^2 + 3.3486 * \theta - 24.9417 * r.$$

Similarly for the ACN/LiSCN system where $\omega_{01}^{opt} = 2397.30$ cm^{-1}, the following equation were obtained:

$$\delta\omega_\theta(cm^{-1}) = -0.0077 * \theta^2 + 2.9652 * \theta - 271.6233,$$

$$\delta\omega_r(cm^{-1}) = -22.2312 * r + 45.6975,$$

$$\omega_{01}(cm^{-1}) = 2171.3742 - 0.0077 * \theta^2 + 2.9652 * \theta - 22.2312 * r.$$

These sets of equations were used to obtain the instantaneous frequencies from the AIMDSs.

The theoretical FFCF derived from the instantaneous frequencies shows an ultrafast decay in agreement with the fast fluctuations seen for the angle θ and distance dr (Figure 4.13). The theoretical FFCF modeled with a single exponential decay (Table 4.6) has characteristic times of 1-2 ps for the CN stretches in $Li(ACN)_4^+$ and $Li(ACN)_3(SCN)$. These time scales are in good agreement with their experimental counterpart of 1.6 ± 0.2 ps. In addition, the computed FFCF reveals the presence of another ultrafast component (~0.1 ps), but it is likely that this component only contributes as homogeneous component in the FFCF and it is not measured experimentally.[242, 245] To compute the influence of the dr and θ geometrical factors on the FFCF, the frequency autocorrelation function was computed for each individual geometrical factors

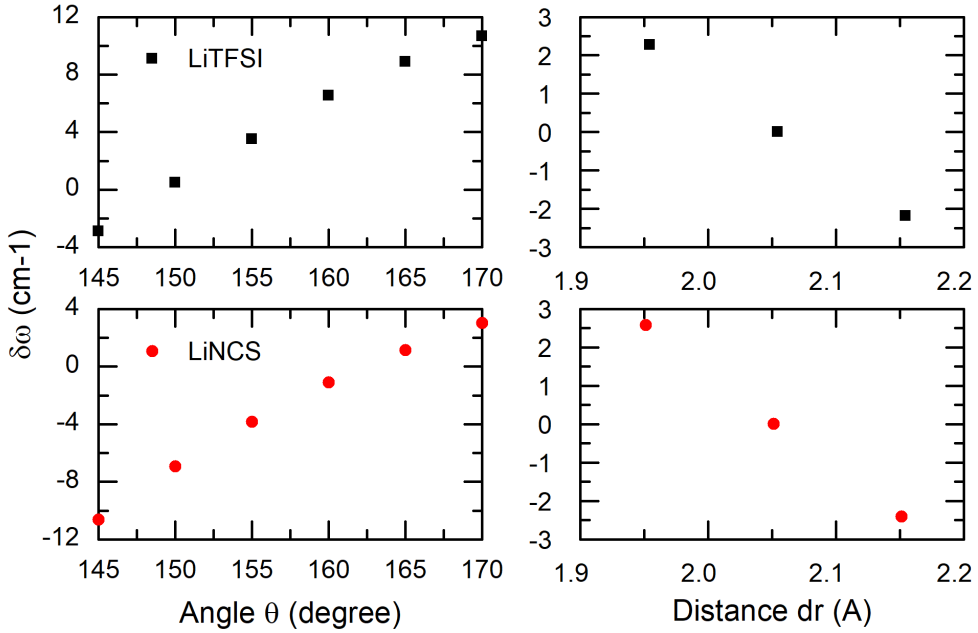

Figure 4.12. Frequency fluctuations (δω) due to the change of θ (left) or dr (right) in the tetrahedral solvation shell (upper) and contact ion pair with SCN- (lower).

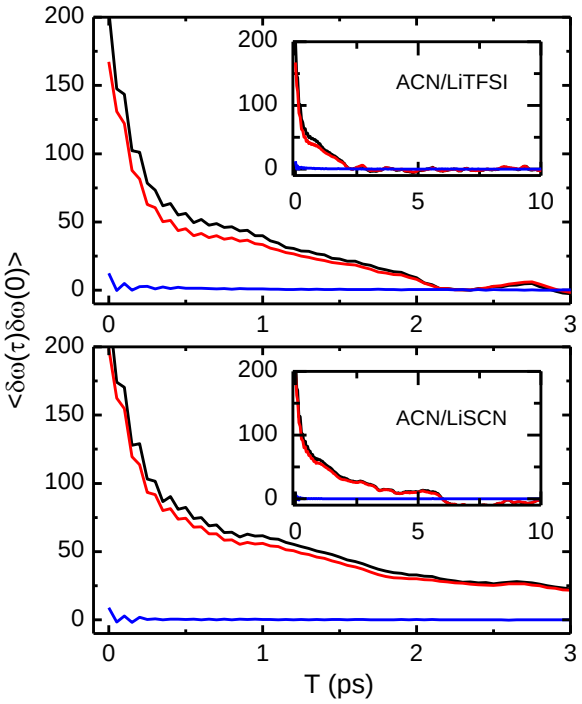

Figure 4.13. FFCFs computed from the AIMDS for the ACN/LiTFSI (top panel) and ACN/LiSCN (bottom panel) systems. Insets show the FFCFs for 10 ps windows. Black, red and blue lines represent the FFCF containing both dr and θ, only θ, or only dr, respectively.

Table 4.6. Parameters from fitting the autocorrelation functions of both dr and θ, only θ or only dr in ACN/LiTFSI and ACN/LiSCN systems.

Type	Fitting Parameters	ACN/LiTFSI	ACN/LiSCN
Both dr&θ	*A'*	104 ± 4	109 ± 2
	τ' (ps)	0.88 ± 0.03	1.70 ± 0.04
Only θ	*A'*	82 ± 3	99 ± 2
	τ' (ps)	0.92 ± 0.04	1.72 ± 0.04
Only dr	*A'*	1.9 ± 0.1	0.65 ± 0.05
	τ' (ps)	1.44 ± 0.08	0.94 ± 0.08

(angle θ and distance dr). The FFCFs for the individual components (Figure 4.13) reveal the same decorrelation times of 1-2 ps. However, it is evident that for both ACN/LiTFSI and ACN/LiSCN systems, the frequency of single ACN nitrile stretch is dominated by the fluctuations in the angle θ since the fluctuations of distance dr have a much smaller amplitude (variance) as compared to those of the angle θ or to the total amplitude of the frequency

fluctuation (Figure 4.13). The result is also in line with the effect of individual motions of ACN molecules in the solvation shell of Li^+, where only the angle θ has a strong effect on the frequency of ACN nitrile stretch (Figure 4.12). In addition, the strong interaction between Li^+ and the CN group, as seen by the presence of sharp peaks in the radial distribution functions (Figure 4.5), is likely to restrict the fluctuations of the distance dr as compared to the angle θ, which explains the small effect of dr in the FFCF. Overall, the results demonstrate that angles play a significant role in the frequency fluctuations of coordinated nitriles, and is similar to what was previously reported in carbonate-based electrolytes, where it was postulated that the angles within the first solvation shell of Li^+ are key for describing the FFCF of the coordinated carbonyl groups.[74, 81]

4.5. Summary

The present study investigated the dynamics of the acetonitrile molecules in first solvation shell of Li^+ and unveiled the underlying molecular mechanism of such dynamics by a combination of experimental and theoretical methodologies. The results showed that $Li(ACN)_4^+$ and $Li(ACN)_3(SCN)$ are formed in ACN/LiTFSI and ACN/LiSCN systems, respectively. In addition, it is observed that the ACN molecules solvating Li^+ are vibrational weakly coupled. Thus, FFCF of coordinated CN stretch extracted from 2DIR experiments and the AIMDSs revealed that the in-place motions of the individual ACN molecules in Li^+ first solvation shell have a characteristic time of ~1.6 ps irrespective of the speciation of Li^+. The experimental FFCF was found to be in good agreement with the theoretical FFCF derived from the AIMDSs and the DFT frequency maps. In addition, analysis of effect of the two geometrical factors, the distance dr and the angle θ, in FFCF indicated that the angle θ is the dominating factor of the FFCF

dynamics while the contribution of the distance dr is found to be negligible. The findings of this work are in line with previous modeling of the solvation shell motions of Li^+.

CHAPTER 5. THE MOLECULAR ORIGIN OF MACROSCOPIC PROPERTIES IN CONCENTRATED LITHIUM ION ELECTROLYTES

Highly concentrated or "solvent-in-salt" electrolytes are an emerging type of lithium ion electrolytes in past few years. In this type of electrolytes, the concentration of Li salt is ~4 M, meaning the molar ratio of salt:solvent is ~1:2. Since there is few free solvent molecules, ion pairs instead of free ion solvation shell, become dominant in the speciation of Li+. In the literature, concentrated electrolytes have been studied extensively regarding the macroscopic properties, e.g. conductivity, viscosity, capacity and cyclability. However, a detailed picture at the microscopic level needs to be resolved in order to obtain a better understanding of the macroscopic properties of concentrated electrolytes. In this work, the highly concentrated electrolytes are studied at the molecular level by linear and non-linear infrared spectroscopies, with the assistance of DFT computations and ab initio molecular dynamics simulations. To investigate the molecular environment of concentrated electrolytes, a family of lithium salts with increasing anion size is used to prepare concentrated electrolytes in acetonitrile. A strong correlation is observed between nearby Li+, indicating a high correlation between nearby first solvation shells. Further analysis reveals the fully correlated dynamics inside and outside the first solvation shells of Li+, which supports the formation of a highly correlated network in concentrated electrolytes. A direct relation between the molecular motions and the macroscopic properties is observed as well, which again supports the proposed model of highly correlated networks. Overall, this study gains better understanding of the concentrated electrolytes at the molecular level, and reveals the molecular origin of macroscopic properties in a family of concentrated lithium ion electrolytes.

5.1. Introduction

Lithium ion batteries (LIB) have become one essential part of the energy storage techniques in last several decades. As a type of rechargeable batteries, LIB have been used universally in mobile phones[25, 246], household electric equipment[25, 247], and some larger-scale power tools like mowing machines[248, 249] and electric vehicles[24, 26]. LIB are known to be superior to other types of batteries due to the advantages of high power output, high energy density, high coulombic efficiency and stable cycling performance.[22, 250-252] However, LIB have some major issues regarding the safety, toxicity, cost and degradation, making the advancement of the battery more and more demanding.[3, 24, 253-256] In the state-of-the-art literature of LIB, most researches focused on making adjustments on the components of the batteries, e.g. electrodes[257, 258], electrolytes[259, 260] or electrolyte additives[261-263], while only a few investigated the molecular structure and motions in the electrolytes[66, 71, 77, 81, 264]. In order to develop LIB with better performance, a detailed picture of the electrolytes at the molecular level needs to be resolved.

Typical lithium ion electrolytes (LIE) are composed of lithium salts and organic solvent.[5, 14] Commercially used electrolytes are prepared by dissolving ~1 M lithium hexafluorophosphate ($LiPF_6$) in a mixture of cyclic and linear carbonates, usually a mixture of ethylene carbonate (EC) and dimethyl carbonate (DMC).[5, 14] Lithium ion (Li+) is known to have a tetrahedral solvation shell exclusively formed by solvent molecules in ~1 M Li+ solutions.[67, 77, 169, 239, 265] It is also known that the conduction mechanism of dilute LIE is the vehicular transport of Li+ first solvation shell. Though commercial LIE have the optimal performance for batteries, they have some problems that are yet to be solved. For instance, the cycling stability of the electrodes are not fulfilled in the dilute electrolyte (~1 M Li+).[4, 266] The electrodes at the solid-electrolyte interface (SEI) reacts with the dilute electrolytes during charging and discharging processes. The

repetitive destruction/construction of SEI will lead to formation of Li dendrites on the surface of electrodes, and therefore, cause capacity fade.[2, 70] One possible solution for this issue is to develop highly concentrated electrolytes.[10, 191]

Highly concentrated electrolyte (HCE) is prepared by dissolving ~4 M Li salt in organic solvents. At this concentration, the molar ratio of Li:solvent is ~1:2, meaning that each Li+ is coordinated by a maximum of two solvent molecules in the first solvation shell. Thus, the anions have to join the first solvation shell to fulfill the coordination number of four.[10, 101, 237] HCE is found to have few free solvent molecules in the solution, which eliminates the solvent intercalation into the electrode and enables the successful cycle of Li intercalation/deintercalation on the surface of electrode.[267, 268] HCE is also determined to have high chemical stability, high cyclability and enhanced safety.[10, 191] Mandai et al. investigated the structure and properties of concentrated mixtures of salts and solvents.[269] It is claimed that certain concentrated mixtures of Li salt and ligand molecules are not simply "solutions" anymore, but may be described as "ionic liquids". In addition, the thermal and electrochemical stability of the mixtures are observed to gradually improve with increasing concentration of Li+.[269] It is also claimed by other research groups that the remarkable performance of the concentrated electrolyte arises from the formation of a fluid polymeric network of the anions and Li+ cations.[10, 98] In the literature, macroscopic properties of HCE have been investigated by many researchers[99, 191, 270-272], while the study of molecular origin of those properties is scarce[10, 98, 101, 237, 273]. In order to gain a better understanding of the macroscopic properties of HCE, more insights should be put into the molecular environment in the electrolytes.

A previous study by our group has obtained more information about the structure and dynamics of Li+ first solvation shell in the concentrated mixtures of Li salts and carbonate

molecules.[101] Three configurations of the first solvation shell around Li+ were derived, where the sulfonylimide anions can coordinate Li+ in either monodentate or bidentate configuration. In addition, the coordination/decoordination of solvent molecules from a Li+ solvation shell is observed on a picosecond time scale. The process of solvent exchange is found to be correlated to the making and breaking of coordination bonds between the cation and anion in the same solvation shell. The making and breaking of coordination bonds initiate the ion transport from one solvation shell to another, which is determined to be the conduction mechanism in HCE. Though carbonate molecules are good infrared probes for studying the structural and dynamical changes in solutions, the excitonic nature or strong vibrational coupling of carbonyl stretches made the interpretation of infrared spectra very demanding. To enable the investigation of individual solvent molecules, a non-excitonic solvent, acetonitrile, is selected and found to be a good reporter for the environment around Li+ centers.[85] Additionally, the spectral features and motions of acetonitrile molecules in Li+ first solvation shell were well studied in previous research.[85] Thus, acetonitrile should be a good reporter for the structure of solvation shell and the dynamics of individual solvent molecules in HCE.

In this study, a family of lithium salts where the size of fluorinated anion increases systematically, was selected to investigate the molecular interactions in the concentrated solutions of acetonitrile (ACN). The selected lithium salts are lithium bis(fluorosulfonyl)imide (LiFSI), lithium bis(trifluoromethanesulfonyl)imide (LiTFSI) and lithium bis(pentafluoroethanesulfonyl)imide (LiBETI), the chemical structures of which are shown in Scheme 5.1. This family of lithium salts has large counter-ions with highly delocalized negative charges, which facilitates the dissolution of Li salts in organic solvents. It is worth noting that the sulfonylimide anion cannot be directly measured by infrared spectroscopies due to the highly

convoluted peaks in the low frequency region. Thus, the environment around the Li+ centers were investigated through the CN stretch of ACN molecules. For these purposes, linear (FTIR) and two-dimensional infrared (2DIR) spectroscopies as well as DFT calculations and ab initio molecular dynamics simulation (AIMDS) were utilized. From IR spectra, the structure and dynamics of Li+ first solvation shell can be investigated. AIMDS will be used to interpret the experimental results by providing detailed information about the local structures and molecular motions in the HCE formed by lithium sulfonylimide salts.

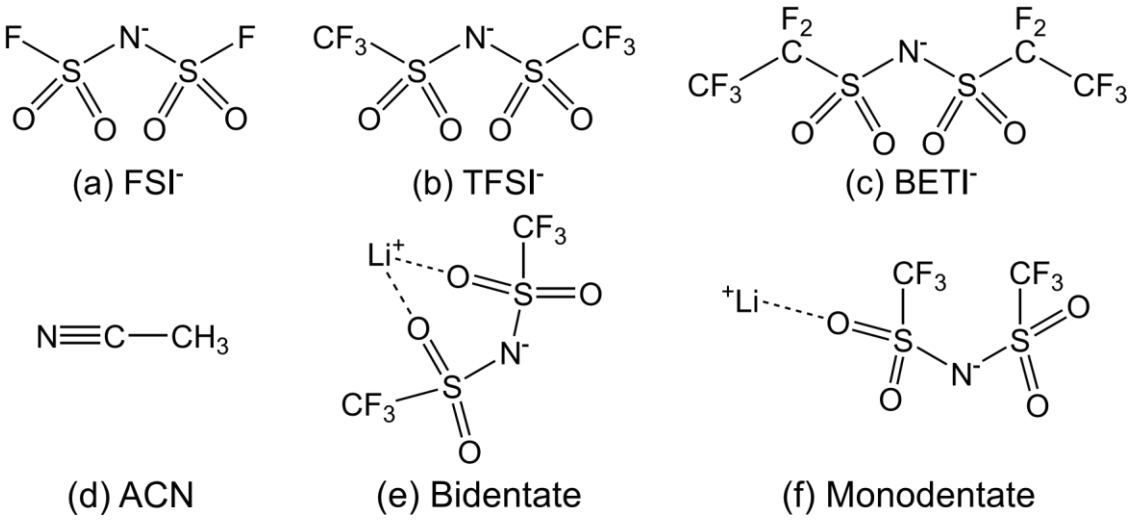

Scheme 5.1. Structures of sulfonylimide anions, solvent molecule and two coordination configurations of $TFSI^-$. (a) bis(fluorosulfonyl)imide (FSI^-), (b) bis(trifluoromethanesulfonyl)imide ($TFSI^-$), (c) bis(pentafluoroethanesulfonyl)imide ($BETI^-$), (d) acetonitrile (ACN), (e) bidentate and (f) monodentate configurations of TFSI- coordinating Li^+.

5.2. Methods

5.2.1. Solution preparation

LiFSI (98% TCI) was used without purification. LiTFSI (98% Alfa Aesar) and LiBETI (98% TCI) were dried in a vacuum oven under 150 ℃ for two days. Acetonitrile-D3 (ACN-D3, 99.8% isotope VWR) was dried in molecular sieves overnight before use. The usage of ACN-D3 instead of ACN is to eliminate the combination band in the nitrile stretching region of infrared

spectrum.[85, 210] In the manuscript, ACN refers to ACN-D3 in the results and discussion of the experiments.

Solutions of LiFSI, LiTFSI or LiBETI in ACN-D3 were prepared at the salt:solvent molar ratio of 1:2. To assist the dissolution of Li salt in ACN-D3, the mixture of salt and solvent was heated at low level on a hot plate until a clear, homogeneous liquid formed. Sample cells for FTIR and 2DIR consisted of the ACN-D3/Li+ solution sandwiched between two CaF_2 windows without spacer. All samples and sample cells were prepared in a N_2-filled glovebox to minimize water contamination from the air. The solvent was tested for less than 100 ppm of water by Karl Fischer titration.

5.2.2. Ionic conductivity and viscosity measurements

The ionic conductivity of the electrolytes was measured using a YSI 3200 conductivity meter combined with YSI 3250 cell probe. The temperature of the solutions was recorded with the integrated temperature probe of the cell probe. The viscosity of the electrolytes was measured using a Brookfield DV-II+pro viscometer.

5.2.3. Fourier transform infrared spectroscopy (FTIR)

FTIR experiments were performed on a Bruker Tensor 27 equipped with a liquid nitrogen cooled MCT detector with a spectral resolution of 0.5 cm^{-1}. Reported spectra were averaged over 40 scans. FTIR data were modeled using OriginLab software.

5.2.4. Two-dimensional infrared spectroscopy (2DIR)

The setup used for 2DIR experiments has been previously detailed in the literature, so only a short description is provided here.[107, 150] The input IR pulses were generated with a Spectra Physics Spitfire Ace Ti:sapphire amplifier at a repetition rate of 5 kHz, in combination with an OPA-800C and difference frequency generation crystal. These input IR pulses were then

split into three replicas and later focused on the sample using the well-known boxcars geometry.[215] The photon echo signal was measured in the $-k_1 + k_2 + k_3$ phase-matching direction. A heterodyned detection was performed using a fourth pulse (local oscillator). The heterodyned signal was measured in a 64-element MCT array detector after dispersing the heterodyned signal in a spectrometer. The photon echo signal was measured as a function of three critical time intervals: the coherence time τ (interval between pulses 1 and 2), the waiting time T_w (interval between pulses 2 and 3), and the coherence time t (interval between pulse 3 and the detected signal). These time intervals were set via computer-controlled translation stages. Here, 2DIR data were collected by scanning τ time from −4 to +4 ps in increments of 5 fs for each waiting time to collect both the rephasing and nonrephasing data by switching the time ordering.[180] Signals were collected for waiting times from 0 to 5 ps in steps of 0.25 ps. The data collection in waiting time was confined to a maximum of 5 ps due to the presence of heating effects.[92, 216, 217] In all of the measurements, the local oscillator always preceded the photon echo signal by ∼0.8 ps. The time domain signal, collected as a function of (τ, T_w, λ_t) via a monochromator-array detection, is transformed into the 2DIR spectra (ω_τ, T_w, ω_t) by means of Fourier transforms. A detailed explanation of the Fourier analysis has been described elsewhere.[218]

5.2.5. Ab initio molecular dynamics simulations (AIMDS)

The AIMDSs were carried out with the CP2K package (version 3.0).[219] The electronic structure was calculated via Quickstep module[219] using the PBE functional with the D2[220] dispersion scheme and the TZV2P basis set, with Goedecker-Teler-Hutter (GTH) pseudopotentials.[221-223] Periodic boundary conditions were applied to the system, and the Nosé-Hoover thermostat was used to keep the temperature constant at 300 K, with the temperature

damping constant of 100 fs. A self-consistent field (SCF) convergence criterion was set to 5.0 × 10^{-7} hartree. The ACN/LiTFSI system was composed of 10 lithium ions (Li+), 10 bis(trifluoromethanesulfonyl)imide ions ($TFSI^-$) and 20 acetonitrile-t3 (ACN-T3) in a cubic box with a length of ~15.9 Å. The ACN-T3 (i.e., all hydrogens (H) were replaced by tritium (T)) is required for 1.0 fs time steps in the AIMDS.[171, 225] In this paper, the box composition is representative of concentrated lithium electrolyte in acetonitrile with a molar ratio between salt and solvent of 1:2.

The initial lithium solvation shell of LiTFSI in ACN-T3, consisting of a Li+ coordinated to 2 acetonitrile molecules and 1 $TFSI^-$ in a bidentate configuration (Scheme 5.1), was first optimized to reach the minimum energy by Gaussian 09.[227] The molecular box contains 10 optimized solvation shells randomly placed using Packmol.[228] The box later underwent a minimization run over 5000 cycles, a 2 ns NVT and 2 ns NPT process using AMBER software package and GAFF force field.[229, 230] These preparation steps were required to assure the equilibration of the box. In the AIMDS, the system was equilibrated for ~20 ps, followed by a production run in the NVT ensemble for another ~100 ps.

5.2.6. DFT calculations

DFT calculations were performed with Gaussian 09 software at the PBE1PBE level of theory using the 6-311++G** basis set.[227] Structure optimization, frequency calculations and natural bond orbital (NBO) analysis were performed in acetonitrile using polarizable continuum model (PCM) in order to obtain reasonable structures of the contact ion pairs.

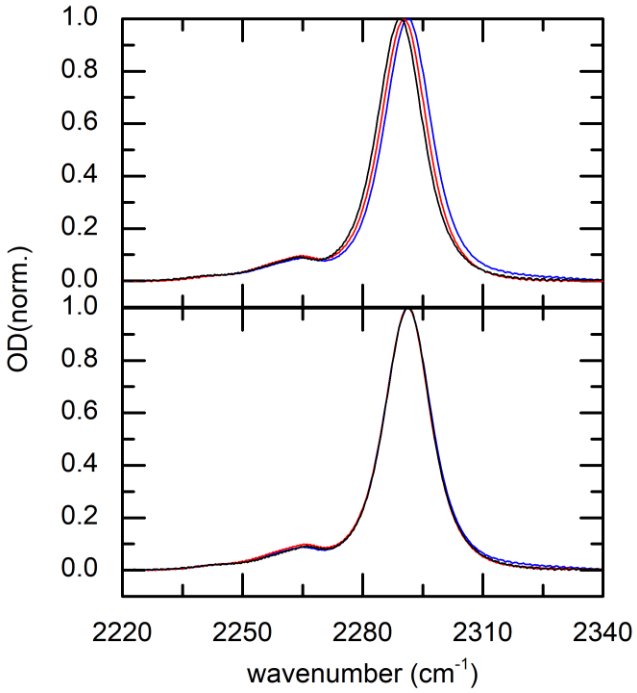

Figure 5.1. Normalized FTIR spectra (upper) and normalized FTIR spectra after overlapping the maxima of peaks (lower). The results of LiFSI, LiTFSI and LiBETI in ACN are represented by black, red and cyan, respectively. The salt:solvent molar ratio is 1:2. Details of the figure are illustrated in the text.

5.3. Results

The concentrated solutions of Li salts and ACN were studied by linear infrared (IR) spectroscopy. The concentration-dependent FTIR spectra in the nitrile (CN) stretching region for the solvent (2220 cm^{-1}–2340 cm^{-1}) are shown in Figure 5.1. From previous research, it is known that pure ACN shows one asymmetric band at ~2265 cm^{-1} corresponding to the free CN stretch.[85] This band is asymmetric due to the overlap of hot band transitions.[207] In dilute ACN electrolytes, the frequency of the CN stretch blue shifts due to the interaction with Li+, giving rise to a second band at ~ 2285 cm^{-1}.[79, 85] Similar bands are also observed in the FTIR spectra of concentrated electrolytes. The low- and high-frequency bands in the CN stretching region are assigned as free and coordinated bands of CN stretch, respectively. It is observed that the intensity of the

coordinated band is much higher than the free band. The central frequency of coordinated band blue shifts by ~2 cm^{-1} from LiFSI to LiBETI sample. In addition, the normalized spectra of three different salts have similar bandwidth. Even after overlapping the maximum of coordinated bands, the difference in bandwidth among three Li salts in ACN at the molar ratio of 1:2 is negligible. (Figure 5.1)

2DIR spectroscopy is known to have high spectral resolution and time resolution. In order to investigate the molecular environment in concentrated electrolytes, the 2DIR spectra were collected for LiFSI, LiTFSI or LiBETI in ACN at the molar ratio of 1:2, as shown in Figure 5.2. The 2DIR spectra among three salts have similar spectral features. In the CN stretching region of each spectrum, one pair of major peaks can be observed along the diagonal, corresponding to the coordinated bands in the FTIR spectra. The red and blue peaks correspond to the vibrational transitions from υ=0 to υ=1 and from υ=1 to υ=2, respectively. The pair of coordinated peaks is located approximately at (ω_τ, ω_t) = (2290 cm^{-1}, 2295 cm^{-1}) and (2290 cm^{-1}, 2270 cm^{-1}). It is worth noting that the free bands in FTIR spectra still appear in the 2DIR spectra on the low-frequency side at around (ω_τ, ω_t) = (2265 cm^{-1}, 2265 cm^{-1}). However, because the amplitude of the transition dipole moment of the coordinated CN stretch (~130 km/mol) is twice as much as the free CN stretch (~60 km/mol) (Table 5.1), the resulted free peaks in 2DIR spectra have very small intensity as compared to the coordinated peaks, and thus, are hardly seen. (Figure 5.2) At short waiting time, the peaks are elongated along the diagonal line that is represented by the solid black line. When time progresses, the shape of the peaks become rounder and more upright, which indicates the process of spectral diffusion. At waiting time of 5 ps, heating effect causes the peaks to get wider along the axis of probe frequency.

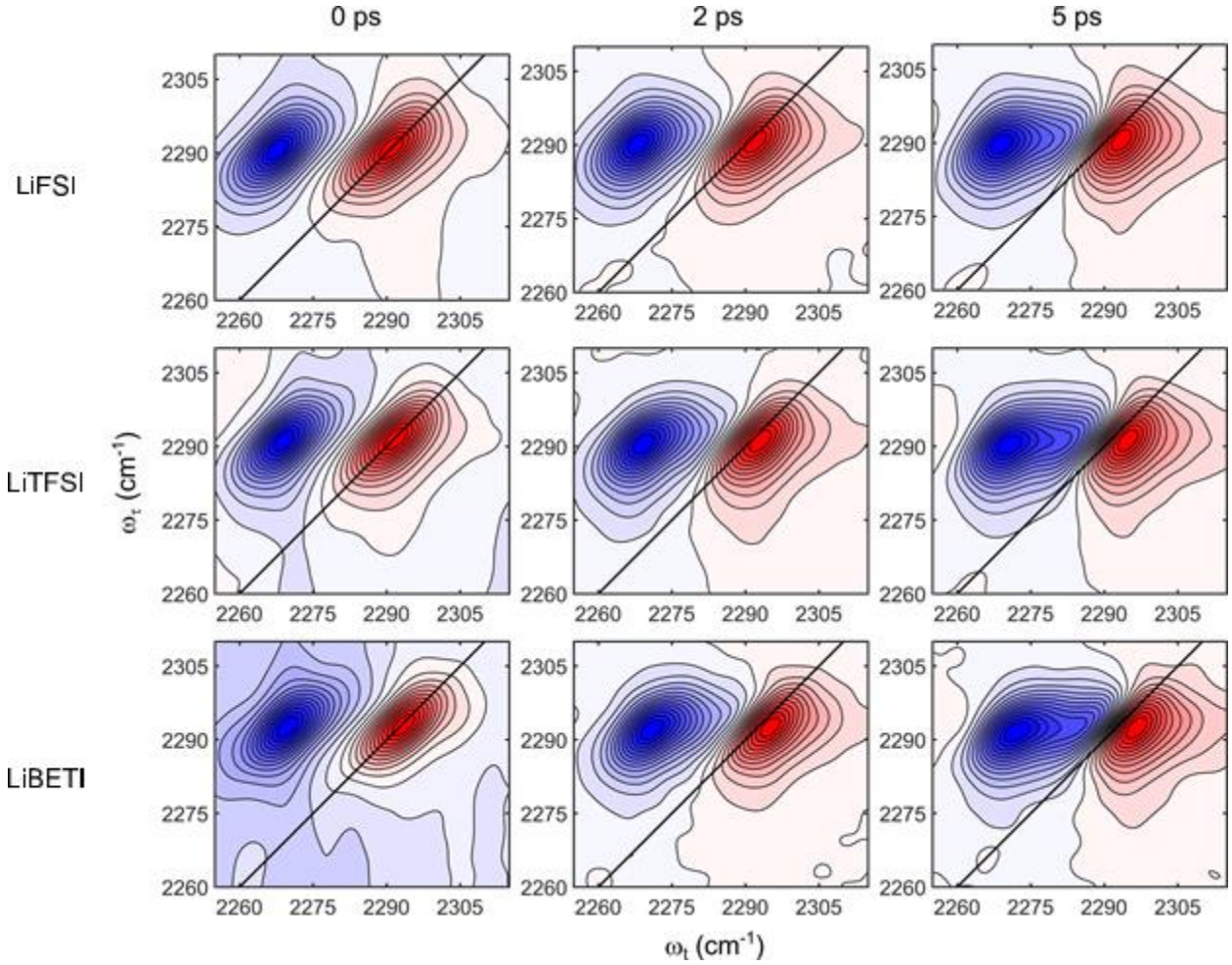

Figure 5.2. 2DIR spectra of Li salts in ACN at the molar ratio of 1:2. LiFSI, LiTFSI and LiBETI are shown in the upper, middle and lower panels, respectively. The waiting times shown from left to right are 0, 2 and 5 ps. The x-axis is probe frequency (ω_t cm^{-1}) while the y-axis is pump frequency (ω_τ cm^{-1}).

Table 5.1. Frequency calculations of bidentate solvation shells formed by three Li salts. The frequency (ω_{CN}) and intensity (I) of coordinated CN stretch are reported in cm^{-1} and km/mol, respectively.

Species	ω_{CN} (cm^{-1})	I (km/mol)
Li(ACN)$_2$(FSI)	2403.66	73.19
	2404.05	214.89
Li(ACN)$_2$(TFSI)	2403.83	210.98
	2404.01	69.01
Li(ACN)$_2$(BETI)	2403.03	172.43
	2403.44	95.90
ACN	2378.15	62.15

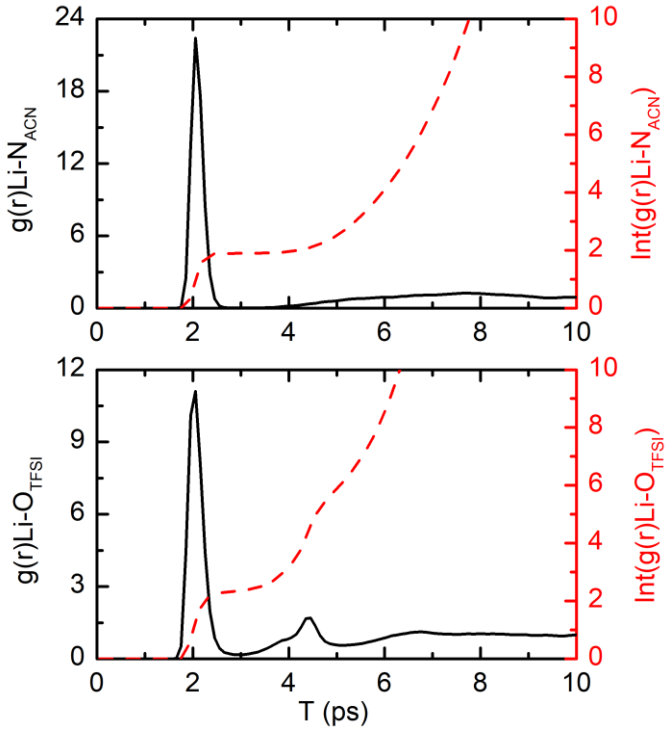

Figure 5.3. Radial distribution functions (g(r)) and the integrated radial distribution functions (Int(g(r))) between Li and coordinated atoms. The g(r)Li-N_{ACN} and Int(g(r)Li-N_{ACN}) between Li and the N of ACN are shown in the upper panel. The g(r)Li-O_{TFSI} and Int(g(r)Li-O_{TFSI}) between Li and the O of TFSI- are shown in the lower panel.

5.4. Discussion

It is known that Li+ forms four coordination bonds with either solvent or anion in the first solvation shell.[10, 101, 237] When the molar ratio of salt:solvent is around 1:2, most of the solvent molecules are coordinated, as supported by the high intensity of coordinated bands and the low intensity of free bands in IR spectra. (Figure 5.1 and Figure 5.2) Fitting the FTIR spectrum reveals the areas of coordinated and free bands. Combining the band areas, Lambert-Beer Law, and the transition dipole amplitudes of CN stretches, the percentage of free ACN is determined to be ~8% at the salt:solvent molar ratio of 1:2.

A comparison of FTIR data with AIMDS of the ACN/LiTFSI system at the salt:solvent molar ratio of 1:2 provides detailed information about the solvation shell of Li+. The radial

distribution functions (g(r)) between Li+ and the coordinated atoms are shown in Figure 5.3. It is indicated that the coordination number of N_{ACN} is 1.89 at the cutoff distance of 2.95 Å, while the coordination number of O_{TFSI} is 2.35 at the cutoff distance of 2.95 Å. It is also shown that O_{TFSI} atoms form more coordination bonds than N_{ACN} atoms. Because the number of coordinated ACN per Li+ is lower than 2, there is a small amount of free solvent molecules in the concentrated electrolytes, which is supported by the low intensity of free band in IR spectra. The percentage of free ACN in the simulation box is calculated to be ~6%, which is similar to the result previously determined by FTIR experiment (~8%). AIMDS also predicts that the total coordination number of Li+ in the ACN/LiTFSI system is 4.24, which is slightly larger than the coordination number in dilute electrolytes (~4).[67, 77, 169, 239, 265] Higher coordination number in the concentrated electrolyte demonstrates an expansion of the first solvation shell due to the extensive coordination between Li+ and counter-ions.

It has been shown that the sulfonylimide anions have four possible coordination sites (four O atoms). Hence, TFSI- can coordinate Li+ in several possible configurations.[67, 98, 100] The most popular configurations of TFSI- coordinating Li+ are monodentate and bidentate as shown in Scheme 5.2, where the Li+ is coordinated by one or two O atoms of a TFSI-, respectively. Similar structures can also be formed for the coordination between Li+ and FSI-/BETI-. AIMDS of the ACN/LiTFSI system supports the configurations of both monodentate and bidentate coordination of TFSI-. Especially, there are three types of Li+ first solvation shells that are commonly seen throughout the 100 ps run. (Scheme 5.2) The first type is defined as mixed configuration with both monodentate and bidentate TFSI-. In this type of solvation shell, besides one coordinated ACN, two TFSI- ions coordinate the same Li+ in different forms: one is monodentate, the other one is bidentate. The second type is defined as double monodentate,

where two TFSI- anions coordinate the same Li+, each by one O atom, with the other two coordination sites occupied by two ACN molecules. The third type is bidentate, which has one TFSI- coordinating Li+ by two O atoms and two ACN molecules coordinating the same cation to make a coordination number of four. Note that similar solvation structures were derived for the concentrated electrolytes of carbonate solvents as well.[101] Despite the different configurations of TFSI- solvation, the frequency of acetonitrile CN stretch in the IR spectra appears to be invariant. (Table 5.2) Hence, the different structures of solvation shells cannot be easily discerned from the lineshape of the linear or non-linear IR spectra, which explains why there is only one coordinated peak in the CN stretching region of the IR spectra.

Table 5.2. Frequency calculations for three configurations of the first solvation shells formed by LiTFSI and ACN. The frequency (ω_{CN}) and intensity (I) of coordinated CN stretch are reported in cm^{-1} and km/mol, respectively.

Configurations	ω_{CN} (cm^{-1})	I (km/mol)
mixed	2404.20	136.17
double monodentate	2403.26	148.95
	2403.60	112.85
bidentate	2403.83	210.98
	2404.01	69.01

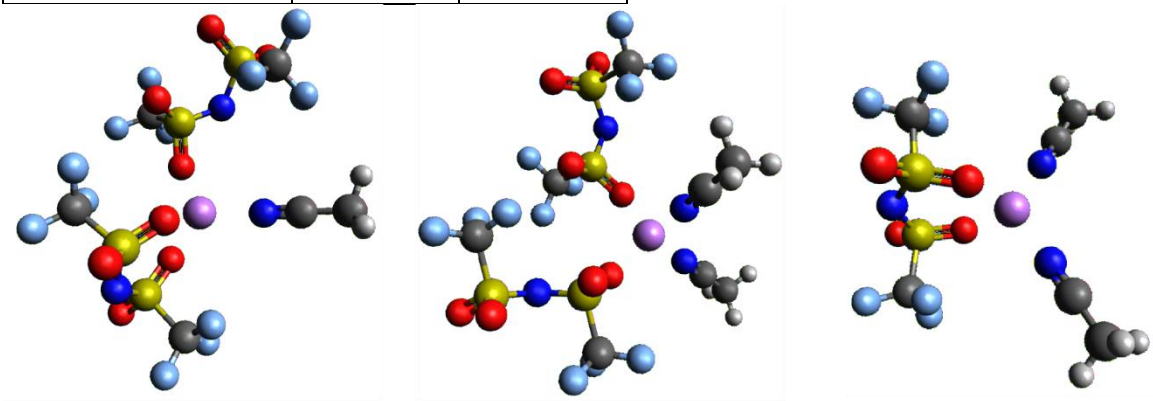

Scheme 5.2. Ball and stick models of the most probable configurations of the first solvation shells for ACN/LiTFSI system at the salt:solvent molar ratio of 1:2. From left to right: (a) mixed, (b) double monodentate, and (c) bidentate configurations. The pink, red, cyan, yellow, gray, light blue and white colors represent Li, O, N, S, C, F and H, respectively.

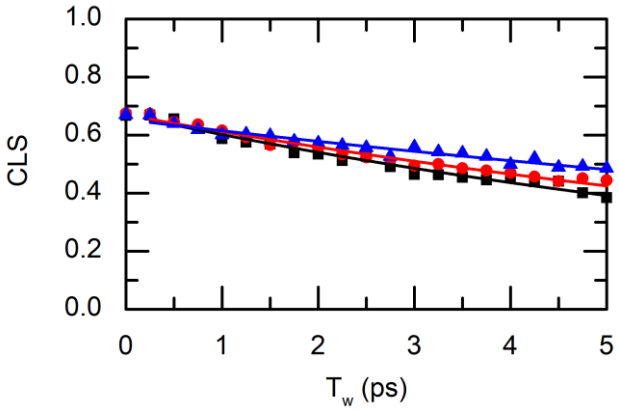

Figure 5.4. CLS of coordinated CN stretch in the 2DIR spectra of three Li salts. Black, red and cyan colors represent the results for LiFSI, LiTFSI and LiBETI, respectively. The lines represent the fitting results of CLS data as discussed in the text.

Table 5.3. Fitting parameters of CLS for the 2DIR spectra of LiFSI, LiTFSI and LiBETI samples.

Sample	τ (ps)	A
ACN/LiFSI	9.3 ± 0.4	0.67 ± 0.01
ACN/LiTFSI	11.0 ± 0.4	0.67 ± 0.01
ACN/LiBETI	16.4 ± 0.9	0.65 ± 0.01

The anion effect on the solvation shell of Li+ is studied through the IR spectra of coordinated solvent molecules. FTIR spectra of three salts share high resemblance at the salt:solvent molar ratio of 1:2. The only difference is a ~2 cm^{-1} blue shift of the coordinated band from LiFSI to LiBETI sample, which is likely due to the change in the dielectric of the mixture. The lineshape of linear absorption spectrum is dependent on the vibrational lifetime, diffusion coefficient and frequency fluctuation of the IR reporter.[107] The similar lineshape of FTIR spectra indicates that the aforementioned properties of CN stretch appear to be very similar even though the counter-ion is different in three samples. It is worth noting that the finding in this work appears to be a match to a previous study on the dilute mixtures of Li salts and ACN, which

revealed very similar IR spectral features of acetonitrile CN stretch irrespective of the solvation structures.[85]

The anion effect on the dynamics of ACN molecules in the Li+ first solation shell is investigated by 2DIR spectroscopy. The peak shape of coordinated band evolves with increasing waiting time, resulted from the gradual decorrelation between the pump and probe frequencies of CN stretch. To model the dynamics of frequency-frequency correlation function (FFCF) of coordinated CN stretch, center line slope (CLS) was analyzed for the coordinated band, as shown in Figure 5.4. The CLS data were modeled with a single exponential decay of the form: $CLS(T_w) = A * e^{-T_w/\tau}$, where A is the amplitude, T_w is the waiting time and τ is the frequency decorrelation time. (Table 5.3) The modeling reveals that the dynamics of FFCF for the concentrated electrolytes (τ) are in the range of 10 to 20 ps, which is almost 10 times slower than that of the dilute electrolyte of LiTFSI in ACN (~1.6 ps).[85] The slower dynamics in concentrated electrolyte indicates a shallower potential well around the coordinated solvent molecules at high concentration of Li+ as described by Kramers theory.[274] The amplitude of CLS (A) is also found to be statistically the same for three samples, while the decorrelation time constant (τ) gets larger from LiFSI to LiTFSI to LiBETI sample. In low concentration electrolyte, the frequency fluctuation of coordinated CN stretch has been assigned to the deformation or the in-place motions of the first solvation shell of Li+.[85] Hence, the faster dynamics of FFCF for the coordinated CN stretch demonstrates a faster deformation of the first solvation shell formed by FSI- than BETI-, namely, the motion of coordinated solvent molecule is within a narrower and deeper potential well in LiFSI sample than in LiBETI sample, with TFSI- sample in between.

The slowdown in FFCF dynamics can arise from different molecular mechanisms. One possible mechanism is that the ion-solvent interactions are different for the different counter-ions. However, the NBO analysis for the bidentate solvation shells of LiFSI, LiTFSi and LiBETI show similar electronic structures around Li+ centers, as shown in Table 5.4. Another possibility is that the frequency fluctuation is related to the energy landscape of moving solvent molecules. Thus, the potential energy surfaces are calculated by adjusting the distance between Li+ and coordinated ACN as one possible coordinate of ACN motion. (Figure 5.5) Note that the distance between Li+ and ACN was adjusted in DFT calculations based on their distributions extracted

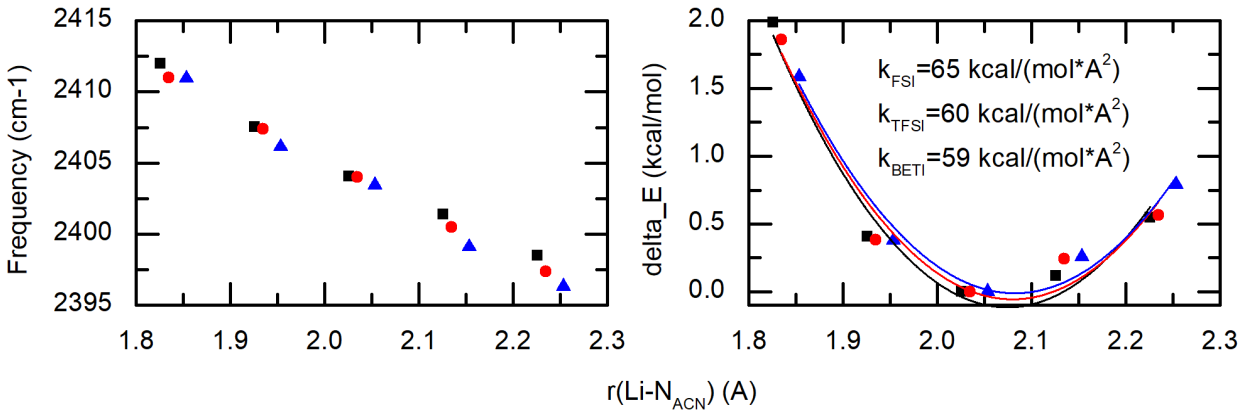

Figure 5.5. Frequency change of coordinated CN stretch and energy landscape of changing the distance between Li+ and N_{ACN} (r(Li-N_{ACN})) in bidentate solvation shells of Li+, calculated by DFT. Black, red and cyan represent the results of LiFSI, LiTFSI and LiBETI, respectively. Each landscape was fitted by a parabolic function based on the energy function of harmonic oscillation. The solid lines show the fitting results. The spring constants, k, from fitting are 65, 60, and 59 kcal/(mol*A^2) for LiFSI, LiTFSI and LiBETI sample, respectively.

Table 5.4. Charge densities on the Li+ and coordinated O_{TFSI}/N_{ACN} calculated by NBO analysis.

Species	Charge on Li+	Charge on N_{ACN}	Charge on O_{TFSI}
$Li(ACN)_2(FSI)$	0.647	-0.387	-0.926
		-0.387	-0.926
$Li(ACN)_2(TFSI)$	0.635	-0.383	-0.945
		-0.383	-0.945
$Li(ACN)_2(BETI)$	0.637	-0.382	-0.947
		-0.379	-0.944

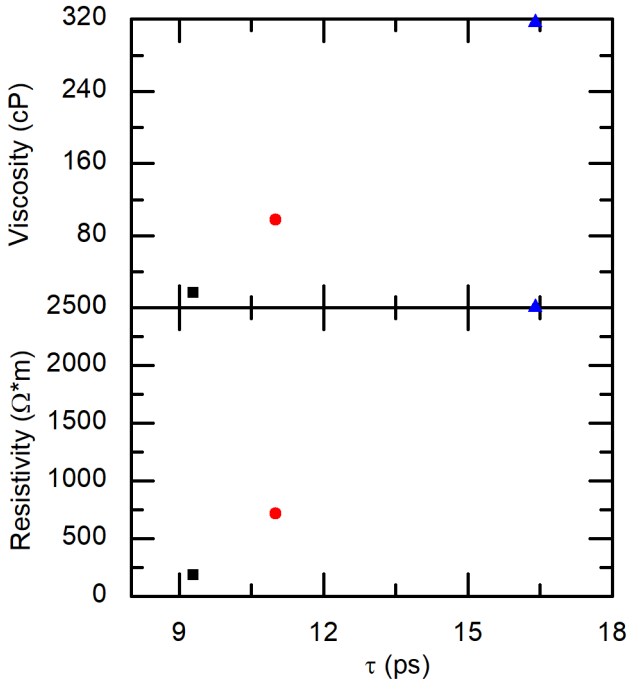

Figure 5.6. Linear relation between FFCF dynamics (τ) and viscosity (upper) or ionic resistivity (lower) of concentrated electrolytes. Results of ACN/LiFSI, ACN/LiTFSI and ACN/LiBETI are represented by black, red and cyan, respectively.

Table 5.5. Ionic conductivity, viscosity and ionic resistivity for three samples: ACN/LiFSI, ACN/LiTFSI, and ACN/LiBETI at the salt:solvent molar ratio of 1:2. All properties were measured at ~23°C.

Sample	Viscosity (cP)	Conductivity (mS/cm)	Resistivity (Ω∗m)
ACN/LiFSI	16.8	5.5	182
ACN/LiTFSI	97.9	1.4	714
ACN/LiBETI	316.2	0.4	2500

from AIMDS trajectories. It is observed that the frequency fluctuates by similar amplitude for the same change in distance, while the energy landscape of ACN motion has no obvious difference among three Li salts. According to Kramers theory[274], the change in energy landscape explains the faster FFCF dynamics in LiFSI system, but no obvious difference can be observed between LiTFSI and LiBETI systems. Another possible explanation for the variant FFCF dynamics is the volume effect, meaning that the deformation of Li+ first solvation shell is less restricted with

increasing anion size. In other words, the Li+ first solvation shell has larger volume with larger anion, which results in a less crowded environment around the coordinated CN stretch. Though this hypothesis is possible, the direct relation between the FFCF dynamics and macroscopic properties suggests otherwise. As shown in Table 5.5 and Figure 5.6, FFCF dynamics of coordinated CN stretch has a linear relation with the viscosity or the resistivity (reciprocal of ionic conductivity) of the sample, which indicates long-range interactions among Li+ first solvation shells in concentrated electrolytes. Since volume effect is a local effect that should only be observed surrounding the first solvation shell of Li+, it is unlikely to be the main reason for the change in FFCF dynamics with increasing anion size. In previous discussion, the local environment within and surrounding the first solvation shell has been investigated. However, no clear connection was found to explain the different FFCF dynamics among three samples measured by 2DIR experiments. Therefore, it is hypothesized that the effect should involve motions beyond the first solvation shells of Li+.

Previously, it was observed that concentrated electrolytes formed by LiTFSI and carbonate solvents present a strong correlation between the Li+-anion coordination and Li+-solvent coordination in the same solvation shell.[101] The making and breaking of coordination bonds between Li+ and TFSI- enable the Li+ transport from one solvation shell to another, which is proposed to be the conduction mechanism for concentrated electrolytes. According to this model, nearby Li+ should be highly correlated through the coordination/decoordination of TFSI from one Li+ center to another. From the AIMDS of ACN/LiTFSI system, a high correlation is found out between nearby first solvation shells in concentrated electrolytes. The g(r) between Li+ and Li+, as well as the correlation function (CF) of the distance between two closest Li+ (r(Li-Li)) were analyzed and shown in Figure 5.7. The data of $CF_{r(Li\text{-}Li)}$ was fitted by a double

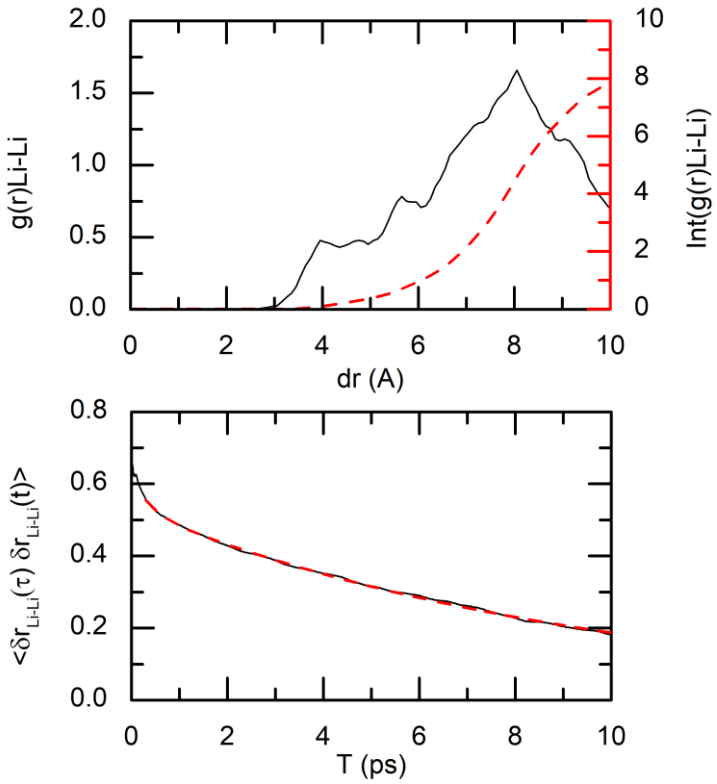

Figure 5.7. High correlation between nearby Li+ supported by AIMDS. The g(r)Li-Li (black solid line) and Int(g(r)Li-Li) (red dotted line) between Li+ and Li+ are shown in the top panel. The correlation function of the distance between two closest Li+ ($CF_{r(Li\text{-}Li)}$) is shown in the bottom panel. The fitting of $CF_{r(Li\text{-}Li)}$ is shown as the red dotted line.

Table 5.6. Fitting parameters of the correlation function of the distance between two closest Li+.

Factor	Params.	Params.	Params.	Params.
	τ_1 (ps)	A_1	τ_2 (ps)	A_2
r(Li-Li)	9.6 ± 0.1	0.53 ± 0.01	0.36 ± 0.01	0.09 ± 0.01

exponential function: $CF(T) = A_1 * e^{-T/\tau_1} + A_2 * e^{-T/\tau_2}$, where A_1, A_2 are the amplitudes, T is the time and τ_1, τ_2 are the time constants. (Table 5.6) Notice that the fast decay time τ_2 (0.36 ps) is likely due to the local oscillation of Li+, and the definition of a cutoff distance. It is shown that the two closest Li+ are separated by ~6 Å, and the dynamics of the distance between them (τ_1) is on the order of ~10 ps. The match between the dynamics of CF(r(Li-Li)) from AIMDS and the

FFCF dynamics from 2DIR experiment confirms the high correlation between nearby Li+, supporting the model proposed previously for the concentrated electrolytes of carbonate solvents.

Further analysis of the correlation functions of the geometrical factors in Li+ first solvation shell demonstrates the fully correlated dynamics within and beyond the first solvation shell. The CFs of four factors were calculated and fitted by exponential decay functions. (Figure 5.8) Note that the CF of the distance between Li+ and coordinated N_{ACN} (r(Li-N_{ACN})) was modeled with a single exponential decay of the form: $CF(T) = A_1 * e^{-T/\tau_1}$, where A_1 is the amplitude, T is the time and τ_1 is the time constant, while the others were fitted by a bi-exponential decay as described previously for the fitting of $CF_{r(Li\text{-}Li)}$. It is indicated that all geometrical factors in Li+ first solvation shell have similar dynamics of ~10 ps. The dynamics of these geometrical factors in the first solvation shell (Table 5.7) match the dynamics of r(Li-Li) (Table 5.6), which also matches the FFCF dynamics measured by 2DIR experiment (Table 5.3). The similarity in the dynamics inside and outside the first solvation shell of Li+ supports the idea of a highly correlated network in the concentrated electrolyte. This explains why DFT calculations did not capture the difference among three Li salts. It is worth noting that the fully correlated dynamics within and beyond the Li+ first solvation shell results from two aspects. One is the bridge between nearby Li+ through the coordination of TFSI-. For example, it is observed that one TFSI- anion can coordinate more than one Li+, forming a bridge between cations. The correlation between cations also arises from the coordination/decoordination of TFSI- from one Li+ center to another. For example, a coordination bond between a TFSI- and Li+ breaks, which initiates the making of a new coordination bond between this TFSI- and a different Li+. Based on this model, the ion-ion interactions dominate the making and breaking of coordination bonds around Li+ centers, where the ion-dipole interactions make adjustments accordingly. Therefore,

the slowdown of FFCF dynamics from LiFSI to LiBETI sample should be related to the dynamics of the making/breaking of ion-ion coordination bonds in concentrated electrolytes. AIMDSs of ACN/LiFSI and ACN/LiBETI are necessary for studying the molecular origin of the slowdown in FFCF dynamics of coordinated CN stretch, which will be conducted in future study.

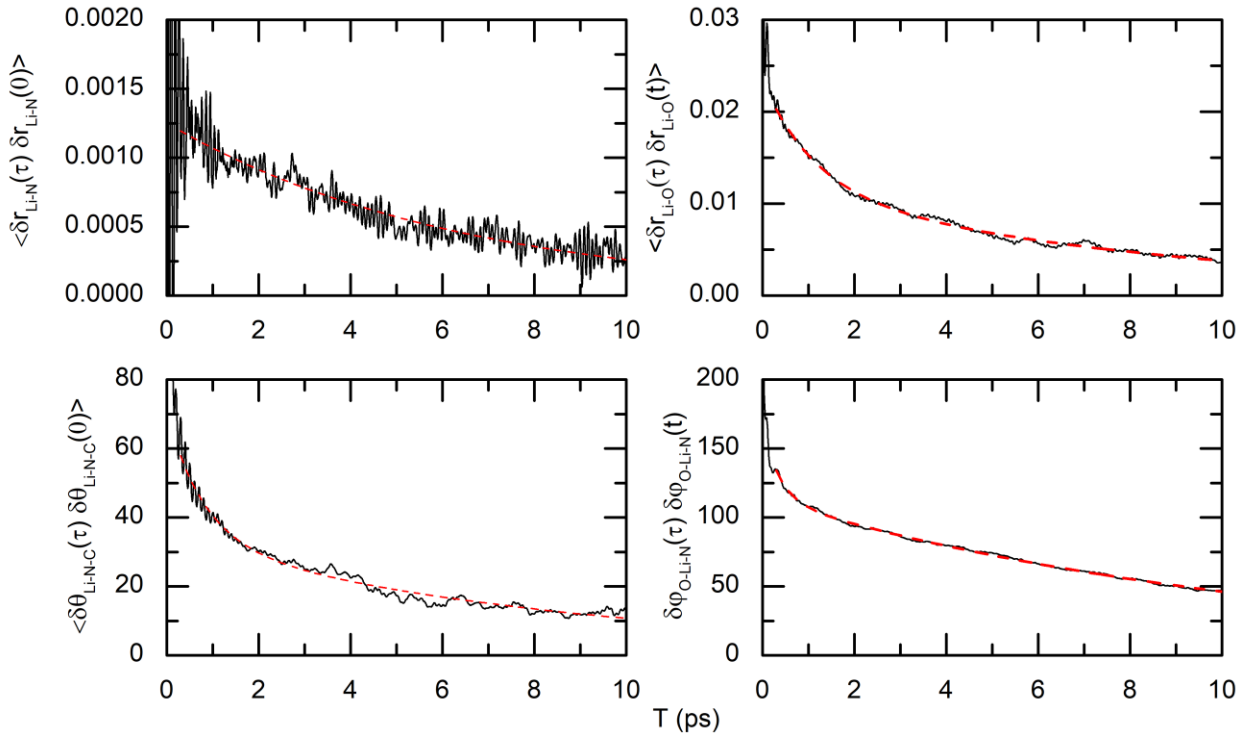

Figure 5.8. Autocorrelation functions of four geometrical factors: the distance between Li+ and N_{ACN} (r(Li-N_{ACN}), top left), the distance between Li+ and O_{TFSI} (r(Li-O_{TFSI}), top right), the angle Li-N≡C (θ, bottom left), and the angle N_{ACN}-Li-O_{TFSI} (φ, bottom right). The red dash lines represent the fitting results as described in the text.

Table 5.7. Fitting parameters of autocorrelation functions of four geometrical factors: the distance between Li+ and N_{ACN} (r(Li-N_{ACN})), the distance between Li+ and O_{TFSI} (r(Li-O_{TFSI})), the angle Li-N≡C (θ), and the angle N_{ACN}-Li-O_{TFSI} (φ).

Factor	Params.	Params.	Params.	Params.
	τ_1 (ps)	A_1	τ_2 (ps)	A_2
r(Li-N_{ACN})	6.4 ± 0.1	0.0013 ± 0.0001	-	-
r(Li-O_{TFSI})	8.9 ± 0.1	0.012± 0.0001	1.13 ± 0.02	0.012± 0.001
θ(Li-N≡C)	8.8 ± 0.1	33.4 ± 0.3	0.80 ± 0.02	37.1 ± 0.6
φ(N_{ACN}-Li-O_{TFSI})	11.1 ± 0.1	113.8± 0.1	0.36 ± 0.01	53 ± 1

Based on all observations in this work, a general picture of the highly correlated network in a concentrated electrolyte is established. A previous study proposed that concentrated mixtures of Li salts and organic solvents behave in part like ionic liquid instead of typical solutions.[269] Another study of ionic liquid observed a linear relation between the lifetime of ion cages and the viscosity of ionic liquids.[275] The making and breaking of local ion-cages in ionic liquid were proposed to be the fundamental event that activates molecular diffusion and thus determines the viscosity of the fluids.[275] The same linear relation is observed between the FFCF dynamics of coordinated CN stretch (τ) and the viscosity of concentrated lithium ion electrolytes. (Table 5.3, Table 5.5 and Figure 5.6) Following the similar principle in ionic liquids, The viscosity of concentrated electrolytes should result from the breakup of coordination bonds between ions, which causes ion transport in the samples. The higher viscosity corresponds to a slower molecular diffusion, or in other words, a slower breakup of ionic cages in LiBETI than in LiFSI solutions. Besides, another study on deep eutectic solvents (DES) observed a linear relation between the ionic resistivity and the reorientational relaxation times in DESs, which is proposed to arise in part from a revolving-door mechanism.[276] Within this mechanism, the most mobile ions find additional paths that allow them to bypass the "doors" formed by urea molecules and less mobile ions. Similar relation is observed for the FFCF dynamics of coordinated CN stretch (τ) and the resistivity of concentrated electrolytes. (Figure 5.6) As stated previously, the dynamics of solvent is dominated by the making and breaking of ion-ion coordination bonds, which is possibly related to the reorientation of anions around Li+ centers. The relation between τ and resistivity could arise from a similar mechanism as revolving-door mechanism, where the charges are transported in the highly correlated network formed by Li+ and TFSI- ions. When the making and breaking of ion-ion coordination bonds slow down from LiFSI to LiBETI sample, the ion transport gets slower, and

thus, the resistivity is higher. Overall, the direct relation between molecular motions and the macroscopic properties is a result of long-range interactions among ions in the concentrated electrolyte. Thus, all observations in this work support the proposed model of highly correlated networks in concentrated electrolytes.

5.5. Summary

This study investigated the molecular origin of the macroscopic properties of concentrated lithium ion electrolytes through the linear and non-linear infrared spectroscopies, with the assistance of DFT calculation and AIMDS. For that purpose, a family of lithium sulfonylimide salts with increasing anion size was used (LiFSI, LiTFSI and LiBETI) to prepare concentrated electrolyte in ACN. Our findings showed that the coordinated CN stretch of ACN has highly resembled spectral features in the IR spectra irrespective of the Li salts. The 2DIR experiments of the concentrated electrolytes at the salt:solvent molar ratio of 1:2 revealed that the FFCF dynamics of coordinated CN stretch slows down with increasing anion size. The direct relation between FFCF dynamics and macroscopic properties of samples indicates long-range interactions among ions in concentrated electrolytes. The analysis of AIMDS of ACN/LiTFSI system showed a fully correlated dynamics within and beyond the Li+ first solvation shell, which supports a model of highly correlated networks in concentrated electrolytes. Based on all observations in this work, a molecular picture for the concentrated electrolyte is established. The making and breaking of ion-ion coordination bonds dominate the overall dynamics inside and outside the first solvation shell of Li+. A highly correlated network was formed in the concentrated electrolyte, where the molecular motions are interconnected among first solvation shells, and thus each first solvation shell cannot be studied independently. Overall, this work proposes the model of highly correlated networks for describing highly concentrated electrolytes,

and reveals the molecular origin of the macroscopic properties in a family of concentrated lithium ion electrolytes.

APPENDIX A. COPYRIGHT RELEASE FOR CHAPTER 3

Structure and dynamics of the lithium ion solvation shell in ureas

Chen, X.; Fulfer, K. D.; Woodard, K. T.; Kuroda, D. G., *The Journal of Physical Chemistry B*. 2019, *123* (46), 9889-9898.

DOI: 10.1021/acs.jpcb.9b07623

A link to the published paper

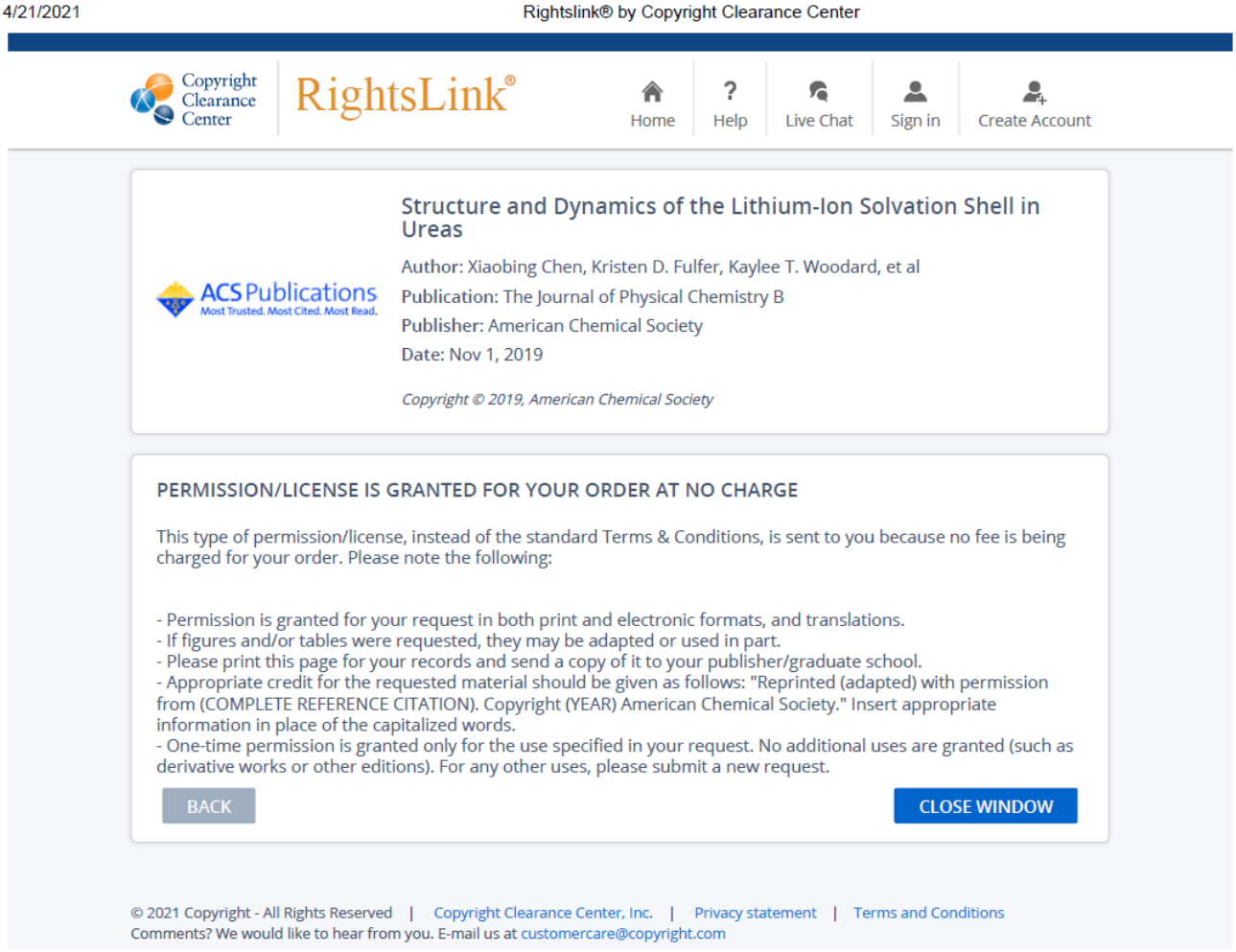

APPENDIX B. COPYRIGHT RELEASE FOR CHAPTER 4

Molecular motions of acetonitrile molecules in the solvation shell of lithium ions

Chen, X.; Kuroda, D. G., *The Journal of Chemical Physics* 2020, *153* (16), 164502.

DOI: 10.1063/5.0024486

A link to the published paper

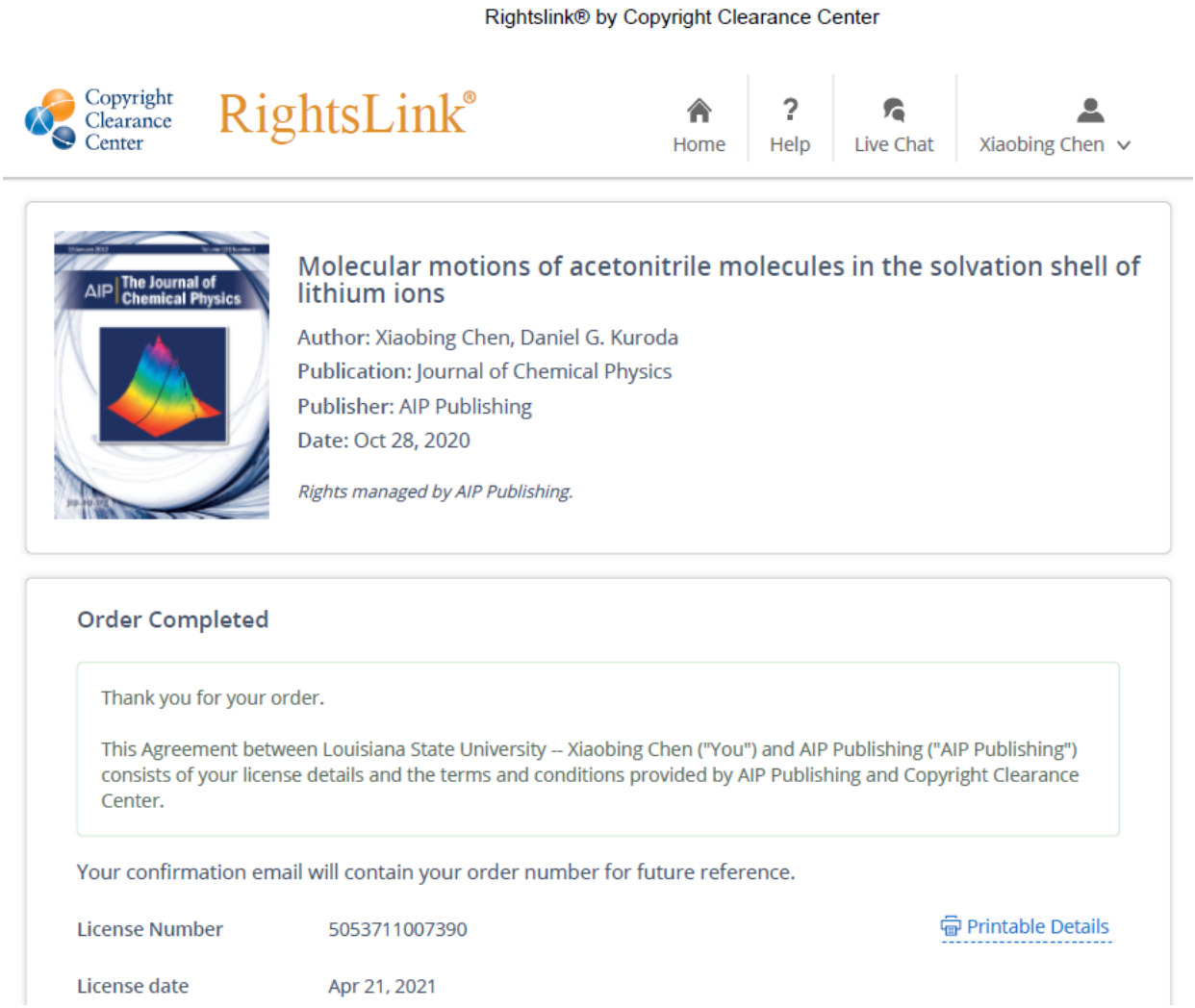

Licensed Content

Licensed Content Publisher	AIP Publishing
Licensed Content Publication	Journal of Chemical Physics
Licensed Content Title	Molecular motions of acetonitrile molecules in the solvation shell of lithium ions
Licensed Content Author	Xiaobing Chen, Daniel G. Kuroda
Licensed Content Date	Oct 28, 2020
Licensed Content Volume	153
Licensed Content Issue	16

Order Details

Type of Use	Thesis/Dissertation
Requestor type	Author (original article)
Format	Electronic
Portion	Excerpt (> 800 words)
Will you be translating?	No

About Your Work

Title	Investigation on the Structure and Dynamics of Lithium Ion Solvation Shell by Linear and Non-linear Infrared Spectroscopy
Institution name	Louisiana State University
Expected presentation date	Jul 2021

Additional Data

Portions	Full article

Requestor Location

Requestor Location	Louisiana State University 3964 Gourrier Ave BATON ROUGE, LA 70808 United States Attn: Louisiana State University

Tax Details

$ Price

Total	0.00 USD

Total: 0.00 USD

CLOSE WINDOW ORDER MORE

REFERENCE LIST

1. Leuthner, S., Lithium-ion battery overview. In *Lithium-Ion Batteries: Basics and Applications*, Korthauer, R., Ed. Springer Berlin Heidelberg: Berlin, Heidelberg, 2018; pp 13-19.

2. Wen, J.; Yu, Y.; Chen, C., A Review on Lithium-Ion Batteries Safety Issues: Existing Problems and Possible Solutions. *Materials Express* **2012,** *2* (3), 197-212.

3. Han, X.; Lu, L.; Zheng, Y.; Feng, X.; Li, Z.; Li, J.; Ouyang, M., A review on the key issues of the lithium ion battery degradation among the whole life cycle. *eTransportation* **2019,** *1*, 100005.

4. Zhang, H.; Liu, S.; Yu, X.; Chen, S., Improving rate capacity and cycling stability of Si-anode lithium ion battery by using copper nanowire as conductive additive. *Journal of Alloys and Compounds* **2020,** *822*, 153664.

5. Xu, K., Nonaqueous Liquid Electrolytes for Lithium-Based Rechargeable Batteries. *Chemical Reviews* **2004,** *104* (10), 4303-4418.

6. Jow, T. R.; Xu, K.; Borodin, O.; Ue, M., *Electrolytes for lithium and lithium-ion batteries*. Springer: 2014; Vol. 58.

7. McOwen, D. W.; Seo, D. M.; Borodin, O.; Vatamanu, J.; Boyle, P. D.; Henderson, W. A., Concentrated electrolytes: decrypting electrolyte properties and reassessing Al corrosion mechanisms. *Energy & Environmental Science* **2014,** *7* (1), 416-426.

8. Sogawa, M.; Sawayama, S.; Han, J.; Satou, C.; Ohara, K.; Matsugami, M.; Mimura, H.; Morita, M.; Fujii, K., Role of solvent size in ordered ionic structure formation in concentrated electrolytes for lithium-ion batteries. *The Journal of Physical Chemistry C* **2019,** *123* (14), 8699-8708.

9. Amine, R.; Liu, J.; Acznik, I.; Sheng, T.; Lota, K.; Sun, H.; Sun, C.-J.; Fic, K.; Zuo, X.; Ren, Y.; El-Hady, D. A.; Alshitari, W.; Al-Bogami, A. S.; Chen, Z.; Amine, K.; Xu, G.-L., Regulating the Hidden Solvation-Ion-Exchange in Concentrated Electrolytes for Stable and Safe Lithium Metal Batteries. *Advanced Energy Materials* **2020,** *10* (25), 2000901.

10. Yamada, Y.; Furukawa, K.; Sodeyama, K.; Kikuchi, K.; Yaegashi, M.; Tateyama, Y.; Yamada, A., Unusual Stability of Acetonitrile-Based Superconcentrated Electrolytes for Fast-Charging Lithium-Ion Batteries. *Journal of the American Chemical Society* **2014,** *136* (13), 5039-5046.

11. Ozawa, K., *Lithium ion rechargeable batteries: materials, technology, and new applications*. John Wiley & Sons: 2012.

12. Ramanan, A., Nobel Prize in Chemistry 2019. *Resonance* **2019,** *24* (12), 1381-1395.

13. Whittingham, M. S., Ultimate Limits to Intercalation Reactions for Lithium Batteries. *Chemical Reviews* **2014,** *114* (23), 11414-11443.

14. Winter, M.; Barnett, B.; Xu, K., Before Li Ion Batteries. *Chemical Reviews* **2018,** *118* (23), 11433-11456.

15. Park, J.; Jeong, J.; Lee, Y.; Oh, M.; Ryou, M.-H.; Lee, Y. M., Micro-Patterned Lithium Metal Anodes with Suppressed Dendrite Formation for Post Lithium-Ion Batteries. *Advanced Materials Interfaces* **2016,** *3* (11), 1600140.

16. Selis, L. A.; Seminario, Jorge M., Dendrite formation in silicon anodes of lithium-ion batteries. *RSC Advances* **2018,** *8* (10), 5255-5267.

17. Moeller, K.-C., Overview of battery systems. In *Lithium-Ion Batteries: Basics and Applications*, Korthauer, R., Ed. Springer Berlin Heidelberg: Berlin, Heidelberg, 2018; pp 3-10.

18. Quinn, J. B.; Waldmann, T.; Richter, K.; Kasper, M.; Wohlfahrt-Mehrens, M., Energy Density of Cylindrical Li-Ion Cells: A Comparison of Commercial 18650 to the 21700 Cells. *Journal of The Electrochemical Society* **2018,** *165* (14), A3284-A3291.

19. Kim, J.-S.; Lee, D.-C.; Lee, J.-J.; Kim, C.-W., Optimization for maximum specific energy density of a lithium-ion battery using progressive quadratic response surface method and design of experiments. *Scientific Reports* **2020,** *10* (1), 15586.

20. Ning, G.; Popov, B. N., Cycle Life Modeling of Lithium-Ion Batteries. *Journal of The Electrochemical Society* **2004,** *151* (10), A1584.

21. Valøen, L. O.; Shoesmith, M. I. In *The effect of PHEV and HEV duty cycles on battery and battery pack performance*, Plug-in hybrid electric Vehicle Conference, 2007.

22. Blomgren, G. E., The Development and Future of Lithium Ion Batteries. *Journal of The Electrochemical Society* **2016,** *164* (1), A5019-A5025.

23. Liang, R.-f.; Wang, Z.-x.; Guo, H.-j.; Li, X.-h.; Peng, W.-j.; Wang, Z.-g., Fabrication and electrochemical properties of lithium-ion batteries for power tools. *Journal of Power Sources* **2008,** *184* (2), 598-603.

24. Lu, L.; Han, X.; Li, J.; Hua, J.; Ouyang, M., A review on the key issues for lithium-ion battery management in electric vehicles. *Journal of Power Sources* **2013,** *226*, 272-288.

25. Zubi, G.; Dufo-López, R.; Carvalho, M.; Pasaoglu, G., The lithium-ion battery: State of the art and future perspectives. *Renewable and Sustainable Energy Reviews* **2018,** *89*, 292-308.

26. Maiyalagan, T.; Elumalai, P., *Rechargeable Lithium-ion Batteries: Trends and Progress in Electric Vehicles*. CRC Press: 2020.

27. Masias, A.; Marcicki, J.; Paxton, W. A., Opportunities and Challenges of Lithium Ion Batteries in Automotive Applications. *ACS Energy Letters* **2021,** *6* (2), 621-630.

28. Chen, T.; Jin, Y.; Lv, H.; Yang, A.; Liu, M.; Chen, B.; Xie, Y.; Chen, Q., Applications of Lithium-Ion Batteries in Grid-Scale Energy Storage Systems. *Transactions of Tianjin University* **2020,** *26* (3), 208-217.

29. Walter, M.; Kovalenko, M. V.; Kravchyk, K. V., Challenges and benefits of post-lithium-ion batteries. *New Journal of Chemistry* **2020,** *44* (5), 1677-1683.

30. Chen, Y.; Kang, Y.; Zhao, Y.; Wang, L.; Liu, J.; Li, Y.; Liang, Z.; He, X.; Li, X.; Tavajohi, N.; Li, B., A review of lithium-ion battery safety concerns: The issues, strategies, and testing standards. *Journal of Energy Chemistry* **2021,** *59*, 83-99.

31. Aravindan, V.; Gnanaraj, J.; Madhavi, S.; Liu, H.-K., Lithium-Ion Conducting Electrolyte Salts for Lithium Batteries. *Chemistry – A European Journal* **2011,** *17* (51), 14326-14346.

32. Markovsky, B.; Amalraj, F.; Gottlieb, H.; Gofer, Y.; Martha, S.; Aurbach, D., On the Electrochemical Behavior of Aluminum Electrodes in Nonaqueous Electrolyte Solutions of Lithium Salts. *Journal of The Electrochemical Society* **2010,** *157*.

33. Kawamura, T.; Okada, S.; Yamaki, J.-i., Decomposition reaction of LiPF6-based electrolytes for lithium ion cells. *Journal of Power Sources* **2006,** *156* (2), 547-554.

34. Yazami, R.; Martinent, A., Chapter 8 - Fluorinated anions and electrode/electrolyte stability in lithium batteries. In *Fluorinated Materials for Energy Conversion*, Nakajima, T.; Groult, H., Eds. Elsevier Science: Amsterdam, 2005; pp 173-194.

35. Choi, N.-S.; Profatilova, I. A.; Kim, S.-S.; Song, E.-H., Thermal reactions of lithiated graphite anode in LiPF6-based electrolyte. *Thermochimica Acta* **2008,** *480* (1), 10-14.

36. Yang, H.; Shen, X.-D., Dynamic TGA–FTIR studies on the thermal stability of lithium/graphite with electrolyte in lithium-ion cell. *Journal of Power Sources* **2007,** *167* (2), 515-519.

37. Sharabi, R.; Markevich, E.; Borgel, V.; Salitra, G.; Gershinsky, G.; Aurbach, D.; Semrau, G.; Schmidt, M. A.; Schall, N.; Stinner, C., Raman study of structural stability of LiCoPO4 cathodes in LiPF6 containing electrolytes. *Journal of Power Sources* **2012,** *203*, 109-114.

38. Zheng, H.; Sun, Q.; Liu, G.; Song, X.; Battaglia, V. S., Correlation between dissolution behavior and electrochemical cycling performance for LiNi1/3Co1/3Mn1/3O2-based cells. *Journal of Power Sources* **2012,** *207*, 134-140.

39. Younesi, R.; Veith, G. M.; Johansson, P.; Edström, K.; Vegge, T., Lithium salts for advanced lithium batteries: Li–metal, Li–O2, and Li–S. *Energy & Environmental Science* **2015,** *8* (7), 1905-1922.

40. Sasaki, Y.; Handa, M.; Kurashima, K.; Tonuma, T.; Usami, K., Application of Lithium Organoborate with Salicylic Ligand to Lithium Battery Electrolyte. *Journal of The Electrochemical Society* **2001,** *148* (9), A999.

41. Marom, R.; Haik, O.; Aurbach, D.; Halalay, I. C., Revisiting $LiClO_4$ as an Electrolyte for Rechargeable Lithium-Ion Batteries. *Journal of The Electrochemical Society* **2010,** *157* (8), A972.

42. Ein-Eli, Y.; Thomas, S. R.; Chadha, R.; Blakley, T. J.; Koch, V. R., Li-Ion Battery Electrolyte Formulated for Low-Temperature Applications. *Journal of The Electrochemical Society* **1997,** *144* (3), 823-829.

43. Archuleta, M. M., Toxicity of materials used in the manufacture of lithium batteries. *Journal of Power Sources* **1995,** *54* (1), 138-142.

44. Ping, P.; Wang, Q.; Sun, J.; Xiang, H.; Chen, C., Thermal Stabilities of Some Lithium Salts and Their Electrolyte Solutions With and Without Contact to a LiFePO[sub 4] Electrode. *Journal of The Electrochemical Society* **2010,** *157* (11), A1170.

45. Hong, E.-S.; Okada, S.; Sonoda, T.; Gopukumar, S.; Yamaki, J.-i., Thermal Stability of Electrolytes with Mixtures of LiPF[sub 6] and LiBF[sub 4] Used in Lithium-Ion Cells. *Journal of The Electrochemical Society* **2004,** *151* (11), A1836.

46. Li, J.; Yuan, C. F.; Guo, Z. H.; Zhang, Z. A.; Lai, Y. Q.; Liu, J., Limiting factors for low-temperature performance of electrolytes in LiFePO4/Li and graphite/Li half cells. *Electrochimica Acta* **2012,** *59*, 69-74.

47. Zhang, S. S.; Xu, K.; Jow, T. R., Study of $LiBF_4$ as an Electrolyte Salt for a Li-Ion Battery. *Journal of The Electrochemical Society* **2002,** *149* (5), A586.

48. Ding, M. S.; Richard Jow, T., How Conductivities and Viscosities of PC-DEC and PC-EC Solutions of LiBF[sub 4], LiPF[sub 6], LiBOB, Et[sub 4]NBF[sub 4], and Et[sub 4]NPF[sub 6] Differ and Why. *Journal of The Electrochemical Society* **2004,** *151* (12), A2007.

49. Xue, L.; Padgett, C. W.; DesMarteau, D. D.; Pennington, W. T., Synthesis and structures of alkali metal salts of bis[(trifluoromethyl)sulfonyl]imide. *Solid State Sciences* **2002,** *4* (11), 1535-1545.

50. Rey, I.; Johansson, P.; Lindgren, J.; Lassègues, J. C.; Grondin, J.; Servant, L., Spectroscopic and Theoretical Study of (CF3SO2)2N- (TFSI-) and (CF3SO2)2NH (HTFSI). *The Journal of Physical Chemistry A* **1998,** *102* (19), 3249-3258.

51. Webber, A., Conductivity and Viscosity of Solutions of LiCF3 SO 3, Li (CF 3 SO 2) 2 N , and Their Mixtures. *Journal of The Electrochemical Society* **1991,** *138* (9), 2586-2590.

52. Benrabah, D.; Arnaud, R.; Sanchez, J., Comparative ab initio calculations on several salts. *Electrochimica acta* **1995,** *40* (13-14), 2437-2443.

53. Steudte, S.; Neumann, J.; Bottin-Weber, U.; Diedenhofen, M.; Arning, J.; Stepnowski, P.; Stolte, S., Hydrolysis study of fluoroorganic and cyano-based ionic liquid anions–consequences for operational safety and environmental stability. *Green chemistry* **2012,** *14* (9), 2474-2483.

54. Chagnes, A.; Carré, B.; Willmann, P.; Lemordant, D., Modeling viscosity and conductivity of lithium salts in γ-butyrolactone. *Journal of Power Sources* **2002,** *109* (1), 203-213.

55. Dudley, J.; Wilkinson, D.; Thomas, G.; LeVae, R.; Woo, S.; Blom, H.; Horvath, C.; Juzkow, M.; Denis, B.; Juric, P., Conductivity of electrolytes for rechargeable lithium batteries. *Journal of power sources* **1991,** *35* (1), 59-82.

56. Zhang, S.; Jow, T., Aluminum corrosion in electrolyte of Li-ion battery. *Journal of Power Sources* **2002,** *109* (2), 458-464.

57. Kanamura, K.; Umegaki, T.; Shiraishi, S.; Ohashi, M.; Takehara, Z.-i., Electrochemical behavior of al current collector of rechargeable lithium batteries in propylene carbonate with licf3 so 3, li (cf 3 so 2) 2 n, or li (c 4 f 9 so 2)(cf 3 so 2) n. *Journal of the Electrochemical Society* **2002,** *149* (2), A185.

58. Ue, M., Secondary batteries-Lithium rechargeable systems | Electrolytes: Nonaqueous. In *Encyclopedia of Electrochemical Power Sources*, Garche, J., Ed. Elsevier: Amsterdam, 2009; pp 71-84.

59. Durmus, Y. E.; Zhang, H.; Baakes, F.; Desmaizieres, G.; Hayun, H.; Yang, L.; Kolek, M.; Küpers, V.; Janek, J.; Mandler, D.; Passerini, S.; Ein-Eli, Y., Side by Side Battery Technologies with Lithium-Ion Based Batteries. *Advanced Energy Materials* **2020,** *10* (24), 2000089.

60. Tanaka, Y.; Kaneko, J.; Minoshima, M.; Iriyama, Y.; Fujinami, T., Electrochemical Properties of a Mixed Boric Ester as a Novel Electrolyte Solvent. *Electrochemistry* **2010,** *78* (5), 397-399.

61. Horino, T.; Tamada, H.; Kishimoto, A.; Kaneko, J.; Iriyama, Y.; Tanaka, Y.; Fujinami, T., High Voltage Stability of Interfacial Reaction at the LiMn[sub 2]O[sub 4] Thin-Film Electrodes/Liquid Electrolytes with Boroxine Compounds. *Journal of The Electrochemical Society* **2010,** *157* (6), A677.

62. Wang, X.; Yasukawa, E.; Kasuya, S., Nonflammable Trimethyl Phosphate Solvent-Containing Electrolytes for Lithium-Ion Batteries: I. Fundamental Properties. *Journal of The Electrochemical Society* **2001,** *148* (10), A1058.

63. Xu, K.; Ding, M. S.; Zhang, S.; Allen, J. L.; Jow, T. R., Evaluation of Fluorinated Alkyl Phosphates as Flame Retardants in Electrolytes for Li-Ion Batteries: I. Physical and Electrochemical Properties. *Journal of The Electrochemical Society* **2003,** *150* (2), A161.

64. Ue, M.; Takehara, M.; Takeda, M., Triethylmethylammonium Tetrafluoroborate as a Highly Soluble Supporting Electrolyte Salt for Electrochemical Capacitors. *Denki Kagaku oyobi Kogyo Butsuri Kagaku* **1997,** *65* (11), 969-971.

65. Fouache-Ayoub, S.; Garreau, M.; Prabhu, P. V. S. S.; Thevenin, J., Mass-Transport Properties of Lithium Surface Layers Formed in Sulfolane-Based Electrolytes. *Journal of The Electrochemical Society* **1990,** *137* (6), 1659-1665.

66. Chen, X.; Fulfer, K. D.; Woodard, K. T.; Kuroda, D. G., Structure and Dynamics of the Lithium-Ion Solvation Shell in Ureas. *The Journal of Physical Chemistry B* **2019,** *123* (46), 9889-9898.

67. Seo, D. M.; Borodin, O.; Han, S.-D.; Boyle, P. D.; Henderson, W. A., Electrolyte Solvation and Ionic Association II. Acetonitrile-Lithium Salt Mixtures: Highly Dissociated Salts. *Journal of The Electrochemical Society* **2012,** *159* (9), A1489-A1500.

68. Hilbig, P.; Ibing, L.; Streipert, B.; Wagner, R.; Winter, M.; Cekic-Laskovic, I., Acetonitrile-based electrolytes for lithium-ion battery application. *Curr. Top. Electrochem* **2018,** *20*, 1-30.

69. Ohzuku, T.; Brodd, R. J., An overview of positive-electrode materials for advanced lithium-ion batteries. *Journal of Power Sources* **2007,** *174* (2), 449-456.

70. Cha, H.; Kim, J.; Lee, Y.; Cho, J.; Park, M., Issues and Challenges Facing Flexible Lithium-Ion Batteries for Practical Application. *Small* **2018,** *14* (43), 1702989.

71. Lee, K. K.; Park, K.; Lee, H. C.; Noh, Y. H.; Kossowska, D.; Kwak, K.; Cho, M., Ultrafast fluxional exchange dynamics in electrolyte solvation sheath of lithium ion battery. *Nature Communications* **2017,** *8*.

72. Lim, J.; Lee, K.-K.; Liang, C.; Park, K.-H.; Kim, M.; Kwak, K.; Cho, M., Two-dimensional infrared spectroscopy and molecular dynamics simulation studies of nonaqueous lithium ion battery electrolytes. *The Journal of Physical Chemistry B* **2019,** *123* (31), 6651-6663.

73. Hartnig, C.; Schmidt, M., Electrolytes and conducting salts. In *Lithium-Ion Batteries: Basics and Applications*, Springer: 2018; pp 59-74.

74. Fulfer, K. D.; Kuroda, D. G., A comparison of the solvation structure and dynamics of the lithium ion in linear organic carbonates with different alkyl chain lengths. *Physical chemistry chemical physics : PCCP* **2017,** *19* (36), 25140-25150.

75. Xu, K.; Zhang, S.; Poese, B. A.; Jow, T. R., Lithium bis (oxalato) borate stabilizes graphite anode in propylene carbonate. *Electrochemical and Solid State Letters* **2002,** *5* (11), A259.

76. Wang, Y.; Balbuena, P. B., Theoretical insights into the reductive decompositions of propylene carbonate and vinylene carbonate: density functional theory studies. *The Journal of Physical Chemistry B* **2002,** *106* (17), 4486-4495.

77. Fulfer, K. D.; Kuroda, D. G., Solvation Structure and Dynamics of the Lithium Ion in Organic Carbonate-Based Electrolytes: A Time-Dependent Infrared Spectroscopy Study. *The Journal of Physical Chemistry C* **2016,** *120* (42), 24011-24022.

78. Maeda, S.; Kameda, Y.; Amo, Y.; Usuki, T.; Ikeda, K.; Otomo, T.; Yanagisawa, M.; Seki, S.; Arai, N.; Watanabe, H.; Umebayashi, Y., Local Structure of Li+ in Concentrated Ethylene Carbonate Solutions Studied by Low-Frequency Raman Scattering and Neutron Diffraction with 6Li/7Li Isotopic Substitution Methods. *The Journal of Physical Chemistry B* **2017,** *121* (48), 10979-10987.

79. Barthel, J.; Buchner, R.; Wismeth, E., FTIR Spectroscopy of Ion Solvation of LiClO4 and LiSCN in Acetonitrile, Benzonitrile, and Propylene Carbonate. *Journal of Solution Chemistry* **2000,** *29* (10), 937-954.

80. Bhatt, M. D.; Cho, M.; Cho, K., Interaction of Li+ ions with ethylene carbonate (EC): Density functional theory calculations. *Applied Surface Science* **2010,** *257* (5), 1463-1468.

81. Zhang, X.; Kuroda, D. G., An ab initio molecular dynamics study of the solvation structure and ultrafast dynamics of lithium salts in organic carbonates: A comparison between linear and cyclic carbonates. *The Journal of Chemical Physics* **2019,** *150* (18), 184501.

82. Franko, C. J.; Yim, C.-H.; Årén, F.; Åvall, G.; Whitfield, P. S.; Johansson, P.; Abu-Lebdeh, Y. A.; Goward, G. R., Concentration Dependent Solution Structure and Transport Mechanism in High Voltage LiTFSI–Adiponitrile Electrolytes. *Journal of The Electrochemical Society* **2020,** *167* (16), 160532.

83. Fulfer, K. D.; Kuroda, D. G., Ion speciation of lithium hexafluorophosphate in dimethyl carbonate solutions: an infrared spectroscopy study. *Physical Chemistry Chemical Physics* **2018,** *20* (35), 22710-22718.

84. Galle Kankanamge, S. R.; Kuroda, D. G., Molecular structure and ultrafast dynamics of sodium thiocyanate ion pairs formed in glymes of different lengths. *Physical Chemistry Chemical Physics* **2019,** *21* (2), 833-841.

85. Chen, X.; Kuroda, D. G., Molecular motions of acetonitrile molecules in the solvation shell of lithium ions. *The Journal of Chemical Physics* **2020,** *153* (16), 164502.

86. Fong, K. D.; Self, J.; Diederichsen, K. M.; Wood, B. M.; McCloskey, B. D.; Persson, K. A., Ion Transport and the True Transference Number in Nonaqueous Polyelectrolyte Solutions for Lithium Ion Batteries. *ACS Central Science* **2019,** *5* (7), 1250-1260.

87. Yamada, Y., Concentrated Battery Electrolytes: Developing New Functions by Manipulating the Coordination States. *Bulletin of the Chemical Society of Japan* **2020,** *93* (1), 109-118.

88. Nilsson, V.; Bernin, D.; Brandell, D.; Edström, K.; Johansson, P., Interactions and Transport in Highly Concentrated LiTFSI-based Electrolytes. *ChemPhysChem* **2020,** *21* (11), 1166-1176.

89. Ding, M. S.; von Cresce, A.; Xu, K., Conductivity, Viscosity, and Their Correlation of a Super-Concentrated Aqueous Electrolyte. *The Journal of Physical Chemistry C* **2017,** *121* (4), 2149-2153.

90. Yamada, Y.; Wang, J.; Ko, S.; Watanabe, E.; Yamada, A., Advances and issues in developing salt-concentrated battery electrolytes. *Nature Energy* **2019,** *4* (4), 269-280.

91. Wang, J.; Yamada, Y.; Sodeyama, K.; Watanabe, E.; Takada, K.; Tateyama, Y.; Yamada, A., Fire-extinguishing organic electrolytes for safe batteries. *Nature Energy* **2018,** *3* (1), 22-29.

92. Rushing, J. C.; Leonik, F. M.; Kuroda, D. G., Effect of Solvation Shell Structure and Composition on Ion Pair Formation: The Case Study of LiTDI in Organic Carbonates. *The Journal of Physical Chemistry C* **2019,** *123* (41), 25102-25112.

93. Borodin, O.; Han, S.-D.; Daubert, J. S.; Seo, D. M.; Yun, S.-H.; Henderson, W. A., Electrolyte Solvation and Ionic Association. *Journal of The Electrochemical Society* **2015,** *162* (4), A501-A510.

94. Arslanargin, A.; Powers, A.; Beck, T. L.; Rick, S. W., Models of Ion Solvation Thermodynamics in Ethylene Carbonate and Propylene Carbonate. *The Journal of Physical Chemistry B* **2016,** *120* (8), 1497-1508.

95. Chaudhari, M. I.; Nair, J. R.; Pratt, L. R.; Soto, F. A.; Balbuena, P. B.; Rempe, S. B., Scaling Atomic Partial Charges of Carbonate Solvents for Lithium Ion Solvation and Diffusion. *Journal of Chemical Theory and Computation* **2016,** *12* (12), 5709-5718.

96. Ganesh, P.; Jiang, D.-e.; Kent, P. R. C., Accurate Static and Dynamic Properties of Liquid Electrolytes for Li-Ion Batteries from ab initio Molecular Dynamics. *The Journal of Physical Chemistry B* **2011,** *115* (12), 3085-3090.

97. Borodin, O.; Smith, G. D., LiTFSI Structure and Transport in Ethylene Carbonate from Molecular Dynamics Simulations. *The Journal of Physical Chemistry B* **2006,** *110* (10), 4971-4977.

98. Andersson, R.; Årén, F.; Franco, A. A.; Johansson, P., Ion Transport Mechanisms via Time-Dependent Local Structure and Dynamics in Highly Concentrated Electrolytes. *Journal of The Electrochemical Society* **2020,** *167* (14), 140537.

99. Nilsson, V.; Kotronia, A.; Lacey, M.; Edström, K.; Johansson, P., Highly Concentrated LiTFSI–EC Electrolytes for Lithium Metal Batteries. *ACS Applied Energy Materials* **2020,** *3* (1), 200-207.

100. Arnaud, R.; Benrabah, D.; Sanchez, J. Y., Theoretical Study of CF3SO3Li, (CF3SO2)2NLi, and (CF3SO2)2CHLi Ion Pairs. *The Journal of Physical Chemistry* **1996,** *100* (26), 10882-10891.

101. Galle Kankanamge, S. R.; Kuroda, D. G., Molecular Structure, Chemical Exchange, and Conductivity Mechanism of High Concentration LiTFSI Electrolytes. *The Journal of Physical Chemistry B* **2020,** *124* (10), 1965-1977.

102. Dokko, K.; Watanabe, D.; Ugata, Y.; Thomas, M. L.; Tsuzuki, S.; Shinoda, W.; Hashimoto, K.; Ueno, K.; Umebayashi, Y.; Watanabe, M., Direct Evidence for Li Ion Hopping Conduction in Highly Concentrated Sulfolane-Based Liquid Electrolytes. *The Journal of Physical Chemistry B* **2018,** *122* (47), 10736-10745.

103. THE INFRACORD® DOUBLE BEAM SPECTROPHOTOMETER. *Chemical & Engineering News Archive* **1957,** *35* (33), 74.

104. Noda, I., Two-dimensional infrared spectroscopy. *Journal of the American Chemical Society* **1989,** *111* (21), 8116-8118.

105. Jonas, D. M., Two-Dimensional Femtosecond Spectroscopy. *Annual Review of Physical Chemistry* **2003,** *54* (1), 425-463.

106. Zheng, J.; Kwak, K.; Fayer, M. D., Ultrafast 2D IR Vibrational Echo Spectroscopy. *Accounts of Chemical Research* **2007,** *40* (1), 75-83.

107. Hamm, P.; Zanni, M., *Concepts and Methods of 2D Infrared Spectroscopy*. Cambridge University Press: Cambridge, 2011.

108. Cho, M., Coherent Two-Dimensional Optical Spectroscopy. *Chemical Reviews* **2008,** *108* (4), 1331-1418.

109. Bredenbeck, J.; Helbing, J.; Kolano, C.; Hamm, P., Ultrafast 2D–IR Spectroscopy of Transient Species. *ChemPhysChem* **2007,** *8* (12), 1747-1756.

110. Ge, N.-H.; M. Hochstrasser, R., Femtosecond two-dimensional infrared spectroscopy: IR-COSY and THIRSTY. *PhysChemComm* **2002,** *5* (3), 17-26.

111. Ganim, Z.; Chung, H. S.; Smith, A. W.; DeFlores, L. P.; Jones, K. C.; Tokmakoff, A., Amide I Two-Dimensional Infrared Spectroscopy of Proteins. *Accounts of Chemical Research* **2008,** *41* (3), 432-441.

112. Dijkstra, A. G.; Jansen, T. l. C.; Knoester, J., Localization and coherent dynamics of excitons in the two-dimensional optical spectrum of molecular J-aggregates. *The Journal of Chemical Physics* **2008,** *128* (16), 164511.

113. Hamm, P.; Helbing, J.; Bredenbeck, J., Two-Dimensional Infrared Spectroscopy of Photoswitchable Peptides. *Annual Review of Physical Chemistry* **2008,** *59* (1), 291-317.

114. Kim, Y. S.; Hochstrasser, R. M., Applications of 2D IR Spectroscopy to Peptides, Proteins, and Hydrogen-Bond Dynamics. *The Journal of Physical Chemistry B* **2009,** *113* (24), 8231-8251.

115. Woutersen, S.; Hamm, P., Nonlinear two-dimensional vibrational spectroscopy of peptides. *Journal of Physics: Condensed Matter* **2002,** *14* (39), R1035-R1062.

116. Andrews, D. L.; Ghoul, W. A., Eighth rank isotropic tensors and rotational averages. *Journal of Physics A: Mathematical and General* **1981,** *14* (6), 1281-1290.

117. Jackson, J. D., *Classical Electrodynamics*. Wiley: 1975.

118. Griffiths, D. J.; Griffiths, P. D. J.; College, R., *Introduction to Electrodynamics*. Prentice Hall: 1999.

119. Kubo, R., A Stochastic Theory of Line Shape. In *Advances in Chemical Physics*, 1969; pp 101-127.

120. Mukamel, S. In *Principles of Nonlinear Optical Spectroscopy*, 1995.

121. Breuer, H. P.; Breuer, P. I. H. P.; Petruccione, F.; Petruccione, S. P. A. P. F., *The Theory of Open Quantum Systems*. Oxford University Press: 2002.

122. Schwabl, F.; Brewer, W. D., *Statistical Mechanics*. Springer Berlin Heidelberg: 2002.

123. Roberts, S. T.; Loparo, J. J.; Tokmakoff, A., Characterization of spectral diffusion from two-dimensional line shapes. *The Journal of Chemical Physics* **2006,** *125* (8), 084502.

124. Kwak, K.; Park, S.; Finkelstein, I. J.; Fayer, M. D., Frequency-frequency correlation functions and apodization in two-dimensional infrared vibrational echo spectroscopy: A new approach. *The Journal of Chemical Physics* **2007,** *127* (12), 124503.

125. Chen, X.; Cui, Y.; Gobeze, H. B.; Kuroda, D. G., Assessing the Location of Ionic and Molecular Solutes in a Molecularly Heterogeneous and Nonionic Deep Eutectic Solvent. *The Journal of Physical Chemistry B* **2020,** *124* (23), 4762-4773.

126. Hamm, P.; Lim, M.; DeGrado, W. F.; Hochstrasser, R. M., The two-dimensional IR nonlinear spectroscopy of a cyclic penta-peptide in relation to its three-dimensional structure. *Proceedings of the National Academy of Sciences* **1999,** *96* (5), 2036-2041.

127. Guerin, A. C.; Riley, K.; Rupnik, K.; Kuroda, D. G., Determining the Energetics of the Hydrogen Bond through FTIR: A Hands-On Physical Chemistry Lab Experiment. *Journal of Chemical Education* **2016,** *93* (6), 1124-1129.

128. Candelaresi, M.; Pagliai, M.; Lima, M.; Righini, R., Chemical Equilibrium Probed by Two-Dimensional IR Spectroscopy: Hydrogen Bond Dynamics of Methyl Acetate in Water. *The Journal of Physical Chemistry A* **2009,** *113* (46), 12783-12790.

129. Backus, S.; III, C. G. D.; Murnane, M. M.; Kapteyn, H. C., High power ultrafast lasers. *Review of Scientific Instruments* **1998,** *69* (3), 1207-1223.

130. Wynne, K.; Reid, G. D.; Hochstrasser, R. M., Regenerative amplification of 30-fs pulses in Ti:sapphire at 5 kHz. *Opt. Lett.* **1994,** *19* (12), 895-897.

131. Khalil, M.; Demirdöven, N.; Tokmakoff, A., Obtaining Absorptive Line Shapes in Two-Dimensional Infrared Vibrational Correlation Spectra. *Physical Review Letters* **2003,** *90* (4), 047401.

132. Nitta, N.; Wu, F.; Lee, J. T.; Yushin, G., Li-ion battery materials: present and future. *Materials Today* **2015,** *18* (5), 252-264.

133. Spotnitz, R.; Franklin, J., Abuse behavior of high-power, lithium-ion cells. *Journal of Power Sources* **2003,** *113* (1), 81-100.

134. Mikolajczak, C., *Lithium-ion batteries hazard and use assessment.* New York : Springer, c2011.: 2011.

135. Voelker, P., *Trace degradation analysis of lithium-ion battery components*. Thermo Fisher Scientific: Sunnyvale, CA, 2014.

136. Finegan, D. P.; Scheel, M.; Robinson, J. B.; Tjaden, B.; Hunt, I.; Mason, T. J.; Millichamp, J.; Di Michiel, M.; Offer, G. J.; Hinds, G.; Brett, D. J. L.; Shearing, P. R., In-operando high-speed tomography of lithium-ion batteries during thermal runaway. *Nature Communications* **2015,** *6*, 6924-6924.

137. Hess, S.; Wohlfahrt-Mehrens, M.; Wachtler, M., Flammability of Li-Ion Battery Electrolytes: Flash Point and Self-Extinguishing Time Measurements. *Journal of the Electrochemical Society* **2015,** *162* (2), A3084-A3097.

138. Self, J.; Wood, B. M.; Rajput, N. N.; Persson, K. A., The Interplay between Salt Association and the Dielectric Properties of Low Permittivity Electrolytes: The Case of LiPF6 and LiAsF6 in Dimethyl Carbonate. *Journal of Physical Chemistry C* **2018,** *122* (4), 1990-1994.

139. Ding, M. S.; Jow, T. R., Conductivity and Viscosity of PC-DEC and PC-EC Solutions of LiPF6. *Journal of The Electrochemical Society* **2003,** *150* (5), A620-A628.

140. Logan, E. R.; Tonita, E. M.; Gering, K. L.; Li, J.; Ma, X.; Beaulieu, L. Y.; Dahn, J. R., A Study of the Physical Properties of Li-Ion Battery Electrolytes Containing Esters. *Journal of The Electrochemical Society* **2018,** *165* (2), A21-A30.

141. Lüttringhaus, A.; Dirksen, H. W., Tetramethylurea as a Solvent and Reagent. *Angewandte Chemie International Edition* **1964,** *3* (4), 260.

142. Lo, C.-C.; Chao, P.-M., Replacement of carcinogenic solvent HMPA by DMI in insect sex pheromone synthesis. *Journal of Chemical Ecology* **1990,** *16* (12), 3245-3253.

143. Wang, Q.; Ping, P.; Zhao, X.; Chu, G.; Sun, J.; Chen, C., Thermal runaway caused fire and explosion of lithium ion battery. *Journal of Power Sources* **2012,** *208*, 210-224.

144. America, M. C., Safety Data Sheet of DMI 1,3 Dimethyl-2-Imidazolidinone. **2012**.

145. Sun, H.; Mumby, S. J.; Maple, J. R.; Hagler, A. T., Ab-Initio Calculations on Small-Molecule Analogs of Polycarbonates. *J Phys Chem-Us* **1995,** *99* (16), 5873-5882.

146. Kemnitz, C. R.; Loewen, M. J., "Amide Resonance" Correlates with a Breadth of C−N Rotation Barriers. *Journal of the American Chemical Society* **2007,** *129* (9), 2521-2528.

147. Mujika, J. I.; Matxain, J. M.; Eriksson, L. A.; Lopez, X., Resonance Structures of the Amide Bond: The Advantages of Planarity. *Chemistry- A European Journal* **2006,** *12* (27), 7215-7224.

148. Wheland, G. W., *Resonance in organic chemistry*. Wiley: New York,, 1955; p 846 p.

149. Xu, K., Electrolytes and Interphases in Li-Ion Batteries and Beyond. *Chemical Reviews* **2014,** *114* (23), 11503-11618.

150. Asplund, M. C.; Zanni, M. T.; Hochstrasser, R. M., Two-dimensional infrared spectroscopy of peptides by phase-controlled femtosecond vibrational photon echoes. *P Natl Acad Sci USA* **2000,** *97* (15), 8219-8224.

151. Middleton, C. T.; Buchanan, L. E.; Dunkelberger, E. B.; Zanni, M. T., Utilizing Lifetimes to Suppress Random Coil Features in 2D IR Spectra of Peptides. *J Phys Chem Lett* **2011,** *2* (18), 2357-2361.

152. Kuroda, D. G.; Hochstrasser, R. M., Dynamic structures of aqueous oxalate and the effects of counterions seen by 2D IR. *Physical Chemistry Chemical Physics* **2012,** *14* (18), 6219-6224.

153. Zanni, M. T.; Hochstrasser, R. M., Two-dimensional infrared spectroscopy: a promising new method for the time resolution of structures. *Current Opinion in Structural Biology* **2001,** *11* (5), 516-522.

154. Maekawa, H.; Ge, N.-H., Picosecond Rotational Interconversion Adjacent to a C═O Bond Studied by Two-Dimensional Infrared Spectroscopy. *Journal of Physical Chemistry B* **2012,** *116* (36), 11292-11301.

155. Cui, Y. W.; Kuroda, D. G., Evidence of Molecular Heterogeneities in Amide-Based Deep Eutectic Solvents. *J Phys Chem A* **2018,** *122* (5), 1185-1193.

156. Kankanamge, S. R. G.; Kuroda, D. G., Molecular structure and ultrafast dynamics of sodium thiocyanate ion pairs formed in glymes of different lengths. *Physical Chemistry Chemical Physics* **2019,** *21* (2), 833-841.

157. Asbury, J. B.; Steinel, T.; Fayer, M. D., Vibrational echo correlation spectroscopy probes of hydrogen bond dynamics in water and methanol. *Journal of Luminescence* **2004,** *107* (1), 271-286.

158. Frisch, M. J.; Trucks, G. W.; Schlegel, H. B.; Scuseria, G. E.; Robb, M. A.; Cheeseman, J. R.; Scalmani, G.; Barone, V.; Petersson, G. A.; Nakatsuji, H.; Li, X.; Caricato, M.; Marenich, A. V.; Bloino, J.; Janesko, B. G.; Gomperts, R.; Mennucci, B.; Hratchian, H. P.; Ortiz, J. V.; Izmaylov, A. F.; Sonnenberg, J. L.; Williams; Ding, F.; Lipparini, F.; Egidi, F.; Goings, J.; Peng, B.; Petrone, A.; Henderson, T.; Ranasinghe, D.; Zakrzewski, V. G.; Gao, J.; Rega, N.; Zheng, G.; Liang, W.; Hada, M.; Ehara, M.; Toyota, K.; Fukuda, R.; Hasegawa, J.; Ishida, M.; Nakajima, T.; Honda, Y.; Kitao, O.; Nakai, H.; Vreven, T.; Throssell, K.; Montgomery Jr., J. A.; Peralta, J. E.; Ogliaro, F.; Bearpark, M. J.; Heyd, J. J.; Brothers, E. N.; Kudin, K. N.; Staroverov, V. N.; Keith, T. A.; Kobayashi, R.; Normand, J.; Raghavachari, K.; Rendell, A. P.; Burant, J. C.; Iyengar, S. S.; Tomasi, J.; Cossi, M.; Millam, J. M.; Klene, M.; Adamo, C.; Cammi, R.; Ochterski, J. W.; Martin, R. L.; Morokuma, K.; Farkas, O.; Foresman, J. B.; Fox, D. J. *Gaussian 16 Rev. C.01*, Wallingford, CT, 2016.

159. Cresce, A. V.; Russell, S. M.; Borodin, O.; Allen, J. A.; Schroeder, M. A.; Dai, M.; Peng, J.; Gobet, M. P.; Greenbaum, S. G.; Rogers, R. E.; Xu, K., Solvation behavior of carbonate-based electrolytes in sodium ion batteries. *Physical Chemistry Chemical Physics* **2016,** *19* (1), 574-586.

160. Woodard, K. T.; Fulfer, K. D. A.; Kuroda, D. G., Exploring the Energetics of the Lithium Ion-Organic Carbonate Interaction: A FTIR and DFT Study. *ECS Transactions* **2017,** *77* (11), 1911-1917.

161. Yang, H.; Zhuang, G. V.; Ross, P. N., Thermal stability of LiPF6 salt and Li-ion battery electrolytes containing LiPF6. *Journal of Power Sources* **2006,** *161* (1), 573-579.

162. Chapman, N.; Borodin, O.; Yoon, T.; Nguyen, C. C.; Lucht, B. L., Spectroscopic and Density Functional Theory Characterization of Common Lithium Salt Solvates in Carbonate Electrolytes for Lithium Batteries. *Journal of Physical Chemistry C* **2017,** *121* (4), 2135-2148.

163. Nie, M.; Abraham, D. P.; Seo, D. M.; Chen, Y.; Bose, A.; Lucht, B. L., Role of Solution Structure in Solid Electrolyte Interphase Formation on Graphite with LiPF6 in Propylene Carbonate. *Journal of Physical Chemistry C* **2013,** *117* (48), 25381-25389.

164. Fulfer, K. D. A.; Kuroda, D. G., Molecular Motions, Structure, and Composition of Carbonates in the Solvation Shell of the Lithium Ion, Via Infrared Spectroscopies. *ECS Transactions* **2017,** *77* (1), 3-10.

165. Kim, Y. S.; Hochstrasser, R. M., Chemical exchange 2D IR of hydrogen-bond making and breaking. *P Natl Acad Sci USA* **2005,** *102* (32), 11185-11190.

166. Liang, C.; Kwak, K.; Cho, M., Revealing the Solvation Structure and Dynamics of Carbonate Electrolytes in Lithium-Ion Batteries by Two-Dimensional Infrared Spectrum Modeling. *J Phys Chem Lett* **2017,** *8* (23), 5779-5784.

167. Hochstrasser, R. M., Two-dimensional IR-spectroscopy: polarization anisotropy effects. *Chem Phys* **2001,** *266* (2-3), 273-284.

168. Zanni, M. T.; Ge, N. H.; Kim, Y. S.; Hochstrasser, R. M., Two-dimensional IR spectroscopy can be designed to eliminate the diagonal peaks and expose only the crosspeaks needed for structure determination. *P Natl Acad Sci USA* **2001,** *98* (20), 11265-11270.

169. Jiang, H.; Zhang, Q.; Zhang, Y.; Sui, L.; Wu, G.; Yuan, K.; Yang, X., Li-Ion solvation in propylene carbonate electrolytes determined by molecular rotational measurements. *Physical Chemistry Chemical Physics* **2019,** *21* (20), 10417-10422.

170. Giorgini, M. G.; Futamatagawa, K.; Torii, H.; Musso, M.; Cerini, S., Solvation Structure around the Li+ Ion in Mixed Cyclic/Linear Carbonate Solutions Unveiled by the Raman Noncoincidence Effect. *J Phys Chem Lett* **2015,** *6* (16), 3296-3302.

171. Ong, M. T.; Verners, O.; Draeger, E. W.; van Duin, A. C. T.; Lordi, V.; Pask, J. E., Lithium Ion Solvation and Diffusion in Bulk Organic Electrolytes from First-Principles and Classical Reactive Molecular Dynamics. *Journal of Physical Chemistry B* **2015,** *119* (4), 1535-1545.

172. Pollard, T. P.; Beck, T. L., Structure and polarization near the Li+ ion in ethylene and propylene carbonates. *Journal of Chemical Physics* **2017,** *147* (16), 161710.

173. Flores, E.; Åvall, G.; Jeschke, S.; Johansson, P., Solvation structure in dilute to highly concentrated electrolytes for lithium-ion and sodium-ion batteries. *Electrochimica Acta* **2017,** *233*, 134-141.

174. Borodin, O.; Olguin, M.; Ganesh, P.; Kent, P. R. C.; Allen, J. L.; Henderson, W. A., Competitive lithium solvation of linear and cyclic carbonates from quantum chemistry. *Physical Chemistry Chemical Physics* **2016,** *18* (1), 164-175.

175. Smiechowski, M.; Krakowiak, J.; Bruzdziak, P.; Stangret, J., Unique agreement of experimental and computational infrared spectroscopy: a case study of lithium bromide solvation in an important electrochemical solvent. *Physical Chemistry Chemical Physics* **2017,** *19* (13), 9270-9280.

176. Schneider, S. H.; Kratochvil, H. T.; Zanni, M. T.; Boxer, S. G., Solvent-Independent Anharmonicity for Carbonyl Oscillators. *Journal of Physical Chemistry B* **2017,** *121* (10), 2331-2338.

177. Cui, Y.; Rushing, J. C.; Seifert, S.; Bedford, N. M.; Kuroda, D. G., Molecularly Heterogeneous Structure of a Nonionic Deep Eutectic Solvent Composed of N-Methylacetamide and Lauric Acid. *Journal of Physical Chemistry B* **2019,** *123* (18), 3984-3993.

178. Ghosh, A.; Tucker, M. J.; Hochstrasser, R. M., Identification of Arginine Residues in Peptides by 2D-IR Echo Spectroscopy. *J Phys Chem A* **2011,** *115* (34), 9731-9738.

179. Vorobyev, D. Y.; Kuo, C.-H.; Kuroda, D. G.; Scott, J. N.; Vanderkooi, J. M.; Hochstrasser, R. M., Water-Induced Relaxation of a Degenerate Vibration of Guanidinium Using 2D IR Echo Spectroscopy. *Journal of Physical Chemistry B* **2010,** *114* (8), 2944-2953.

180. Rubtsova, N. I.; Rubtsov, I. V., Vibrational Energy Transport in Molecules Studied by Relaxation-Assisted Two-Dimensional Infrared Spectroscopy. *Annu Rev Phys Chem* **2015,** *66*, 717-738.

181. Kuroda, D. G.; Hochstrasser, R. M., Two-dimensional infrared spectral signature and hydration of the oxalate dianion. *Journal of Chemical Physics* **2011,** *135* (20), 204502.

182. Kuroda, D. G.; Abdo, M.; Chuntonov, L.; III, A. B. S.; Hochstrasser, R. M., Vibrational dynamics of a non-degenerate ultrafast rotor: The (C12,C13)-oxalate ion. *Journal of Chemical Physics* **2013,** *139* (16), 164514.

183. Kobus, M.; Nguyen, P. H.; Stock, G., Coherent vibrational energy transfer along a peptide helix. *Journal of Chemical Physics* **2011,** *134* (12), 124518.

184. E. Peled, z. a. S. M., Review—SEI: Past, Present and Future. *Journal of The Electrochemical Society* **2017,** *164* (7), A1703-A1719.

185. Marcinek, M.; Syzdek, J.; Marczewski, M.; Piszcz, M.; Niedzicki, L.; Kalita, M.; Plewa-Marczewska, A.; Bitner, A.; Wieczorek, P.; Trzeciak, T.; Kasprzyk, M.; P.Łężak;

Zukowska, Z.; Zalewska, A.; Wieczorek, W., Electrolytes for Li-ion transport – Review. *Solid State Ionics* **2015,** *276*, 107-126.

186. Chockla, A. M.; Harris, J. T.; Akhavan, V. A.; Bogart, T. D.; Holmberg, V. C.; Steinhagen, C.; Mullins, C. B.; Stevenson, K. J.; Korgel, B. A., Silicon Nanowire Fabric as a Lithium Ion Battery Electrode Material. *Journal of the American Chemical Society* **2011,** *133* (51), 20914-20921.

187. Taberna, P. L.; Mitra, S.; Poizot, P.; Simon, P.; Tarascon, J. M., High rate capabilities Fe3O4-based Cu nano-architectured electrodes for lithium-ion battery applications. *Nature Materials* **2006,** *5* (7), 567-573.

188. Hu, Y.-Y.; Liu, Z.; Nam, K.-W.; Borkiewicz, O. J.; Cheng, J.; Hua, X.; Dunstan, M. T.; Yu, X.; Wiaderek, K. M.; Du, L.-S.; Chapman, K. W.; Chupas, P. J.; Yang, X.-Q.; Grey, C. P., Origin of additional capacities in metal oxide lithium-ion battery electrodes. *Nature Materials* **2013,** *12* (12), 1130-1136.

189. Haregewoin, A. M.; Wotango, A. S.; Hwang, B.-J., Electrolyte additives for lithium ion battery electrodes: progress and perspectives. *Energy & Environmental Science* **2016,** *9* (6), 1955-1988.

190. Michan, A. L.; Parimalam, B. S.; Leskes, M.; Kerber, R. N.; Yoon, T.; Grey, C. P.; Lucht, B. L., Fluoroethylene Carbonate and Vinylene Carbonate Reduction: Understanding Lithium-Ion Battery Electrolyte Additives and Solid Electrolyte Interphase Formation. *Chemistry of Materials* **2016,** *28* (22), 8149-8159.

191. Seo, D. M.; Reininger, S.; Kutcher, M.; Redmond, K.; Euler, W. B.; Lucht, B. L., Role of Mixed Solvation and Ion Pairing in the Solution Structure of Lithium Ion Battery Electrolytes. *Journal of Physical Chemistry C* **2015,** *119* (25), 14038-14046.

192. Wang, J.; Yamada, Y.; Sodeyama, K.; Chiang, C. H.; Tateyama, Y.; Yamada, A., Superconcentrated electrolytes for a high-voltage lithium-ion battery. *Nature Communications* **2016,** *7* (1), 12032.

193. Umebayashi, Y.; Mitsugi, T.; Fukuda, S.; Fujimori, T.; Fujii, K.; Kanzaki, R.; Takeuchi, M.; Ishiguro, S.-I., Lithium Ion Solvation in Room-Temperature Ionic Liquids Involving Bis(trifluoromethanesulfonyl) Imide Anion Studied by Raman Spectroscopy and DFT Calculations. *Journal of Physical Chemistry B* **2007,** *111* (45), 13028-13032.

194. Suo, L.; Borodin, O.; Gao, T.; Olguin, M.; Ho, J.; Fan, X.; Luo, C.; Wang, C.; Xu, K., "Water-in-salt" electrolyte enables high-voltage aqueous lithium-ion chemistries. *Science* **2015,** *350* (6263), 938-943.

195. Soetens, J.-C.; Millot, C.; Maigret, B.; Bakó, I., Molecular dynamics simulation and X—ray diffraction studies of ethylene carbonate, propylene carbonate and dimethyl carbonate in liquid phase. *Journal of Molecular Liquids* **2001,** *92* (3), 201-216.

196. Fujii, K.; Matsugami, M.; Ueno, K.; Ohara, K.; Sogawa, M.; Utsunomiya, T.; Morita, M., Long-Range Ion-Ordering in Salt-Concentrated Lithium-Ion Battery Electrolytes: A Combined High-Energy X-ray Total Scattering and Molecular Dynamics Simulation Study. *Journal of Physical Chemistry C* **2017,** *121* (41), 22720-22726.

197. Yang, L.; Xiao, A.; Lucht, B. L., Investigation of solvation in lithium ion battery electrolytes by NMR spectroscopy. *Journal of Molecular Liquids* **2010,** *154* (2), 131-133.

198. Bogle, X.; Vazquez, R.; Greenbaum, S.; Cresce, A. v. W.; Xu, K., Understanding Li+–Solvent Interaction in Nonaqueous Carbonate Electrolytes with 17O NMR. *J Phys Chem Lett* **2013,** *4* (10), 1664-1668.

199. Hayamizu, K., Temperature Dependence of Self-Diffusion Coefficients of Ions and Solvents in Ethylene Carbonate, Propylene Carbonate, and Diethyl Carbonate Single Solutions and Ethylene Carbonate + Diethyl Carbonate Binary Solutions of LiPF6 Studied by NMR. *Journal of Chemical & Engineering Data* **2012,** *57* (7), 2012-2017.

200. Matsuda, Y.; Fukushima, T.; Hashimoto, H.; Arakawa , R., Solvation of Lithium Ions in Mixed Organic Electrolyte Solutions by Electrospray Ionization Mass Spectroscopy. *Journal of The Electrochemical Society* **2002,** *149* (8), A1045-A1048.

201. Cresce, A.; Xu, K., Preferential Solvation of Li+ Directs Formation of Interphase on Graphitic Anode. *Electrochemical and Solid State Letters* **2011,** *14*, A154.

202. Fukushima, T.; Matsuda, Y.; Hashimoto, H.; Arakawa , R., Studies on Solvation of Lithium Ions in Organic Electrolyte Solutions by Electrospray Ionization-Mass Spectroscopy. *Electrochemical and Solid State Letters* **2001,** *4* (8), A127-A128.

203. Lewis, N. H. C.; Zhang, Y.; Dereka, B.; Carino, E. V.; Maginn, E. J.; Tokmakoff, A., Signatures of Ion Pairing and Aggregation in the Vibrational Spectroscopy of Super-Concentrated Aqueous Lithium Bistriflimide Solutions. *Journal of Physical Chemistry C* **2020**.

204. Bao, L.; Zou, X.; Luo, X.; Pu, Y.; Wang, J.; Lei, J., Real-time tracking the Li+-ion transition behavior and dynamics in solid Poly(vinyl alcohol)/LiClO4 electrolytes. *Scientific Reports* **2017,** *7* (1), 45921.

205. Borodin, O.; Zhuang, G. V.; Ross, P. N.; Xu, K., Molecular Dynamics Simulations and Experimental Study of Lithium Ion Transport in Dilithium Ethylene Dicarbonate. *Journal of Physical Chemistry C* **2013,** *117* (15), 7433-7444.

206. Kumar, N.; Seminario, J. M., Lithium-Ion Model Behavior in an Ethylene Carbonate Electrolyte Using Molecular Dynamics. *Journal of Physical Chemistry C* **2016,** *120* (30), 16322-16332.

207. Chang, T.-M.; Dang, L. X., Li+ solvation and kinetics of Li+–BF4−/PF6− ion pairs in ethylene carbonate. A molecular dynamics study with classical rate theories. *Journal of Chemical Physics* **2017,** *147* (16), 161709.

208. Fawcett, W. R.; Liu, G.; Faguy, P. W.; Foss, C. A.; Motheo, A. J., Attenuated total reflection fourier-transform infrared spectroscopic study of ion–solvent and ion–ion interactions in alkali-metal perchlorate–acetonitrile solutions. *Journal of the Chemical Society, Faraday Transactions* **1993,** *89* (5), 811-816.

209. Mollner, A. K.; Brooksby, P. A.; Loring, J. S.; Bako, I.; Palinkas, G.; Fawcett, W. R., Ion−Solvent Interactions in Acetonitrile Solutions of Lithium Iodide and Tetrabutylammonium Iodide. *J Phys Chem A* **2004,** *108* (16), 3344-3349.

210. Xuan, X.; Zhang, H.; Wang, J.; Wang, H., Vibrational Spectroscopic and Density Functional Studies on Ion Solvation and Association of Lithium Tetrafluorobrate in Acetonitrile. *J Phys Chem A* **2004,** *108* (37), 7513-7521.

211. Fawcett, W. R.; Liu, G.; Kessler, T. E., Solvent-induced frequency shifts in the infrared spectrum of acetonitrile in organic solvents. *J Phys Chem-Us* **1993,** *97* (37), 9293-9298.

212. Seo, D. M.; Borodin, O.; Han, S.-D.; Ly, Q.; Boyle, P. D.; Henderson, W. A., Electrolyte Solvation and Ionic Association. *Journal of The Electrochemical Society* **2012,** *159* (5), A553-A565.

213. Ji, M.; Park, S.; Gaffney, K. J., Dynamics of Ion Assembly in Solution: 2DIR Spectroscopy Study of LiNCS in Benzonitrile. *J Phys Chem Lett* **2010,** *1* (12), 1771-1775.

214. Paoli, D.; Luçon, M.; Chabanel, M., Vibrational study of ionic association in aprotic solvents—I. The ion pairs of alkali and silver thiocyanate in dimethylformamide or dimethylthioformamide. *Spectrochimica Acta, Part A: Molecular and Biomolecular Spectroscopy* **1978,** *34* (11), 1087-1091.

215. Lee, K.-K.; Park, K.-H.; Kwon, D.; Choi, J.-H.; Son, H.; Park, S.; Cho, M., Ion-pairing dynamics of Li+ and SCN− in dimethylformamide solution: Chemical exchange two-dimensional infrared spectroscopy. *Journal of Chemical Physics* **2011,** *134* (6), 064506.

216. Eckbreth, A. C., BOXCARS: Crossed‐beam phase‐matched CARS generation in gases. *Applied Physics Letters* **1978,** *32* (7), 421-423.

217. Sokolowsky, K. P.; Fayer, M. D., Dynamics in the Isotropic Phase of Nematogens Using 2D IR Vibrational Echo Measurements on Natural-Abundance 13CN and Extended Lifetime Probes. *Journal of Physical Chemistry B* **2013,** *117* (48), 15060-15071.

218. Park, S.; Ji, M.; Gaffney, K. J., Ligand Exchange Dynamics in Aqueous Solution Studied with 2DIR Spectroscopy. *Journal of Physical Chemistry B* **2010,** *114* (19), 6693-6702.

219. Kim, Y. S.; Wang, J.; Hochstrasser, R. M., Two-Dimensional Infrared Spectroscopy of the Alanine Dipeptide in Aqueous Solution. *Journal of Physical Chemistry B* **2005,** *109* (15), 7511-7521.

220. VandeVondele, J.; Krack, M.; Mohamed, F.; Parrinello, M.; Chassaing, T.; Hutter, J., Quickstep: Fast and accurate density functional calculations using a mixed Gaussian and plane waves approach. *Computer Physics Communications* **2005,** *167* (2), 103-128.

221. Grimme, S., Semiempirical GGA-type density functional constructed with a long-range dispersion correction. *Journal of Computational Chemistry* **2006,** *27* (15), 1787-1799.

222. Goedecker, S.; Teter, M.; Hutter, J., Separable dual-space Gaussian pseudopotentials. *Physical Review B* **1996,** *54* (3), 1703-1710.

223. Lippert, G.; Hutter, J.; Ballone, P.; Parrinello, M., Response Function Basis Sets: Application to Density Functional Calculations. *J Phys Chem-Us* **1996,** *100* (15), 6231-6235.

224. Perdew, J. P.; Burke, K.; Ernzerhof, M., Generalized Gradient Approximation Made Simple. *Physical Review Letters* **1996,** *77* (18), 3865-3868.

225. Ray, P.; Vogl, T.; Balducci, A.; Kirchner, B., Structural Investigations on Lithium-Doped Protic and Aprotic Ionic Liquids. *Journal of Physical Chemistry B* **2017,** *121* (20), 5279-5292.

226. Leung, K.; Budzien, J. L., Ab initio molecular dynamics simulations of the initial stages of solid–electrolyte interphase formation on lithium ion battery graphitic anodes. *Physical Chemistry Chemical Physics* **2010,** *12* (25), 6583-6586.

227. Hwang, S.; Kim, D.-H.; Shin, J. H.; Jang, J. E.; Ahn, K. H.; Lee, C.; Lee, H., Ionic Conduction and Solution Structure in LiPF6 and LiBF4 Propylene Carbonate Electrolytes. *Journal of Physical Chemistry C* **2018,** *122* (34), 19438-19446.

228. Gaussian 09, R. D., M. J. Frisch, G. W. Trucks, H. B. Schlegel, G. E. Scuseria, ; M. A. Robb, J. R. C., G. Scalmani, V. Barone, B. Mennucci, ; G. A. Petersson, H. N., M. Caricato, X. Li, H. P. Hratchian, ; A. F. Izmaylov, J. B., G. Zheng, J. L. Sonnenberg, M. Hada, ; M. Ehara, K. T., R. Fukuda, J. Hasegawa, M. Ishida, T. Nakajima, ; Y. Honda, O. K., H. Nakai, T. Vreven, J. A. Montgomery, Jr., ; J. E. Peralta, F. O., M. Bearpark, J. J. Heyd, E. Brothers, ; K. N. Kudin, V. N. S., T. Keith, R. Kobayashi, J. Normand, ; K. Raghavachari, A. R., J. C. Burant, S. S. Iyengar, J. Tomasi, ; M. Cossi, N. R., J. M. Millam, M. Klene, J. E. Knox, J. B. Cross, ; V. Bakken, C. A., J. Jaramillo, R. Gomperts, R. E. Stratmann, ; O. Yazyev, A. J. A., R. Cammi, C. Pomelli, J. W. Ochterski, ; R. L. Martin, K. M., V. G. Zakrzewski, G. A. Voth, ; P. Salvador, J. J. D., S. Dapprich, A. D. Daniels, ; O. Farkas, J. B. F., J. V. Ortiz, J. Cioslowski, ; and D. J. Fox, G., Inc., Wallingford CT, 2013.

229. Martínez, L.; Andrade, R.; Birgin, E. G.; Martínez, J. M., PACKMOL: A package for building initial configurations for molecular dynamics simulations. *Journal of Computational Chemistry* **2009,** *30* (13), 2157-2164.

230. Maier, J. A.; Martinez, C.; Kasavajhala, K.; Wickstrom, L.; Hauser, K. E.; Simmerling, C., ff14SB: Improving the Accuracy of Protein Side Chain and Backbone Parameters from ff99SB. *Journal of Chemical Theory and Computation* **2015,** *11* (8), 3696-3713.

231. D.A. Case, R. M. B., D.S. Cerutti, T.E. Cheatham, III, T.A. Darden, R.E. Duke, T.J. Giese, H. Gohlke,; A.W. Goetz, N. H., S. Izadi, P. Janowski, J. Kaus, A. Kovalenko, T.S. Lee, S. LeGrand, P. Li, C.; Lin, T. L., R. Luo, B. Madej, D. Mermelstein, K.M. Merz, G. Monard, H. Nguyen, H.T. Nguyen, I.; Omelyan, A. O., D.R. Roe, A. Roitberg, C. Sagui, C.L. Simmerling, W.M. Botello-Smith, J. Swails,; R.C. Walker, J. W., R.M. Wolf, X. Wu, L. Xiao and P.A. Kollman (2016), AMBER 2016. University of California, San Francisco.

232. Suzuki, I.; Nakagawa, J.; Fujiyama, T., Vibration—rotation spectrum of methyl cyanide— analyses of ν2 and ν3 + ν4 bands. *Spectrochimica Acta Part A: Molecular Spectroscopy* **1977,** *33* (6), 689-698.

233. Hashimoto, S.; Ohba, T.; Ikawa, S.-i., Infrared and molecular dynamics study of reorientational relaxation of liquid acetonitrile. *Chem Phys* **1989,** *138* (1), 63-69.

234. Jamroz, D.; Stangret, J.; Lindgren, J., An infrared spectroscopic study of the preferential solvation in water-acetonitrile mixtures. *Journal of the American Chemical Society* **1993,** *115* (14), 6165-6168.

235. Sajeevkumar, V. A.; Singh, S., Infrared spectral studies on preferential solvation of lithium ions in binary mixtures of acetonitrile and dimethyl formamide. *Journal of Molecular Structure* **1996,** *382* (2), 101-110.

236. Seo, J.-S.; Cheong, B.-S.; Cho, H.-G., Solvation of LiClO4 and NaClO4 in deuterated acetonitrile studied by means of infrared and Raman spectroscopy. *Spectrochimica Acta, Part A: Molecular and Biomolecular Spectroscopy* **2002,** *58* (8), 1747-1756.

237. Liu, L.; Bakker, H. J., Infrared-Activated Proton Transfer in Aqueous Nafion Proton-Exchange-Membrane Nanochannels. *Physical Review Letters* **2014,** *112* (25), 258301.

238. See, K. A.; Wu, H.-L.; Lau, K. C.; Shin, M.; Cheng, L.; Balasubramanian, M.; Gallagher, K. G.; Curtiss, L. A.; Gewirth, A. A., Effect of Hydrofluoroether Cosolvent Addition on Li Solvation in Acetonitrile-Based Solvate Electrolytes and Its Influence on S Reduction in a Li–S Battery. *ACS Applied Materials & Interfaces* **2016,** *8* (50), 34360-34371.

239. Seo, D. M.; Borodin, O.; Balogh, D.; O'Connell, M.; Ly, Q.; Han, S.-D.; Passerini, S.; Henderson, W. A., Electrolyte Solvation and Ionic Association III. Acetonitrile-Lithium Salt Mixtures–Transport Properties. *Journal of The Electrochemical Society* **2013,** *160* (8), A1061-A1070.

240. Puchta, R.; Galle, M.; van Eikema Hommes, N.; Pasgreta, E.; van Eldik, R., Evidence for Associative Ligand Exchange Processes on Solvated Lithium Cations. *Inorganic Chemistry* **2004,** *43* (26), 8227-8229.

241. Spångberg, D.; Hermansson, K., The solvation of Li+ and Na+ in acetonitrile from ab initio-derived many-body ion–solvent potentials. *Chem Phys* **2004,** *300* (1), 165-176.

242. Šanda, F.; Perlík, V.; Lincoln, C. N.; Hauer, J., Center Line Slope Analysis in Two-Dimensional Electronic Spectroscopy. *J Phys Chem A* **2015,** *119* (44), 10893-10909.

243. Fenn, E. E.; Fayer, M. D., Extracting 2D IR frequency-frequency correlation functions from two component systems. *Journal of Chemical Physics* **2011,** *135* (7), 074502.

244. Kuroda, D. G.; Vorobyev, D. Y.; Hochstrasser, R. M., Ultrafast relaxation and 2D IR of the aqueous trifluorocarboxylate ion. *Journal of Chemical Physics* **2010,** *132* (4), 044501.

245. Kramer, P. L.; Nishida, J.; Giammanco, C. H.; Tamimi, A.; Fayer, M. D., Observation and theory of reorientation-induced spectral diffusion in polarization-selective 2D IR spectroscopy. *Journal of Chemical Physics* **2015,** *142* (18), 184505.

246. Finkelstein, I. J.; Zheng, J.; Ishikawa, H.; Kim, S.; Kwak, K.; Fayer, M. D., Probing dynamics of complex molecular systems with ultrafast 2D IR vibrational echo spectroscopy. *Physical Chemistry Chemical Physics* **2007,** *9* (13), 1533-1549.

247. Yoshino, A., The Birth of the Lithium-Ion Battery. *Angewandte Chemie International Edition* **2012,** *51* (24), 5798-5800.

248. Bila, M.; Opathella, C.; Venkatesh, B., Grid connected performance of a household lithium-ion battery energy storage system. *Journal of Energy Storage* **2016,** *6*, 178-185.

249. Horiba, T., Lithium-Ion Battery Systems. *Proceedings of the IEEE* **2014,** *102* (6), 939-950.

250. Sahin, H.; Guvenc, L., Household robotics: autonomous devices for vacuuming and lawn mowing [Applications of control]. *IEEE Control Systems Magazine* **2007,** *27* (2), 20-96.

251. Diouf, B.; Pode, R., Potential of lithium-ion batteries in renewable energy. *Renewable Energy* **2015,** *76*, 375-380.

252. Li, J.; Du, Z.; Ruther, R. E.; An, S. J.; David, L. A.; Hays, K.; Wood, M.; Phillip, N. D.; Sheng, Y.; Mao, C.; Kalnaus, S.; Daniel, C.; Wood, D. L., Toward Low-Cost, High-Energy Density, and High-Power Density Lithium-Ion Batteries. *JOM* **2017,** *69* (9), 1484-1496.

253. Wang, S.; Quan, W.; Zhu, Z.; Yang, Y.; Liu, Q.; Ren, Y.; Zhang, X.; Xu, R.; Hong, Y.; Zhang, Z.; Amine, K.; Tang, Z.; Lu, J.; Li, J., Lithium titanate hydrates with superfast and stable cycling in lithium ion batteries. *Nature Communications* **2017,** *8* (1), 627.

254. Bandhauer, T. M.; Garimella, S.; Fuller, T. F., A Critical Review of Thermal Issues in Lithium-Ion Batteries. *Journal of The Electrochemical Society* **2011,** *158* (3), R1.

255. Sun, J.; Li, J.; Zhou, T.; Yang, K.; Wei, S.; Tang, N.; Dang, N.; Li, H.; Qiu, X.; Chen, L., Toxicity, a serious concern of thermal runaway from commercial Li-ion battery. *Nano Energy* **2016,** *27*, 313-319.

256. Wood, D. L.; Li, J.; Daniel, C., Prospects for reducing the processing cost of lithium ion batteries. *Journal of Power Sources* **2015,** *275*, 234-242.

257. Wang, Q.; Jiang, L.; Yu, Y.; Sun, J., Progress of enhancing the safety of lithium ion battery from the electrolyte aspect. *Nano Energy* **2019,** *55*, 93-114.

258. Kong, F.; Liang, X.; Yi, L.; Fang, X.; Yin, Z.; Wang, Y.; Zhang, R.; Liu, L.; Chen, Q.; Li, M., Multi-electron reactions for the synthesis of a vanadium-based amorphous material as lithium-ion battery cathode with high specific capacity. *Energy* **2020**, 119513.

259. Ji, Y.; Lu, X.; Luo, F.; Zhang, W.; Tian, Q.; Sui, Z., Improved SnO_2/C composite anode enabled by well-designed heterogeneous nanospheres decoration. *Chemical Physics Letters* **2021,** *763*, 138242.

260. Hirata, K.; Kawase, T.; Sumida, Y., Effects of Lithium Salts and Solvents on the Performance of Lithium-ion Batteries with Carbonate-free Electrolytes Comprising Lithium Bis(fluorosulfonyl)imide and Sulfolane. *Chemistry Letters* **2020,** *49* (10), 1140-1143.

261. Yuanjie, Z.; Yida, W.; Xiaowei, M.; Haicong, L.; Xuejie, H., 4.5 V Li-ion battery with a carbonate ester-based electrolyte. *Energy Storage Science and Technology* **2020,** *9* (2), 319.

262. Kim, J.; Pham, H. Q.; Chung, G. J.; Hwang, E.-H.; Kwon, Y.-G.; Song, S.-W., Impacts of fluorinated phosphate additive on interface stabilization of 4.6 V battery cathode. *Electrochimica Acta* **2021,** *367*, 137527.

263. Pathak, A. D.; Samanta, K.; Sahu, K. K.; Pati, S., Mechanistic insight into the performance enhancement of Si anode of a lithium-ion battery with a fluoroethylene carbonate electrolyte additive. *Journal of Applied Electrochemistry* **2020**.

264. Aupperle, F.; Eshetu, G. G.; Eberman, K. W.; Xioa, A.; Bridel, J.-S.; Figgemeier, E., Realizing a high-performance LiNi 0.6 Mn 0.2 Co 0.2 O 2/silicon–graphite full lithium ion battery cell via a designer electrolyte additive. *Journal of Materials Chemistry A* **2020,** *8* (37), 19573-19587.

265. Zhang, M.; Hao, H.; Zhou, D.; Duan, Y.; Wang, Y.; Bian, H., Understanding the Microscopic Structure of a "Water-in-Salt" Lithium Ion Battery Electrolyte Probed with Ultrafast IR Spectroscopy. *The Journal of Physical Chemistry C* **2020,** *124* (16), 8594-8604.

266. Borodin, O.; Smith, G. D., Quantum Chemistry and Molecular Dynamics Simulation Study of Dimethyl Carbonate: Ethylene Carbonate Electrolytes Doped with LiPF6. *The Journal of Physical Chemistry B* **2009,** *113* (6), 1763-1776.

267. Yi, T.-F.; Shu, J.; Yue, C.-B.; Zhu, X.-D.; Zhou, A.-N.; Zhu, Y.-R.; Zhu, R.-S., Enhanced cycling stability of microsized LiCoO2 cathode by Li4Ti5O12 coating for lithium ion battery. *Materials Research Bulletin* **2010,** *45* (4), 456-459.

268. McKinnon, W. R.; Dahn, J. R., How to Reduce the Cointercalation of Propylene Carbonate in Li x ZrS2 and Other Layered Compounds. *Journal of The Electrochemical Society* **1985,** *132* (2), 364-366.

269. Jeong, S.-K.; Inaba, M.; Iriyama, Y.; Abe, T.; Ogumi, Z., Electrochemical Intercalation of Lithium Ion within Graphite from Propylene Carbonate Solutions. *Electrochemical and Solid-State Letters* **2003,** *6* (1), A13.

270. Mandai, T.; Yoshida, K.; Ueno, K.; Dokko, K.; Watanabe, M., Criteria for solvate ionic liquids. *Physical Chemistry Chemical Physics* **2014,** *16* (19), 8761-8772.

271. Suo, L.; Hu, Y.-S.; Li, H.; Armand, M.; Chen, L., A new class of Solvent-in-Salt electrolyte for high-energy rechargeable metallic lithium batteries. *Nature Communications* **2013,** *4* (1), 1481.

272. Xiang, L.; Ou, X.; Wang, X.; Zhou, Z.; Li, X.; Tang, Y., Highly Concentrated Electrolyte towards Enhanced Energy Density and Cycling Life of Dual-Ion Battery. *Angewandte Chemie International Edition* **2020,** *59* (41), 17924-17930.

273. Nilsson, V. O. In *Highly Concentrated Electrolytes for Lithium Batteries - From fundamentals to cell tests*, 2018.

274. Ugata, Y.; Thomas, M. L.; Mandai, T.; Ueno, K.; Dokko, K.; Watanabe, M., Li-ion hopping conduction in highly concentrated lithium bis(fluorosulfonyl)amide/dinitrile liquid electrolytes. *Physical Chemistry Chemical Physics* **2019,** *21* (19), 9759-9768.

275. Hänggi, P.; Talkner, P.; Borkovec, M., Reaction-rate theory: fifty years after Kramers. *Reviews of Modern Physics* **1990,** *62* (2), 251-341.

276. Ren, Z.; Ivanova, A. S.; Couchot-Vore, D.; Garrett-Roe, S., Ultrafast Structure and Dynamics in Ionic Liquids: 2D-IR Spectroscopy Probes the Molecular Origin of Viscosity. *The Journal of Physical Chemistry Letters* **2014,** *5* (9), 1541-1546.

277. Reuter, D.; Binder, C.; Lunkenheimer, P.; Loidl, A., Ionic conductivity of deep eutectic solvents: the role of orientational dynamics and glassy freezing. *Physical Chemistry Chemical Physics* **2019,** *21* (13), 6801-6809

VITA

Xiaobing Chen finished her undergraduate study and obtained the Bachelor of Engineering degree in the major of Applied Chemistry from Qingdao University of Science and Technology in 2016. She entered the United States to pursue higher education in the same year. She came to Louisiana State University to continue her study under the guidance of Prof. Daniel Kuroda in the division of physical chemistry. She is specialized in the linear and non-linear infrared spectroscopy. Her research during graduate school focuses on the investigation of materials at the molecular level through a combination of experimental and theoretical tools.